

**STRUCTURAL CHANGES PROBED IN POLYMER-SOLVENT  
SYSTEMS AT MOLECULAR, CRYSTALLINE AND LAMELLAR  
LENGTH-SCALES DURING CRYSTALLIZATION AND PHASE  
TRANSITIONS**

**Thesis Submitted to AcSIR for the Award of the Degree of DOCTOR OF  
PHILOSOPHY in Chemical Sciences**



by

**SHAIJU P**

**Registration No: 10CC12A39005**

**Under the Supervision of**

**Dr. E. BHOJE GOWD**



**CSIR-NATIONAL INSTITUTE FOR INTERDISCIPLINARY SCIENCE AND  
TECHNOLOGY (CSIR-NIIST)**

**THIRUVANANTHAPURAM-695 019, KERALA, INDIA**

**2017**



## **DECLARATION**

I hereby declare that the work incorporated in the thesis entitled: “**Structural Changes Probed in Polymer-Solvent Systems at Molecular, Crystalline and Lamellar Length-Scales during Crystallization and Phase Transitions**” is the result of the investigations carried out by me at the Materials Science and Technology Division, CSIR-National Institute for Interdisciplinary Science and Technology (CSIR-NIIST), Thiruvananthapuram, under the supervision of Dr. E. Bhoje Gowd and the same has not been submitted elsewhere for any other degree. Due acknowledgements have been made wherever anything has been borrowed from other sources.

**Shaiju P**



राष्ट्रीय अंतर्विषयी विज्ञान तथा प्रौद्योगिकी संस्थान  
NATIONAL INSTITUTE FOR INTERDISCIPLINARY SCIENCE & TECHNOLOGY

वैज्ञानिक तथा औद्योगिक अनुसंधान परिषद्

Council of Scientific & Industrial Research

इंडस्ट्रियल इस्टेट पि. ओ, पाप्पनकोड, तिरुवनंतपुरम- 695 019

Industrial Estate P.O., Thiruvananthapuram - 695 019

**Dr. E. BHOJE GOWD**

Senior Scientist

Materials Science & Technology Division

+91471-2515474

+919048427911

## CERTIFICATE

*This is to certify that the work incorporated in this Ph.D. thesis entitled “Structural Changes Probed in Polymer-Solvent Systems at Molecular, Crystalline and Lamellar Length-Scales during Crystallization and Phase Transitions” submitted by Mr. Shaiju P to Academy of Scientific and Innovative Research (AcSIR), in partial fulfilment of the requirements for the award of the Degree of Doctor of Philosophy in Chemical Sciences, embodies original research work under my supervision and guidance at the Materials Science and Technology Division of the CSIR-National Institute for Interdisciplinary Science and Technology (CSIR-NIIST), Thiruvananthapuram. I further certify that this work has not been submitted to any other University or Institution in part or full for the award of any degree or diploma. Research material obtained from other sources has been duly acknowledged in the thesis. Any text, illustration, table etc., used in the thesis from other sources, have been duly cited and acknowledged.*

**Shaiju P**

Thiruvananthapuram  
June, 2017

**Dr. E. Bhoje Gowd**  
(Thesis Supervisor)

## ACKNOWLEDGEMENTS

*Foremost, I extend my deep sense of gratitude and indebtedness to Dr. E. Bhoje Gowd, my research supervisor and mentor, for his guidance, fruitful discussions, constant support and encouragement throughout my research career. His positive outlook and passion towards research have greatly inspired me and helped me to build confidence in my work. His teachings, motivation and advices were indispensable for whatever I have been able to do.*

*I sincerely thank Dr. A. Ajayaghosh, Director, NIIST, and former Directors Dr. Suresh Das and Dr. Gangan Pratap, for providing the necessary facilities and infrastructure to carry out this investigation.*

*My sincere thanks are also due to:*

- ❖ Dr. R. Luxmi Varma and Dr. Mangalam S. Nair, present and former AcSIR coordinators for the continuous support during my course work.*
- ❖ Dr. K. P. Surendran, Dr. Saju Pillai, Dr. Joshy Joseph, my DAC members for their insightful comments and encouragement.*
- ❖ Prof. N. Sanjeeva Murthy, Rutgers University, USA for sharing his expertise and for the sincere and valuable guidance extended to me.*
- ❖ Dr. A.R.R. Menon, Dr. V. S. Prasad, Dr. J. D. Sudha and Mr. M. Brahmakumar for their valuable help and suggestions.*
- ❖ Present group members Mr. Baku Nagendra, Ms. Deepthi Krishnan, Mrs. Sijla Rosely C V, Mrs. Angel Mary Joseph, Ms. Jerin K. Pancrecios, Mr. Sivaprasad, Mr. Amal Raj R. B and Ms. Praveena N. M and former group members Mr. Robinson C. Jose, Dr. S. Nagarajan, Dr. Kumari Nisha for the stimulating discussions and for all the fun we have had in the last five years.*
- ❖ All my friends in NIIST for their help and cooperation. I would like to mention many names here, but I am afraid that the list would become too long. I would also like to extend huge, warm thanks to my roommates.*
- ❖ Mr. Vishnu M. for AFM analysis and Mrs. Soumya for SEM analysis.*
- ❖ All technical and supportive staff of CSIR-NIIST for their timely help in the utilization of sophisticated analytical instruments.*
- ❖ All my teachers who stood as the source of inspiration in my early days and who taught me many things at different stages of my academic career.*

❖ *University Grants Commission (UGC) and Department of Science and Technology (DST), Government of India for financial assistance.*

*I am deeply and forever indebted to my parents, family members and all my friends for their constant source of love, inspiration and support. This accomplishment would not have been possible without them. Thank you.*

**Shaiju P**

# CONTENTS

	<b>Page</b>
<b>Declaration</b>	i
<b>Certificate</b>	iii
<b>Acknowledgements</b>	v
<b>Contents</b>	vii
<b>List of Abbreviations</b>	xiii
<b>Preface</b>	xv

---

<b>CHAPTER 1:</b>	<b>Introduction</b>	<b>01-31</b>
-------------------	---------------------	--------------

---

<b>1.1.</b>	Polymer Crystallization	1
<b>1.2.</b>	Hierarchical Structure of Semicrystalline Polymers	3
<b>1.3.</b>	Melt Crystallization	4
<b>1.4.</b>	Polymorphism	5
<b>1.4.1.</b>	Importance of Polymorphism	5
<b>1.4.2.</b>	Polymorphism in Polymers	6
<b>1.4.2.1.</b>	Poly lactide	6
<b>1.4.2.2.</b>	Syndiotactic Polystyrene	7
<b>1.5.</b>	Solvent-Induced Crystallization in Polymers	8
<b>1.6.</b>	Cocrystals	11
<b>1.7.</b>	Polymer Cocrystals	11
<b>1.7.1.</b>	Poly(vinyl alcohol)[PVA]-Iodine Complex	11
<b>1.7.2.</b>	Poly( <i>L</i> -lactide) [PLLA] Cocrystals	12

1.7.3.	Syndiotactic Polystyrene (sPS) Cocrystals	15
1.7.3.1.	Guest Exchange Process in sPS Cocrystals	16
1.7.3.2.	Guest Extraction Process in sPS Cocrystals	16
1.7.3.3.	Structural Transitions in sPS Cocrystal	17
1.8.	Polymer Single Crystals	21
1.9.	Lamellar Thickening	22
1.10.	Optical Properties of Polymers	23
1.11.	Applications of Nanoporous sPS	25
1.11.1.	Increased Shelf Life of Fruits and Vegetables	25
1.11.2.	Molecular Separations	25
1.12.	References	26

---

<b>CHAPTER 2:</b>	<b>Transparent and Crystalline Poly(L-lactide) prepared by Solvent-Induced Crystallization: Studies of Structural Reorganization during Heating</b>	<b>33-60</b>
-------------------	---	--------------

---

2.1.	Abstract	33
2.2.	Introduction	34
2.3.	Experimental	37
2.3.1.	Materials	37
2.3.2.	Sample Preparation	37
2.3.3.	Characterization	37
2.4.	Results and Discussion	39
2.4.1.	Solvent-Induced Crystallization of Amorphous PLLA in Various Solvents	39

2.4.2.	Morphology of Solvent-Crystallized PLLA Films	41
2.4.3.	Transparency of Solvent-Crystallized PLLA Films	47
2.4.4.	Structural Reorganization of Solvent-Crystallized PLLA Films during Heating	49
2.5.	Conclusions	56
2.6.	References	57
<hr/>		
<b>CHAPTER 3:</b>	<b>Poly(<i>L</i>-lactide) (PLLA) Cocrystals: Structural Changes on Multiple Length Scales during Cyclopentanone (CPO) Desorption in PLLA/CPO Cocrystals</b>	<b>61-89</b>
<hr/>		
3.1.	Abstract	61
3.2.	Introduction	62
3.3.	Experimental	64
3.3.1.	Materials	64
3.3.2.	Sample Preparation	64
3.3.3.	Characterization	64
3.4.	Results and Discussion	67
3.4.1.	Stability of PLLA Cocrystals at Room Temperature	67
3.4.2.	Thermal Behavior of PLLA/CPO Cocrystal ( $\epsilon$ )	69
3.4.3.	Crystalline Transition during Heating by <i>in-situ</i> WAXS	70
3.4.4.	Conformational Change by Temperature-Dependent FTIR	74
3.4.5.	Solvent Distribution by SANS	78
3.4.6.	Lamellar Morphology Changes during Heating by <i>in- situ</i> SAXS.	79

3.5.	Conclusions	85
3.6.	References	85

---

<b>CHAPTER 4:</b>	<b>Syndiotactic Polystyrene (sPS) Cocrystals: Structural Phase Transitions of sPS upon the Guest Exchange and Guest Extraction Processes</b>	<b>91-121</b>
-------------------	--	---------------

---

4.1.	Abstract	91
4.2.	Introduction	92
4.3.	Experimental	94
4.3.1.	Materials	94
4.3.2.	Sample Preparation	94
4.3.3.	Characterization	95
4.4.	Results and Discussion	95
4.4.1.	Guest Exchange Process Using Toluene Treated Amorphous Samples	95
4.4.2.	Guest Exchange Process Using Toluene Treated $\alpha$ form Samples	98
4.4.3.	Guest Exchange Process Using Toluene Treated $\gamma$ form Samples	102
4.4.4.	Guest Exchange Process Using Chloroform Treated Amorphous Samples	105
4.4.5.	Guest Exchange Process Using Chloroform Treated $\alpha$ form Samples	109
4.4.6.	Guest Exchange Process Using Chloroform Treated $\gamma$ form Samples	111
4.4.7.	Guest Extraction from Chloroform Treated Amorphous Samples	114

4.4.8.	Guest Extraction from Chloroform Treated $\gamma$ form Samples	116
4.5.	Conclusions	118
4.6.	References	119
<hr/>		
<b>CHAPTER 5:</b>	<b>Overall Summary</b>	<b>123-126</b>
<hr/>		
5.1.	Summary	123
5.2.	Future Perspectives	125
<hr/>		
<b>Papers Presented at Conferences</b>		127
<b>List of Publications</b>		129
<hr/>		



## List of Abbreviations

$\mu\text{m}$	Micrometer
$^{\circ}\text{C}$	Degree Celsius
1D	One-dimensional
2D	Two-dimensional
$\text{\AA}$	Angstrom
AFM	Atomic Force Microscopy
cm	Centimeter
CPO	Cyclopentanone
dCPO	Deuterated cyclopentanone
DMA	Dynamic mechanical analysis
DMF	N,N-dimethylformamide
DSC	Differential scanning calorimetry
DTA	Differential thermal analysis
FTIR	Fourier transform infrared spectroscopy
FWHM	Full width at half maximum
h	Hour
IR	Infrared
$K(z)$	One-dimensional electron density correlation function
KBr	Potassium Bromide
kV	Kilovolt
$L$	Long period
$l_a$	Amorphous thickness
$l_c$	Lamellar thickness
m.p.	Melting point
mA	Milliampere
min	Minutes
mm	Millimeter
$M_n$	Number-average molecular weight
$M_w$	Weight-average molecular weight
nm	Nanometer
PDI	Polydispersity Index

PDLA	Poly( <i>D</i> -lactide)
PEI	Polyethyleneimine
PLLA	Poly( <i>L</i> -lactide)
POM	Polarized Optical Microscopy
PVA	poly(vinyl alcohol)
Q	Invariant
SANS	small-angle neutron scattering
SAXS	Small-angle X-ray scattering
SEM	Scanning electron microscopy
sPS	Syndiotactic polystyrene
$T_c$	Crystallization temperature
$T_g$	Glass transition temperature
TGA	Thermogravimetric Analysis
THF	Tetrahydrofuran
$T_m$	Melting temperature
UV-Vis	Ultraviolet-visible
WAXS	Wide-angle X-ray scattering
XRD	X-ray diffraction

## PREFACE

Introducing an amorphous polymer into the atmosphere of an interacting solvent can help in the regularization of the polymer chains, which further leads to the crystallization of the polymer. This type of crystallization is termed as solvent-induced crystallization. This is complex phenomenon which involves solvent diffusion, followed by swelling and crystallization of the polymer. The presence of solvent molecules facilitates the segmental mobility of the polymer chains by reducing the glass transition temperature, which in turn allows the crystallization of polymer chains. Even though the melt processing technique is used for many practical applications, advanced applications need advanced polymer processing techniques such as spin-casting, electrospinning, wet spinning, and 3D printing, where the solvent is one of the essential ingredients in processing the polymers. Therefore, it is necessary to understand the interaction of solvents with the polymers. The main objective of the present thesis is to comprehend the effect of solvent interactions on the crystallization behaviour, polymorphism, cocrystals formation and guest exchange in cocrystals of certain semicrystalline polymers.

The thesis includes five chapters. The first chapter gives a brief introduction to the polymorphism and its influence on the properties of semicrystalline polymers. The chapter also explains the mechanism of solvent induced crystallization in semicrystalline polymers and its advantages. Further, the chapter elucidates the cocrystal formation by certain polymers, where the polymer acts as the host that accommodates the solvent molecules within its crystal lattice as the guest. The creation of nanoporous structures by the selective removal of the

solvent from the cocrystals and the applications of these structures and the cocrystals will also be discussed here in detail.

Chapter-II focuses on the solvent induced crystallization of poly(L-lactide) (PLLA) in the presence of different solvents. The structural and morphological changes during the treatment of PLLA with various solvents were followed by different characterization techniques. The PLLA films were found to crystallize into the  $\alpha$  form, irrespective of the solvent used for the crystallization. However, it showed interesting morphologies depending on the polymer-solvent interactions. PLLA films treated with acetone/H<sub>2</sub>O mixture exhibited a rodlike morphology. In addition the films showed better transparency due to the reduced surface roughness. On the other hand, PLLA films treated with acetone, THF and THF/water mixture showed spherulitic morphology. These films were found to be opaque or translucent in nature, due to the larger spherulite dimensions and high surface roughness. Moreover, a substantial increase in the long period values was observed for the solvent-treated PLLA films upon heating, especially at higher temperatures. This is referred as lamellar thickening. At elevated temperatures, the highly activated amorphous chains diffuse into the crystal growth front of the existing lamellae and finally adsorbed and recrystallized into the thicker crystals. The results obtained in this work will help in finding new routes to control the morphology of polymer films.

In Chapter-III, the structural changes in polymer-solvent complexes of PLLA with different solvents were studied. PLLA forms cocrystals ( $\epsilon$ ) with certain organic solvents such as cyclopentanone (CPO) by incorporating the solvent

molecules within its crystal lattice, at subambient temperatures. The transformation of this structure ( $\varepsilon$ ) into the  $\alpha$  form during solvent desorption and the accompanying changes in the structure at multiple length scales were studied by various characterization techniques. These studies show that the solvent desorption results in a precise sequence of quantifiable structural changes at multiple length scales.

Chapter IV discusses the effect of the host preparation method as well as the nature of guest molecules used for guest exchange in determining the structural phase transitions of syndiotactic polystyrene (sPS) upon guest exchange and guest extraction processes. To investigate this, sPS with different initial morphologies like amorphous,  $\alpha$  and  $\gamma$  forms were used for preparing cocrystals with chloroform and toluene. Such obtained cocrystals were further utilized for the guest exchange process with a series of n-alkanes and also for guest extraction. These studies were very helpful in understanding the conditions to prepare nanoporous crystalline materials with defined structures. Such nanoporous materials can be used as packaging materials since it improves the shelf life of fruits and vegetables by absorbing ethylene, molecular sensors, for chemical separation, etc.

Chapter V summarizes the overall concept of the thesis. The entire work emphasizes the importance of polymer-solvent interactions on the crystallization behavior and other properties of certain semicrystalline polymers. Depending on the polymer-solvent interactions, PLLA crystallizes into the  $\alpha$  form in certain solvents. Again the nature of solvent used for crystallization played a significant role in controlling the optical properties of PLLA. However, when the PLLA was

crystallized at subambient conditions, it favored the formation of cocrystals in certain solvents such as dimethylformamide, tetrahydrofuran and CPO. The intimate correlation between the crystal lattice and the lamellar structure was probed in PLLA cocrystals during the solvent desorption using various techniques. A systematic investigation was carried out on the factors that control the structure of sPS upon the guest exchange and guest extraction processes. Appropriate conditions were identified to attain nanoporous cavities as well as channels within the crystal lattice of sPS.

## Introduction

---

### 1.1. Polymer Crystallization

Crystallization in polymers is a widely investigated phenomenon, and it has contributed significantly to the growth of polymer science. In fact, the subject of polymer crystallization still receives considerable interest and studies are going on to understand the intricacies involved in the crystallization process. This is mainly due to the commercial importance and rapid advance of the polymer industry. Unlike small molecules, the inherent intriguing feature of macromolecules leads to a highly complex and divergent hierarchy that is a rather challenging task for theorists and experimentalists. Crystallization involves the alignment of polymer chains, where the polymer chains fold together to give ordered regions called lamellae. Crystallization of polymer chains was first identified in the year 1920 by the X-ray diffraction studies, carried out on synthetic and natural polymers.<sup>1</sup> The patterns were found to be broader compared to that of inorganic and low molecular weight materials. Crystallization has a strong influence on the physical and mechanical properties of polymers.

Amorphous films, which contain disordered polymer chains, are prepared by the sudden quenching of polymer melt below its glass transition temperature ( $T_g$ ). Even though the amorphous phase is considered as a chaotic phase, detailed studies showed that it might have some degree of order.<sup>2</sup> Instead of sudden quenching, if the polymer melt is cooled at a slower rate under appropriate conditions, depending on their chemical structure, some polymers crystallize by forming three-dimensional spherical structures called spherulites.<sup>3</sup> This kind of crystallization is termed as melt crystallization. Spherulites are developed by the growth of chain folded lamellae, which are oriented radially. That means the spherulites contain lamellar stacks arranged in radial directions. On the other hand,

if the crystallization happens by the heating of amorphous film above its  $T_g$ , it is called cold crystallization.

Crystallization process in polymers has a strong dependence on the nucleation behavior. Mainly there are two types of nucleation; Primary and secondary. Primary nucleation involves the formation of a nucleus (a small amount of crystalline material) within the melt due to the density fluctuations in the supercooled melt,<sup>4</sup> and the secondary nucleation involves the process of crystal growth that needs nucleation at the growing interface. The nucleus triggers the crystal growth in all directions, which will result in the formation of spherulites. Primary nucleation can happen in different ways. When the nucleation happens by the spontaneous aggregation of the polymer chains in a reversible way up to a certain point, beyond which the addition of chains is irreversible, the crystal starts to grow. Such type of nucleation is termed as homogeneous nucleation. It requires a large degree of supercooling. On the other hand, if the polymer chains aggregate at the interface of a foreign phase, it is called heterogeneous nucleation. The foreign phase can be a purposefully added nucleating agent or even an impurity. This type of nucleation needs only a small degree of supercooling. The crystallization rate can be effectively improved by the addition of nucleating agents since it increases the number of nucleating centers, which in turn increases the number of spherulites. Another kind of nucleation, which is called self-nucleation, was also reported.<sup>5</sup> This is a kind of primary nucleation where the nucleation originates from the presence of preexisting crystal that has survived from the earlier melting or dissolution process.<sup>5,6</sup>

In polymer crystallization, it was a subject of debate that how the long polymer chains are accommodated within the small crystallites. Based on the electron diffraction studies performed on gutta percha, Storks postulated that the total chain length is much larger compared to the film thickness.<sup>7</sup> He proposed a chain folded structure for the first time to explain the crystallization in such systems.<sup>7</sup> Later in 1957, Keller proved the concept of chain folding in different polymers such as polyethylenes, polyamides (nylons) and gutta percha, based on electron microscopy and electron diffraction studies.<sup>8</sup> He showed that the polymer

chain axes are perpendicular to the plane of the crystal. Since the length of the polymer chains is higher than the crystal thickness, the polymer chains might be folded.<sup>8</sup> Different theories were proposed to explain the chain folding during the crystallization process in polymers, and this topic has been reviewed by several researchers.<sup>7-11</sup>

## 1.2. Hierarchical Structure of Semicrystalline Polymers

The structure of semicrystalline polymers can be described at three different length scales. The dimensions of unit cell will be in fractions of nanometers. The information about the structure of unit cell can be obtained from the techniques such as wide-angle X-ray scattering (WAXS) and electron diffraction. The polymer chains adopt random coil conformation in the melt stage. However, during crystallization, the chains fold together to form ordered crystalline structures called lamellae. The lamellae are stitched together by disordered amorphous phase, which yields the semicrystalline structure. The thickness of the lamellae will be  $\sim 10$  nm with lateral dimensions in several  $\mu\text{m}$ . Small-angle X-ray scattering (SAXS) can be used to gather the information about the lamellar structure. The lamellae can be arranged in many ways. As mentioned earlier, the radial growth of lamellae results in the formation of three-dimensional superstructures called spherulites. Depending on the crystallization conditions, the dimensions of the spherulites may vary from  $\mu\text{m}$  to mm. The crystallization of the polymer from the melt mostly gives the spherulitic structure. The formation of spherulites can be observed using a polarized optical microscope (POM). Figure 1.1 shows the hierarchical structures in semicrystalline polymers.

Lamellar twisting is a common phenomenon that has been observed in many spherulites from the optical studies. Different reasons were proposed to explain the twisting. In one of them, the twisting is correlated to the continuous generation of screw dislocations and splaying of the new lamellae at the screw center may result in the reorientation of the lamellae. In another explanation, the lamellar twisting is ascribed to the asymmetry generated by the tilting of the chain, which causes different fold conformations in the top and bottom fold surfaces of

the lamellae. This introduces opposite bending moments between the two lamellar halves, which results in the twisting.

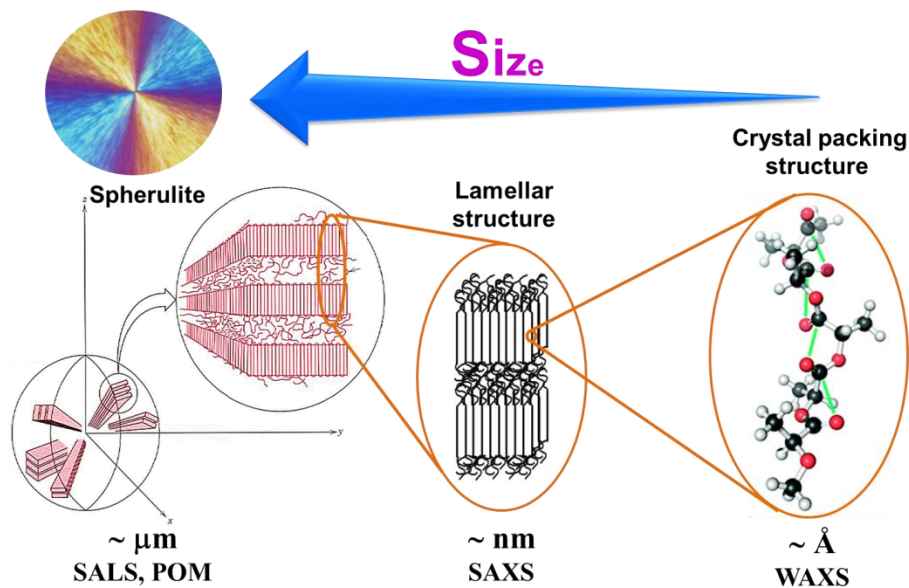
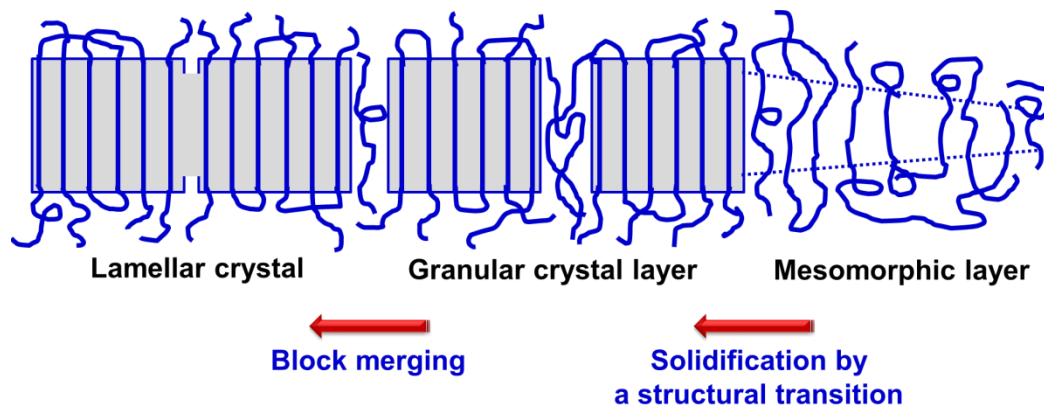


Figure 1.1. Schematic representation of structural hierarchy in semicrystalline polymers.

### 1.3. Melt Crystallization

The conversion of highly entangled melt stage into a semicrystalline state during the cooling process is termed as melt crystallization. Different theories were proposed to describe the crystallization of polymer from the melt.<sup>12-15</sup> According to Strobl's theory, the crystallization from the melt is a multistep process.<sup>16</sup> Figure 1.2 depicts the schematic illustration of the route of formation of polymer crystallites, as proposed by Strobl.<sup>16</sup> Here, the first step is the formation of the mesomorphic layer due to the density fluctuations, where the chain shows both orientation and mobility. The mobility of the chain decreases with the increase in the layer thickness. Once the critical thickness is reached solidification occurs, and the thickening stops at this point. Such obtained structure is denoted as "granular crystal layer." The final step is the merging of blocks to give a continuous lamellar crystal. This merging decreases the Gibbs free energy, which leads to the stabilization of the structure. However, the degree of stabilization varies with the change in the location. The thickness of the resulting crystal will be same as that of their constituent blocks.<sup>16</sup>



**Figure 1.2.** Schematic representation of the model proposed by Strobl for the formation of polymer crystallites. Adapted with permission from ref 16; Copyright 2000 EDP Sciences, Springer-Verlag, Società Italiana di Fisica.

## 1.4. Polymorphism

Polymorphism can be defined as the phenomenon that involves different packing arrangements, at least two, of the same molecule in the solid state.<sup>17, 18</sup> Polymorphs are assumed to be the different crystal forms of the same molecule, which show different arrangements. Due to the difference in the packing arrangements, polymorphs differ in their stability, melting point, density, solubility, color etc.<sup>18, 19</sup>

### 1.4.1. Importance of Polymorphism

Controlling polymorph formation has been a real concern in the chemical industry because of their entirely different properties. In the pharmaceutical industry, the change in the polymorphism is highly important since different polymorphs of the same drug show different solubility, which can affect the drug efficacy and safety.<sup>19</sup> The polymorphs can immediately change from a less stable form to a more stable form. The stable form will be the least soluble form in most cases. The change in polymorphism can occur at any time; for example, during the manufacturing process or even at the time of storage. The desired polymorph can be obtained by controlling the molecular recognition, kinetics, and thermodynamics. However, the methods reported for controlling the polymorphic forms have many drawbacks, and still, several studies are going on in this aspect.

## 1.4.2. Polymorphism in Polymers

Several polymers are known to exhibit polymorphism. In fact, it is believed that all the semicrystalline polymers can show polymorphism if the suitable conditions can be identified. As in the case of small molecules, the difference in the crystal structure of the polymers is due to the discrepancies in the packing arrangements, which depends on the crystallization conditions. A brief description of the polymorphic behavior exhibited by some polymers is given below

### 1.4.2.1. Polylactide

Polylactide (PLA) is a thermoplastic polymer from the polyester family with biodegradability and biocompatibility. It is produced from renewable resources.<sup>20, 21</sup> Because of its biocompatible nature, PLA can be used for drug delivery applications and as bioimplants. Since the conventional, non-biodegradable plastic materials used for the packaging are creating adverse environmental effects, PLA can be used as an effective alternative because it gives harmless degradable products. There are two ways to prepare PLA. One is condensation of lactic acid, which will give brittle, low molecular weight product. The second and most used way is the ring opening polymerization of lactide, a dimer of lactic acid, which gives high molecular weight PLA.<sup>22</sup>

Lactic acid, the monomer of PLA, exists in two optically active forms, L-lactic acid and D-lactic acid, due to the presence of an asymmetric carbon atom. If the polymer is made from pure L form, it is called poly(L-lactide) (PLLA) and if it is made from pure D form, it is called poly(D-lactide) [PDLA]. PLLA is the most commonly used isomer of PLA.

PLLA is known to exist in different crystal forms depending on the variation in the crystallization conditions. The  $\alpha$  form is the most common crystalline form of PLLA, which is obtained by normal melt or solution crystallization. De Santis et al. reported the presence of the  $\alpha$  form in PLLA for the first time.<sup>23</sup> Zhang et al. discovered that when PLLA is crystallized below 120 °C, another crystalline form, which they termed as the  $\alpha'$  form, is obtained.<sup>24</sup> The chain conformation of the  $\alpha'$  is similar to that of the  $\alpha$  form, whereas it shows a

slightly disordered chain packing. Later, it was reported that the crystallization of PLLA below 100 °C would lead to the formation of pure  $\alpha'$  form. When the PLLA is crystallized between 100 and 120 °C, a mixture of  $\alpha$  and  $\alpha'$  is obtained.<sup>25, 26</sup> Due to its loose packing, the  $\alpha'$  form shows poor barrier properties and lower modulus compared to the  $\alpha$  form.<sup>27</sup> Another disordered crystalline form of the  $\alpha$  form, which is the  $\alpha''$  form, was discovered by Marubayashi et al. in 2008. It was obtained by the crystallization of PLLA under 3-15 MPa CO<sub>2</sub> at 0-20 °C and under 7-15 MPa CO<sub>2</sub> at 30 °C.<sup>28</sup>

Eling et al. reported another crystalline form  $\beta$ , which is prepared by stretching the  $\alpha$  form at relatively high draw ratio at high temperature.<sup>29, 30</sup> The thermal stability of the  $\beta$  form is poor compared to the  $\alpha$  form since the melting point of the  $\beta$  form is around 10 °C less than that of the  $\alpha$  form.<sup>30</sup> A frustrated structure was suggested for the  $\beta$  form by Puiggali et al.,<sup>31</sup> in which three chains are accommodated in a trigonal cell, and the chains are arranged randomly up and down. The same group has also reported one more crystalline form  $\gamma$ , which is more ordered.<sup>32</sup> The  $\gamma$  form is typically obtained by the epitaxial crystallization of PLLA on a substrate like hexamethylbenzene. PLLA was also reported to form cocrystals ( $\epsilon$ ) with certain solvents at subambient temperatures.<sup>33</sup> Along with homocrystals PLLA and PDLA, the formation of stereocomplex was also reported, where the crystal cell is made up of one chain of PLLA and one chain of PDLA.<sup>34</sup> Stereocomplex shows higher thermal stability compared to the homocrystals because of its higher melting temperature ( $\sim 50^\circ\text{C}$  greater than that of homocrystals).

#### 1.4.2.2. Syndiotactic Polystyrene

Syndiotactic polystyrene (sPS) is one of the most studied polymers due to its complex polymorphic behavior. sPS has five major crystalline forms namely  $\alpha$ ,  $\beta$ ,  $\gamma$ ,  $\delta$  and  $\epsilon$  along with some mesophases and sub-modifications.<sup>35-51</sup>  $\alpha$  and  $\beta$  forms are obtained by the thermal treatment of amorphous sPS, and these forms contain hexagonal and orthorhombic unit cells, respectively, with all-trans

conformation ( $T_4$ ).<sup>37, 40, 42</sup> The  $\alpha$  form is again classified into two;  $\alpha'$  (limiting disordered) and  $\alpha''$  (limiting ordered).<sup>36, 38, 40</sup> Similarly, the  $\beta$  form is also subdivided as limiting disordered  $\beta'$ , and limiting ordered  $\beta''$ .<sup>36, 38-40, 42, 52</sup> On the other hand, solvent treatment of amorphous films yield  $\gamma$ ,  $\delta$  and  $\varepsilon$  forms.<sup>35, 37, 53-61</sup> Solvent-induced crystallization in polymers will be discussed elaborately in the next section.

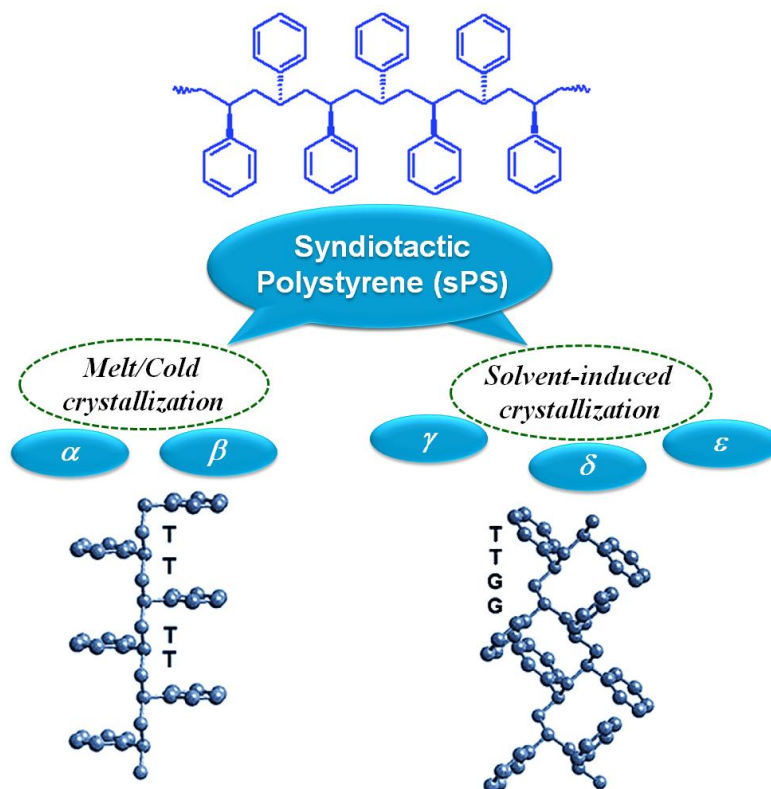


**Figure 1.3.** Polymorphism exhibited by syndiotactic polystyrene (sPS).

### 1.5. Solvent-Induced Crystallization in Polymers

Solvent-induced crystallization of polymers is an important subject from both scientific and technological perspectives. Solvents have frequently been encountered with polymers during polymerization and processing steps. Most of the advanced applications of polymers need advanced polymer processing techniques such as spin-casting, electrospinning, wet spinning, and 3D printing, where the solvent is one of the essential ingredients in processing the polymers. There have been significant efforts to understand the solvent-induced crystallization of semicrystalline polymers. Generally, crystal growth rate  $G$  in

melt-grown crystals is nucleation controlled process and exponentially depends on  $1/T\Delta T$ ; and for solution-grown crystals, the growth rate  $G$  is diffusion-controlled and linearly proportional to supercooling  $\Delta T$ .<sup>62, 63</sup>

Solvent induced crystallization involves the diffusion of solvent into the polymer matrix, swelling of the polymer, and crystallization. As the name implies, here the crystallization is triggered by the solvent molecules. Several factors like temperature, pressure, solvent chemistry, etc. can affect the rate or extent of the process. The interaction of the solvent molecules unsettle the intermolecular cohesive forces between polymer chains, which reduces the  $T_g$  and facilitates the segmental mobility.<sup>64</sup> The extent of interaction between the polymer and the solvent depends on the starting properties of the polymer like molecular weight, crystallinity orientation, etc. and also on the properties of the solvents like solubility parameter, polarity, hydrogen bonding ability, etc. Match in the solubility parameters of the polymer and the solvent is an important factor that determines the crystallization of the polymer. If the difference between the solubility parameters of the polymer and the solvent is within one unit, the polymer will dissolve in that solvent.<sup>65</sup>

Tashiro and co-workers investigated the solvent-induced crystallization of syndiotactic polystyrene (sPS) and demonstrated that the accelerating rate of molecular motion of the amorphous chain and the formation rate of crystalline domains are dependent on the nature of the solvent used for the crystallization of the polymer. The mechanism of solvent induced crystallization in sPS is shown Figure 1.4. As shown in the figure, the solvent molecules induce the micro-Brownian motion in polymer chains due to the plasticizing effect. This motion triggers the formation of short helices, which further grow into long helices. Tashiro and co-workers measured the  $T_g$  of sPS in different solvent environments using both FTIR and molecular dynamics calculations and showed that the  $T_g$  was shifted to sub ambient temperatures ( $-80$  to  $-20$  °C) depending on the solvent used for the swelling experiments.

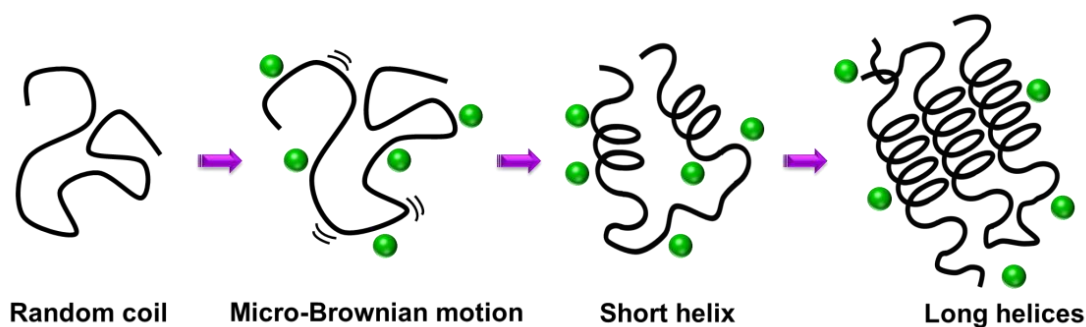


**Figure 1.4.** Schematic representation of solvent induced crystallization of sPS (Inspired by the work of Tashiro et al. *Macromolecules* 2002, 35, 410-414).<sup>66</sup>

Depending on the nature of the interaction between the polymer and solvent molecules, there are two possibilities as represented in Figure 1.5. In one case the solvent molecules only induce the crystallization by facilitating the segmental mobility, and in the other case, the solvent molecules are trapped within the crystal lattice of the polymer during the crystallization. Thus obtained structures are called polymer cocrystals. Extensive studies have been carried out to understand the solvent-induced crystallization behavior of polymers such as syndiotactic polystyrene, poly(ethylene terephthalate), poly(ethylene imine), etc.

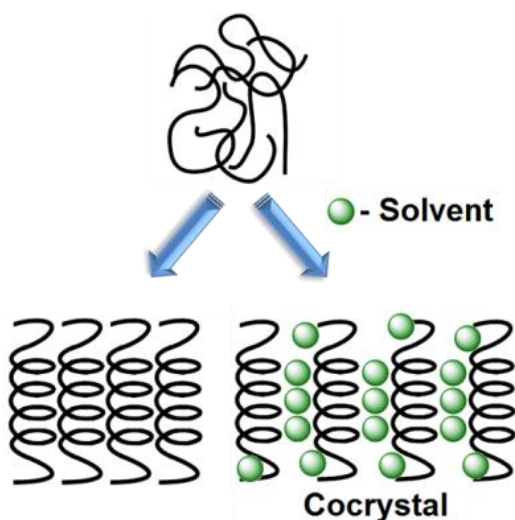


**Figure 1.5.** Schematic diagram showing the different possibilities of solvent induced crystallization of amorphous sPS.

Cocrystal formation in small molecules is a well-studied phenomenon. A brief description about the cocrystals is given below

## 1.6. Cocrystals

As per the definition proposed by FDA, “Cocrystals are solids that are crystalline materials composed of two or more molecules within the same crystal lattice.” The interaction between the molecules in the cocrystal can be hydrogen bonding,  $\pi$  stacking, van der Waals forces, etc. Cocrystals have a broad range of applications especially is in the field of pharmaceutical industry. Some of the advantages of cocrystals are their thermodynamic stability, they can improve the solubility of poorly water-soluble drugs, and there is no need to make or break covalent bonds.

## 1.7. Polymer Cocrystals

Polymer-solvent complexes and intercalates (cocrystals) are produced through the cocrystallization, or in a broader sense, through the co-organization of polymer chains with solvent or small molecules. These systems can be designated as polymer-solvent compounds, crystallosolvates and intercalates. Typically, these systems form either through molecular recognition or specific molecular interactions. While these systems were known for decades for biological polymers, forming mainly complexes, such as cellulose, amylose, its occurrence with synthetic polymers is much more recent.

In polymer cocrystals, the polymer molecule acts as host that accommodates a low molecular mass guest within its crystal lattice. Several polymers are recognized to form cocrystals. Some examples are poly(vinyl alcohol) (PVA),<sup>67, 68</sup> poly(L-lactide) [PLLA],<sup>33</sup> syndiotactic polystyrene (sPS)<sup>37</sup> etc.

### 1.7.1. Poly(vinyl alcohol)[PVA]-Iodine Complex

PVA-Iodine complexes are prepared by dipping an oriented or unoriented PVA film into an aqueous solution of potassium iodide and iodine. If the concentration of iodine is less (0.01–0.1 M), the complex will be formed mainly in the amorphous region.<sup>67</sup> However, at higher concentrations (0.1–1 M), the complex will be formed in the crystalline region also.<sup>67, 68</sup> Two types of such complexes, named as complex I and complex II, are reported, depending on the

variation in the concentration of iodine.<sup>69, 70</sup> PVA-iodine complex is a widely used optical polarizer since it is inexpensive compared to the other type of polarizers. It is used in photographic filters, liquid crystal display, sunglasses etc.<sup>71</sup>

### 1.7.2. Poly(L-lactide) [PLLA] Cocrystals

Cocrystal formation is a recent observation in PLLA crystallization. In 2012, Marubayashi et al. discovered that PLLA forms solvent complex with specific organic solvents like N, N-dimethylformamide (DMF) and tetrahydrofuran (THF), etc. at subambient temperatures.<sup>33</sup> They termed the new crystalline form as “ $\varepsilon$ .” In the cocrystal, PLLA chains exhibit  $10_7$  (left-handed  $10_3$ ) helical conformation and are accommodated in an orthorhombic lattice with unit cell parameters  $a = 1.5\text{--}1.6$  nm,  $b = 1.2\text{--}1.3$  nm,  $c = 2.8\text{--}2.9$  nm, and  $\alpha = \beta = \gamma = 90^\circ$ .<sup>33</sup> The  $\varepsilon$  cocrystal is less stable and transforms into the  $\alpha$  form with solvent desorption. The crystal structure proposed for PLLA/DMF cocrystal is shown in Figure 1.6.

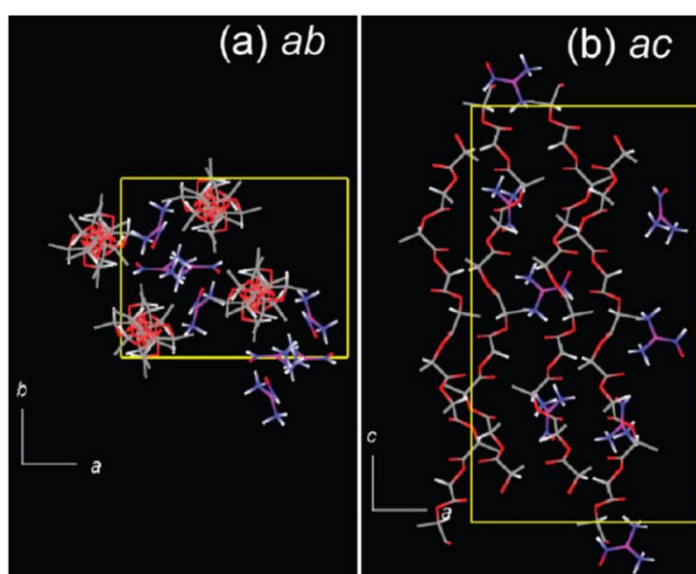


**Figure 1.6.** Packing model of PLLA chains and DMF molecules in the  $\varepsilon_{\text{DMF}} (I_{\text{DMF}})_R$ : (a) ab- and (b) ac-projections. Carbon atoms in PLLA chains and DMF molecules are shown by gray and blue, respectively. The unit cell is shown by a yellow rectangle. Reprinted with permission from ref 33; Copyright 2012 American Chemical Society.

DMF molecules are incorporated in the channel shaped cavities formed by the PLLA chains along the c-axis direction. The relatively short diameter of the

channel-shaped cavity might be the reason for the selectivity of solvents in the complexation. The interactions between PLLA and DMF were confirmed with the help of FTIR analysis, and they proposed that large numbers of such weak interactions are responsible for the stability of PLLA/DMF complex.<sup>33</sup>

Crystal to crystal transition in PLLA cocrystals was also investigated by the same group using wide angle X-ray diffraction and Fourier transform infrared spectroscopy.<sup>72</sup> They tried to understand the crystal transition during solvent exchange in CO<sub>2</sub> and solvent complexes. In addition, guest-induced transitions of  $\alpha$ ,  $\alpha'$ , and  $\alpha''$ , which are noncomplex crystals, were also investigated in detail. A schematic representation of the crystal to crystal transition between two polymorphs selected from the PLLA-CO<sub>2</sub> complex, PLLA-solvent complexes, and,  $\alpha$ ,  $\alpha'$ , and  $\alpha''$  is shown in Figure 1.7

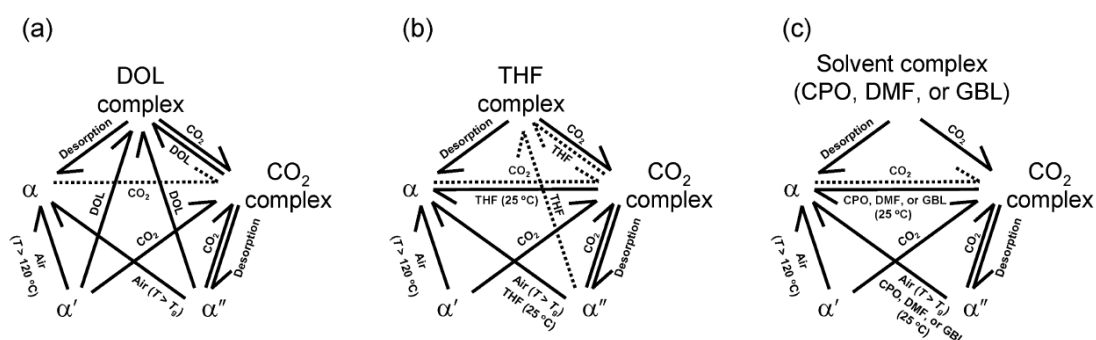


**Figure 1.7.** Schematic illustration showing the transition behavior between two polymorphs selected from the solvent complex, CO<sub>2</sub> complex, and noncomplex crystals ( $\alpha$ ,  $\alpha'$ , and  $\alpha''$ ). (a) DOL exposure was conducted only at -25 °C. (b) THF without labeling of temperature (e.g., CO<sub>2</sub> complex → THF complex) means THF exposure at -25 °C. (c) Results of exposure to CPO, DMF, and GBL at -25 °C were not shown, because of relatively low solubility of these three solvents in the PLLA film at -25 °C. Each broken line represents that completion of the transition was not obtained (mixture with other crystal structure). Reprinted with permission from ref 72; Copyright 2013 American Chemical Society.

The solvent exchange carried out at -25 °C was found to be successful, even though it showed some dependence on the solvent used for the process. An increase in the content of  $\alpha$  form was observed with the rise in the solvent exchange temperature. The studies on the transition behavior between CO<sub>2</sub> and different solvent complexes revealed that the transition from solvent complex to the CO<sub>2</sub> complex is complete for all the complexes. On the other hand, the

transition from CO<sub>2</sub> complex to the solvent complex was found to be affected by the nature of the solvent and the surrounding temperature. The guest induced transitions of noncomplex crystals,  $\alpha$ ,  $\alpha'$ , and  $\alpha''$ , were found to have a strong correlation with the order of the crystal and the kind of guest molecules used.<sup>72</sup>

Rizzo et al. proposed the structure of PLLA/CPO cocrystal based on the X-ray diffraction analyses.<sup>73</sup> According to them, PLLA takes 10/7 helical conformation in the cocrystal, and 16 CPO molecules are accommodated in an orthorhombic lattice with unit cell parameters  $a = 1.61$  nm,  $b = 1.26$  nm, and  $c = 2.90$  nm, according to the space group  $P2_12_12_1$ . The proposed schematic model is given in Figure 1.8. They also reported that the solvents that are capable of inducing cocrystal formation in PLLA could generate uniplanar orientations by low-temperature sorption in amorphous films.<sup>73</sup>

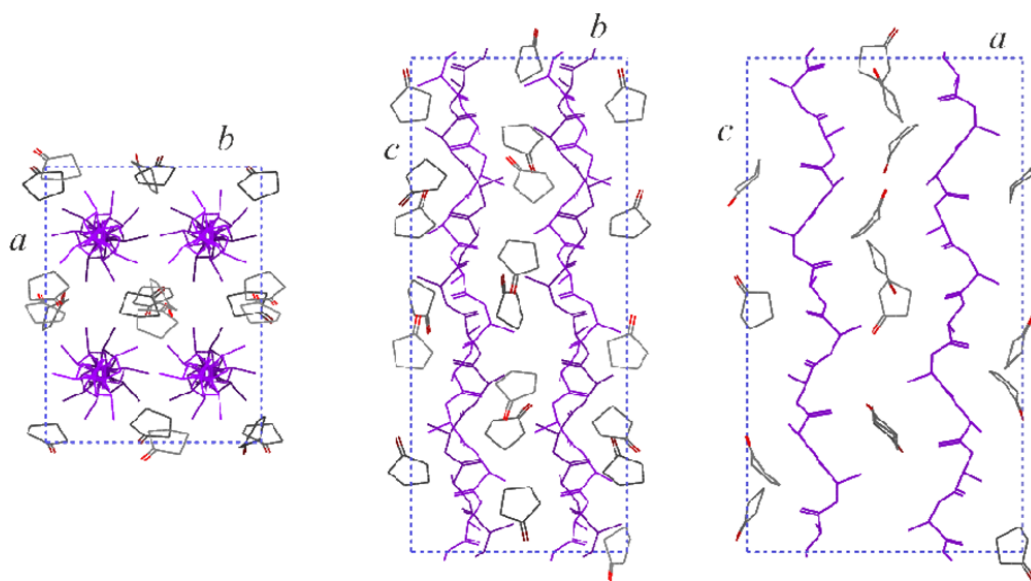


**Figure 1.8.** Schematic representation of the packing model for the PLLA-CPO cocrystalline form in an orthorhombic unit cell with parameters  $a = 1.61$  nm,  $b = 1.26$  nm, and  $c$  (chain axis) = 2.90 nm, according to the symmetry of the space group  $P2_12_12_1$ : projection along the  $c$  axis,  $a$  axis and  $b$  axis. PLLA helical chains are reported in magenta. Reprinted with permission from ref 73; Copyright 2015, American Chemical Society.

Gel formation by PLLA was also reported in the presence of certain solvents.<sup>74, 75</sup> Gels were obtained by cooling the PLLA solution prepared at higher temperatures in particular solvents that are capable of producing PLLA cocrystals. The solvent in the gel can be exchanged with certain other solvents by treating the

gel with the corresponding solvents.<sup>74</sup> Thermal stability of the gels was also investigated by heating. The structure was found to be transformed from  $\varepsilon$  to  $\alpha$ , with the rise in the temperature.<sup>74</sup>

### 1.7.3. Syndiotactic Polystyrene (sPS) Cocrystals

Cocrystal formation of sPS with different solvent molecules and the structural changes associated with solvent exchange and solvent extraction processes have been well documented in the literature.<sup>37, 43, 47, 48, 56, 76, 77</sup> Solvent treatment of amorphous sPS gives  $\gamma$ ,  $\delta$  and  $\varepsilon$  forms depending on the polymer-solvent interactions and the preparation conditions. All these crystalline forms exhibit the same  $[-(T_2G_2)_2-]$  helical  $s(2/1)2$  conformation.<sup>35, 37, 53-61</sup> Among these three crystalline forms,  $\delta$  and  $\varepsilon$  forms contain solvent molecules inside their crystal lattice. Hence they can be termed as cocrystals. On the other hand,  $\gamma$  form does not contain solvent molecules within its crystal lattice even though the conformation is similar to  $\delta$  and  $\varepsilon$  cocrystals.<sup>78</sup> Furthermore, sPS cocrystals were classified based on the difference in the interlayer spacing ( $d_{010}$ ) as shown in Figure 1.9.

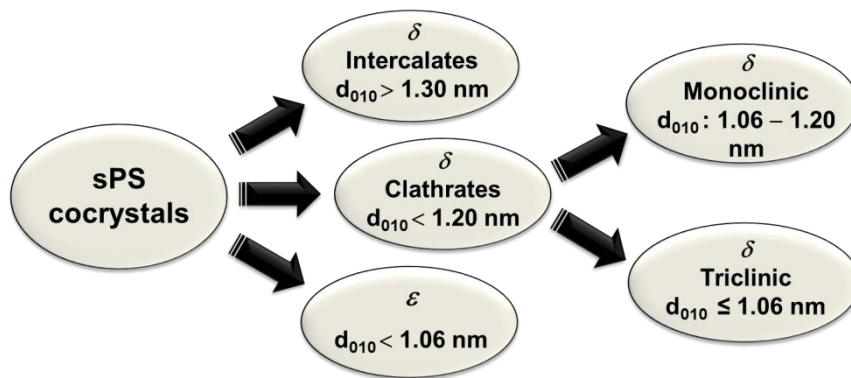


**Figure 1.9.** Classification of sPS cocrystals

Depending on the difference in the monomeric unit to a guest molecule ratio,  $\delta$  cocrystal is classified as  $\delta$  clathrates and  $\delta$  intercalates.<sup>35, 37, 79-82</sup> In  $\delta$  clathrates, the ratio of monomeric unit to a guest is 4:1. Here the guest molecules are trapped within the isolated cavities present in the crystal lattice of sPS.<sup>35, 37, 53-58</sup> On the other hand, the monomer to guest ratio is 2:1 in  $\delta$  intercalates. Here the guest molecules are arranged between the polymer helices and are not trapped

inside the cavities.<sup>35, 37, 79-81, 83</sup> Based on the size and shape of the guest molecules, which affects the  $d_{010}$  spacing,  $\delta$  clathrates are again subdivided into  $\delta$  monoclinic and  $\delta$  triclinic.<sup>84, 85</sup> In  $\varepsilon$  cocrystal, the guest molecules are accommodated in channel shaped cavities, in such a way that the planes of the guest molecules will be roughly parallel to the polymer helices.<sup>48, 76, 86</sup>

### 1.7.3.1. Guest Exchange Process in sPS Cocrystals

sPS cocrystals are relatively stable at room temperature. Nevertheless, it is possible to exchange the guest molecules with certain other solvents, by keeping the cocrystal in the corresponding solvent atmosphere.<sup>87-94</sup> Guest exchange process is strongly influenced by the properties of the guest molecules and the polymer-guest interactions.<sup>89</sup> It is a useful technique to incorporate certain functional molecules into the crystal lattice, which is difficult with the aid of typical solution cast or solvent induced crystallization.<sup>95</sup>

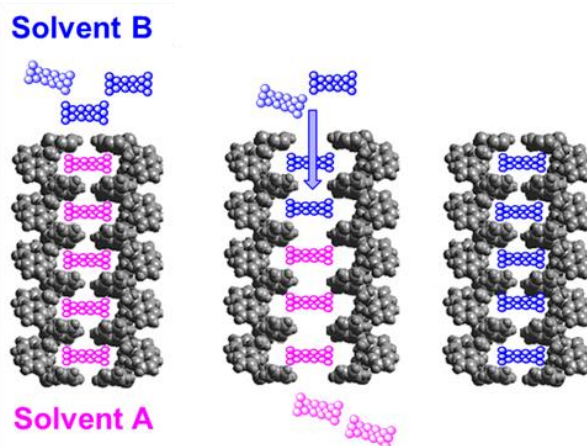


Figure 1.10. Schematic representation of guest exchange process in sPS cocrystals.

### 1.7.3.2. Guest Extraction Process in sPS Cocrystals

Nanoporous structures can be prepared by the selective removal of solvent from the crystal lattice of  $\delta$  and  $\varepsilon$  cocrystals, which give nanoporous  $\delta$  ( $\delta_e$ ),<sup>47, 77, 96</sup> and nanoporous  $\varepsilon$  ( $\varepsilon_e$ ) forms, respectively.<sup>48, 97</sup>  $\delta_e$  can be prepared by dipping the  $\delta$  cocrystal in acetone and further rinsing in methanol<sup>85, 86</sup> or by dipping in acetonitrile.<sup>48, 49</sup>  $\varepsilon_e$  can also be prepared by same methods.<sup>49</sup> Treating with supercritical CO<sub>2</sub> is another method, which is used to produce nanoporous sPS.<sup>98, 99</sup>

The cavities and the channels are created within the crystal lattice, and the helical structure is retained as such. Since these nanoporous structures have the capability to absorb molecules like CO<sub>2</sub> and H<sub>2</sub><sup>100, 101</sup> as well as organic molecules,<sup>49, 102</sup> they are used as molecular sensors,<sup>103-106</sup> molecular sieves,<sup>102, 107-109</sup> etc. Applications of nanoporous sPS will be discussed later.

### 1.7.3.3. Structural Transitions in sPS Cocrystal

Thermally induced structural changes in sPS cocrystals have been discussed elaborately in the literature.<sup>53, 96, 97, 110, 111</sup> Most of the studies focus on the transition behavior of  $\delta$ . It was reported that the  $\delta$  form transforms to the  $\gamma$  form by heating above the  $T_g$ , which results in the expulsion of the solvent molecules from the crystal lattice.<sup>53, 112</sup> However, the polymer chain conformation is retained even after the solvent exclusion. There are several reports, which discuss the phase transition from  $\delta$  to  $\gamma$ .<sup>58, 89, 110, 113</sup> Gowd et al. investigated the structural changes in uniaxially drawn  $\delta$  and  $\delta_e$  forms of sPS during heating using simultaneous WAXS and small-angle X-ray scattering (SAXS) measurements.<sup>59</sup> They observed that the  $\delta$  form transforms to the  $\gamma$  form in a temperature range of 100–130 °C, without disturbing the stacked lamellar structure much. When the temperature reaches around 190–200 °C, the  $\gamma$  form transforms to a mixture of  $\alpha$  and  $\beta$  forms. Schematic representation of the structural changes in  $\delta$  form on heating is given in Figure 1.11.<sup>61</sup> Initially, the  $\delta$  form transforms to the  $\gamma$  form along with a small fraction of  $\beta$ . The solvent molecules excluded from the  $\delta$  form crystal lattice are remained in the amorphous region transiently and are responsible for the formation of the  $\beta$  form in a relatively low temperature region. On further heating, the  $\gamma$  form transforms to the  $\alpha$  form by retaining the small fraction of  $\beta$ .

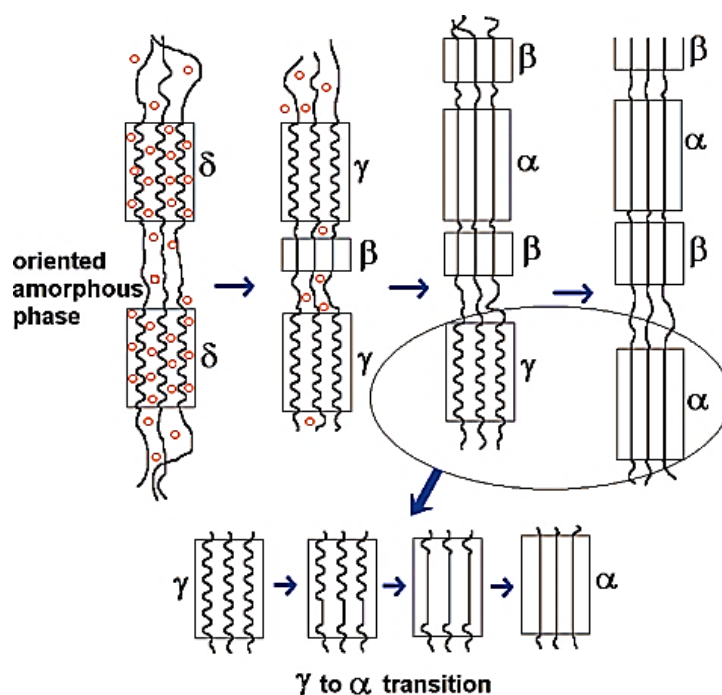


**Figure 1.11.** Schematic illustration of structural change in the phase transition from  $\delta$  to  $\gamma$  ( $\beta$ ) to  $\alpha$  ( $\beta$ ) form. The straight solid lines indicate the all-trans zigzag conformation, the curved lines indicate the helical conformation, and the small circles indicate the solvent molecules. Enlarged picture shown in the lower side illustrates the transition from the  $\gamma$  to  $\alpha$  form. Reprinted with permission from ref 61; Copyright 2007 American Chemical Society.

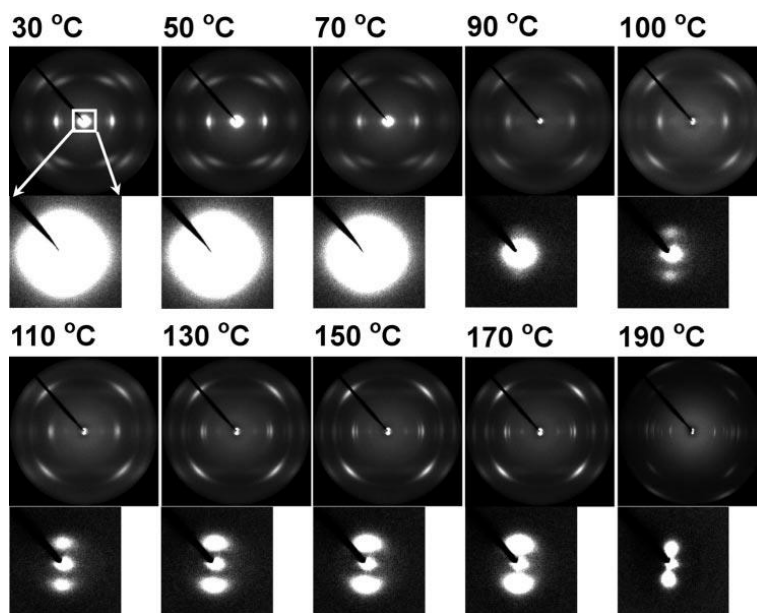


**Figure 1.12.** Temperature dependence of the WAXS and SAXS patterns measured simultaneously using a single imaging plate for the uniaxially oriented  $\delta_e$  form of the sPS/chloroform complex in the heating process. SAXS patterns are expanded and showed below the respective WAXS pattern for the purpose of clarity. The draw axis is along the vertical direction. Reprinted with permission from ref 59; Copyright 2008 American Chemical Society.

On the other hand, simultaneous WAXS/SAXS measurements of  $\delta_e$  revealed that there is a major reorganization of the stacked lamellar structure.<sup>59</sup> Two-dimensional (2D) WAXS and SAXS patterns obtained at different temperatures for the uniaxially oriented  $\delta_e$  form of the sPS/chloroform complex in the heating process are shown in Figure 1.12.<sup>59</sup> In 2D SAXS pattern of  $\delta_e$ , a strong diffused scattering was observed at room temperature due to the presence of empty cavities in the crystal lattice.

The changes in the one-dimensional (1D) profile scanned along the equatorial direction in 2D WAXS, and meridional direction in 2D SAXS are shown in Figure 1.13. In the WAXS results, new patterns, different from  $\delta_e$  and  $\gamma$ , were observed in the temperature range 70–100 °C. This is related to the formation of an intermediate phase. In the corresponding SAXS pattern, the intensity of the diffused scattering has started to decrease at 70 °C and almost disappeared at 100 °C. This indicates the disappearance of the cavities and the appearance of the intermediate form. As the temperature increases beyond 130 °C, considerable changes were observed in the 1D WAXS patterns, which indicate the formation of  $\gamma$ . When the temperature reaches around 190–200 °C, the  $\gamma$  form transforms to  $\alpha$  and as a result, an entirely different WAXS and SAXS patterns were observed in this temperature range.

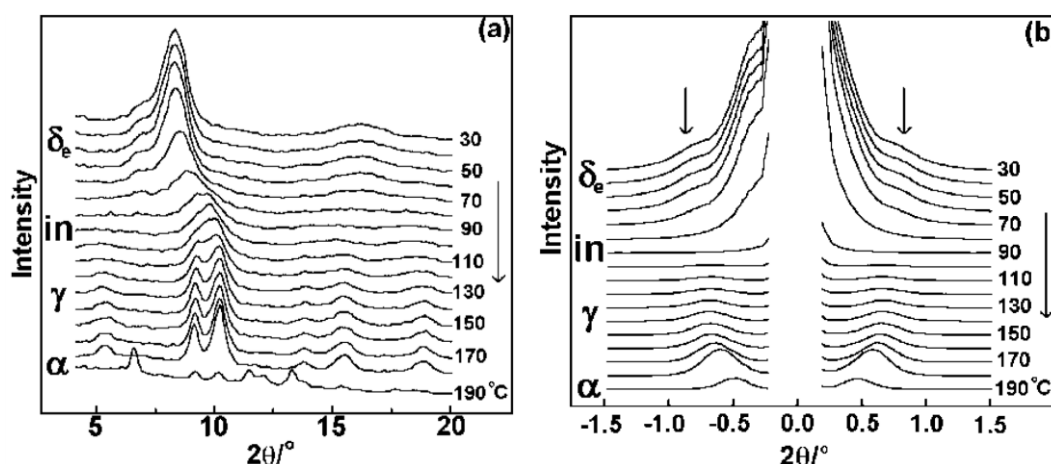


**Figure 1.13.** Temperature dependence of X-ray diffraction profile on the (a) equatorial line (WAXS) and (b) meridional line (SAXS). Reprinted with permission from ref 59; Copyright 2008 American Chemical Society.

Schematic representation of the phase transition of the  $\delta_e$  form upon heating is shown in Figure 1.14. The X-ray and DSC results are also shown for comparison. In region (a) only the  $\delta_e$  form with cavities having  $T_2G_2$  helical conformation is present. In region (b), due to the increase in the temperature, the cavities started to disappear, and as a result, a slight disorder in the chain packing was observed. The formation of disordered structure was further confirmed by the appearance of the endothermic peak in the DSC diagram at this temperature region. Therefore, in this region, both  $\delta_e$  form and the intermediate phase coexist. On further increase in the temperature, the cavities will disappear completely, and the disordered chains will come together to form more tightly packed structure. As a result, in region (c), the  $\gamma$  form started to appear along with the intermediate phase. The ordering in the structure was evidenced by the appearance of exothermic peak in the DSC diagram. Region (d) represents the complete transformation of the structure into the  $\gamma$  form.<sup>96</sup>

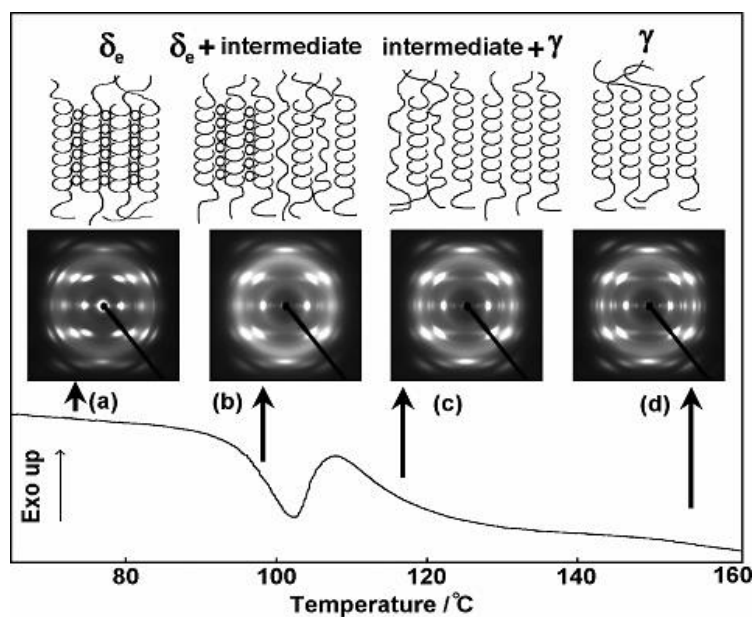


**Figure 1.14.** Schematic illustration of the chain-packing mode at different temperatures during heating of the  $\delta_e$  form sample in comparison with the observed X-ray fiber diagram and DSC thermogram. Reprinted with permission from ref 96; Copyright 2006 American Chemical Society.

In some reports, the direct transformation from  $\delta$  to  $\beta$ , without passing through  $\gamma$  is also mentioned.<sup>38, 114</sup> This transformation occurs by rapid heating or

annealing of the  $\delta$  form. Gowd et al. reported the presence of  $\beta$  form along with  $\gamma$  form above 140 °C. This is related to the vigorous motion of the amorphous phase, which is induced by the solvent molecules present in this region.<sup>54</sup> They also found that the content of  $\beta$  has increased with the increase in the thickness of the film. In thicker samples, the solvent content will be more, and as the temperature increases, all these solvent molecules will be ejected into the amorphous region, which in turn enhances the formation of  $\beta$ . However, in the thermal transitions of  $\varepsilon$ , the structure was found to be transforming directly to  $\gamma$  form at intermediate temperatures, without going through the intermediate phase.<sup>97</sup>

### 1.8. Polymer Single Crystals

The formation of polymer single crystals was first observed in the case of polyethylene (PE) during the crystallization on cooling dilute solutions, where it was found to form lozenge shaped single crystals similar to paraffin single crystals.<sup>8, 115</sup> In dilute solutions the possibility of the chain overlap is insignificant, and therefore the possibility of intermolecular entanglements can be ruled out. As a result, the polymer chain segments can readily diffuse towards the crystal growth face. Morphologies similar to the single crystal were also found to occur in more concentrated solutions<sup>116</sup> and even after the melt crystallization<sup>117</sup> of certain polymers. In the single crystals, the polymer chains fold back and forth to form lamellae with thickness  $\sim 10$  nm.<sup>8, 115</sup> The direction of the polymer chains was found to be nearly normal to the lamellar surface. In fact, the idea of chain folding was emerged by the discovery of single crystals,<sup>8</sup> even though the concept of chain folding was already formulated by Storks in 1938.<sup>7</sup> Since the thickness of the crystals is only  $\sim 10$  nm, and the length of the PE chains is much larger ( $\geq 1$   $\mu\text{m}$ ) compared to the crystal thickness, the polymer chains must be folded.

Comprehensive crystallographic information can be obtained with the help of single crystals since it gives a direct visualization of the polymer chains. As already mentioned, several polymers are known to exist in different polymorphic forms, and some of these polymorphs cannot be subjected to mechanical forces since they are unstable. Therefore the crystal structure analysis using conventional

fiber techniques becomes difficult due to the difficulty in making fibers. However, it is possible to obtain the single crystals of some these crystal modifications, which makes the structural investigation possible.

### 1.9. Lamellar Thickening

The ability of polymer crystals to increase the thickness and hence the fold length during heating, above their initial crystallization temperature is termed as lamellar thickening. This can be considered as the tendency of the polymer chains to move towards the lowest free energy state by reducing the number of folds and hence energy so that they can attain the optimum state. However, under normal conditions, it is difficult to achieve such optimum state with fully extended chain configuration. It has been noticed that the lamellar thickening will be more evident and faster at higher temperatures. Two mechanisms have been proposed to explain the lamellar thickening; melt recrystallization and sliding diffusion mechanisms.<sup>118-121</sup> In the *melt*-recrystallization, the thickening is due to either melting or partial melting of the crystalline domains, and subsequent recrystallization.<sup>121</sup> Sliding diffusion mechanism relates the lamellar thickening to the chain sliding along the chain axis between the adjacent lamellae in the crystal lattice, which results in the rearrangement of the polymer chains.<sup>118, 119</sup> The thickness of the lamellae is almost doubled according to sliding diffusion mechanism. Dreyfus and Keller elucidated the lamellar doubling with the help of fold-dislocation thickening model, as shown in Figure 1.15.<sup>119, 122</sup>

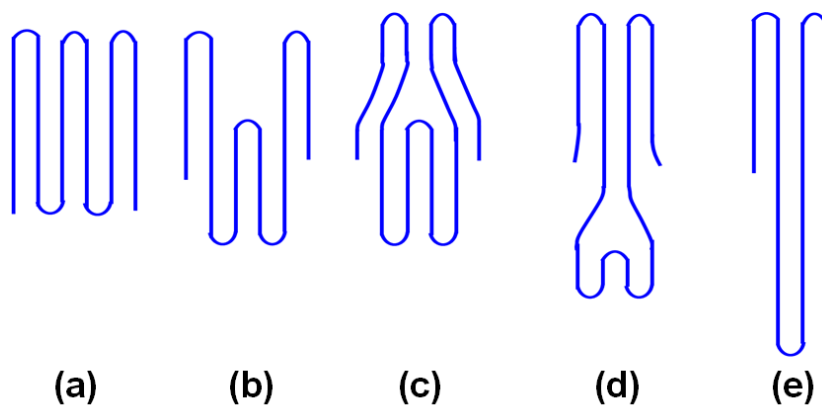


**Figure 1.15.** Schematic representation of lamellar doubling proposed by Dreyfus and Keller. Adapted with permission from ref 122; Copyright 1970 John Wiley & Sons, Inc.

Another model was proposed by Rastogi et al. to explain the doubling phenomenon as displayed in Figure 1.16.<sup>123</sup> However, this model allows the possibility of only one doubling since the chains get mutually entangled at the doubled crystalline surface. This was different from the model proposed by Barham and Keller, where they showed the probability of tripling and quadrupling of the lamellar thickness.<sup>124</sup>

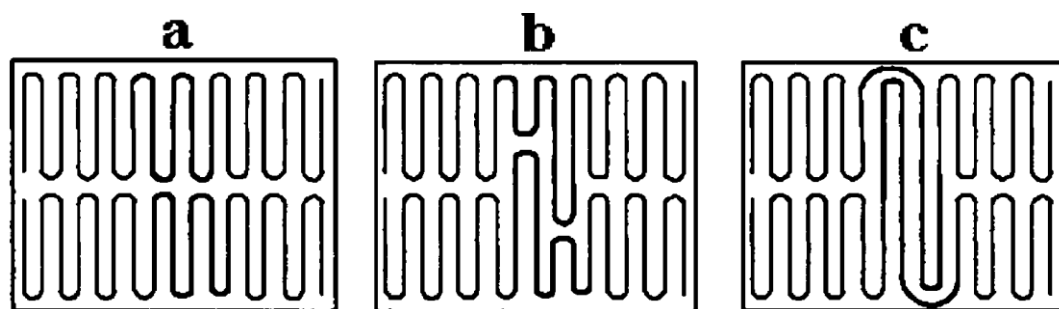


**Figure 1.16.** Schematic model to explain the doubling phenomenon in the regularly stacked adjacent lamellae. The bold line represents the test chain. Reprinted with permission from ref 123; Copyright 1997 American Chemical Society.

## 1.10. Optical Properties of Polymers

Polymers differ in their transparency from crystal clear to completely opaque. The basic structure of the polymer has a substantial impact on the transparency or opaqueness of the polymer. The opaqueness can be related to the light scattering from the surface as well as from the interior of the polymer film. The bulk or interior scattering is mainly due to the variations in refractive index. Mostly amorphous polymers will be transparent due to the single refractive index of the amorphous phase. On the other hand, semicrystalline polymers will be opaque due to the different densities and hence different refractive indices of the crystalline and amorphous region. However, there are some exceptions. Poly 4-methyl pentene-1, a highly crystalline polymer, was found to be transparent in nature. This transparent nature is due to the equal densities of the amorphous and the crystalline regions. Due to the similar densities of the crystalline and amorphous regions, the difference in the refractive index will be less, which in turn helps in the smooth transmission of light.

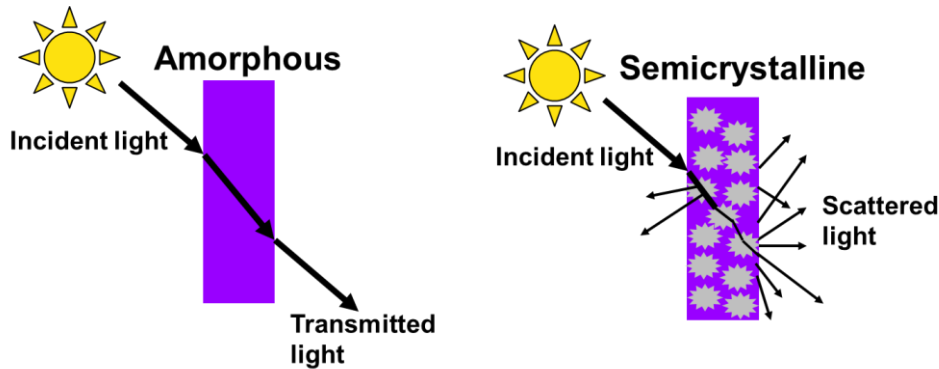


**Figure 1.17.** Schematic representation of light transmission in amorphous and semicrystalline polymers.

Apart from the difference in the densities, the presence of internal voids can also affect the transparency in polymers. The intensity of scattering depends on the size of the voids. The whitening observed during the stretching of a polymer film or while performing a simple tensile test is mostly due to the formation of voids. Transparency changes in semicrystalline polymers can also be correlated with the formation of spherulites. If the dimensions of the spherulites are larger than the wavelength of the incident light, it will not allow the light to pass through it. Considerable improvement in the transparency can be brought about by reducing the dimensions of the spherulites below the wavelength of light. If the size of the spherulites matches with the wavelength of the light, the transparency of the material will improve due to the effective transmission of light. Clarifiers or nucleating agents are often added to polymers to promote the formation of small spherulites.<sup>125, 126</sup>

Surface properties can also affect the transparency in semicrystalline polymers. Scattering arising from the surface roughness of the film can contribute to the opaqueness of the film.<sup>127</sup> Surface roughness might be due to extrusion roughness and crystallization roughness.<sup>127, 128</sup> As the name indicates the extrusion roughness is attributable to the generation of surface defects during the extrusion process after the resin has come out of the die. Crystallization roughness can be related to the formation of crystallization aggregates formed on the surface of the film.

---

---

## 1.11. Applications of Nanoporous sPS

### 1.11.1. Increased Shelf Life of Fruits and Vegetables

Ethylene is an important component in plant life since it regulates many diverse metabolic activities in plants and it plays an important role in the production of enzymes that cause ripening. But ethylene can significantly affect the post-harvest life and quality of fruits and vegetables. Therefore, it is necessary to reduce the content of ethylene to improve the post-harvest quality of fruits and vegetables. Nanoporous sPS showed high solubility and low diffusivity of ethylene due to the formation of cocrystal, where the ethylene molecules are arranged perpendicular to the direction of polymer helices.<sup>129</sup> Recently Sicari et al. studied the effect of packaging material on the maintenance of the quality of oranges.<sup>130</sup> The oranges were wrapped in biaxially oriented polypropylene (BOPP) and nanoactive films with a core layer of nanoporous sPS and kept at 6 °C and 80% relative humidity for 45 days. Oranges stored in BOPP film showed mold development after 30 days. On the other hand, the mold formation has started only after 45 days for the fruits stored in the nanoactive film. This is due to the ability of the nanoactive films to absorb a greater amount of ethylene produced during respiration of the fruit.<sup>130</sup>

### 1.11.2. Molecular Separations

Nanoporous sPS can be used for the effective removal of volatile organic compounds (VOCs) from air and water due to their capability to accommodate apolar molecules and to exclude the highly polar water molecules. VOCs such as 1,2-dichloroethane, 1,2-dibromoethane, and 1,1,2,2-tetrachloroethane, in spite of their difference in mass, boiling temperature and volume, were reported to form cocrystals with sPS.<sup>131</sup> The cocrystals formed were found to have a very low diffusivity as well. Most of these solvent uptake studies were performed using nanoporous  $\delta$  due to the lower absorption ability of the  $\varepsilon$  form. However, the  $\varepsilon$  form can be used for the absorption of long organic compounds, which cannot be absorbed by the small cavities of the  $\delta$ .

## 1.12 References

- (1) Katz, J. *Kolloid Z* **1925**, 37, 19-22.
- (2) Miller, R. L.; Boyer, R. F. *J. Polym. Sci.: Polym. Phys. Ed.* **1984**, 22, 2043-2050.
- (3) Bassett, D. C., *Principles of polymer morphology*. CUP Archive: 1981.
- (4) Gibbs, J. W., *The scientific papers of J. Willard Gibbs*. Longmans, Green and Company: 1906; Vol. 1.
- (5) Blundell, D. J.; Keller, A.; Kovacs, A. J. *J. Polym. Sci. B* **1966**, 4, 481-486.
- (6) Wunderlich, B., CHAPTER V - The Nucleation Step. In *Macromolecular Physics*, Academic Press: 1976; pp 1-114.
- (7) Storks, K. H. *J. Am. Chem. Soc.* **1938**, 60, 1753-1761.
- (8) Keller, A. *Philos. Mag.* **1957**, 2, 1171-1175.
- (9) Till, P. *J. Polym. Sci.* **1957**, 24, 301-306.
- (10) Fischer, E. *Z. Naturforsch.* **1957**, 753-4.
- (11) Flory, P. *J. Am. Chem. Soc.* **1962**, 84, 2857-2867.
- (12) Hoffman, J. D. *Polym. Eng. Sci.* **1964**, 4, 315-362.
- (13) Sadler, D. M. *J. Polym. Sci.: Polym. Phys. Ed.* **1985**, 23, 1533-1554.
- (14) Sadler, D.; Gilmer, G. *Phys. Rev. Lett.* **1986**, 56, 2708.
- (15) Bower, D. I., *An Introduction to Polymer Physics*. Cambridge University Press: 2002.
- (16) Strobl, G. *Eur. Phys. J. E* **2000**, 3, 165-183.
- (17) Threlfall, T. L. *Analyst* **1995**, 120, 2435-2460.
- (18) Desiraju, G. R. *Cryst. Growth Des.* **2008**, 8, 3-5.
- (19) Llinàs, A.; Goodman, J. M. *Drug Discovery Today* **2008**, 13, 198-210.
- (20) Drumright, R. E.; Gruber, P. R.; Henton, D. E. *Adv. Mater.* **2000**, 12, 1841-1846.
- (21) Garlotta, D. *J. Polym. Environ.* **2001**, 9, 63-84.
- (22) Mehta, R.; Kumar, V.; Bhunia, H.; Upadhyay, S. N. *J. Macromol. Sci., Part C* **2005**, 45, 325-349.
- (23) De Santis, P.; Kovacs, A. J. *Biopolymers* **1968**, 6, 299-306.
- (24) Zhang, J.; Duan, Y.; Sato, H.; Tsuji, H.; Noda, I.; Yan, S.; Ozaki, Y. *Macromolecules* **2005**, 38, 8012-8021.
- (25) Kawai, T.; Rahman, N.; Matsuba, G.; Nishida, K.; Kanaya, T.; Nakano, M.; Okamoto, H.; Kawada, J.; Usuki, A.; Honma, N.; Nakajima, K.; Matsuda, M. *Macromolecules* **2007**, 40, 9463-9469.

- 
- (26) Zhang, J.; Tashiro, K.; Tsuji, H.; Domb, A. J. *Macromolecules* **2008**, *41*, 1352-1357.
- (27) Cocca, M.; Lorenzo, M. L. D.; Malinconico, M.; Frezza, V. *Eur. Polym. J.* **2011**, *47*, 1073-1080.
- (28) Marubayashi, H.; Akaishi, S.; Akasaka, S.; Asai, S.; Sumita, M. *Macromolecules* **2008**, *41*, 9192-9203.
- (29) Eling, B.; Gogolewski, S.; Pennings, A. J. *Polymer* **1982**, *23*, 1587-1593.
- (30) Hoogsteen, W.; Postema, A. R.; Pennings, A. J.; Ten Brinke, G.; Zugenmaier, P. *Macromolecules* **1990**, *23*, 634-642.
- (31) Puiggali, J.; Ikada, Y.; Tsuji, H.; Cartier, L.; Okihara, T.; Lotz, B. *Polymer* **2000**, *41*, 8921-8930.
- (32) Cartier, L.; Okihara, T.; Ikada, Y.; Tsuji, H.; Puiggali, J.; Lotz, B. *Polymer* **2000**, *41*, 8909-8919.
- (33) Marubayashi, H.; Asai, S.; Sumita, M. *Macromolecules* **2012**, *45*, 1384-1397.
- (34) Ikada, Y.; Jamshidi, K.; Tsuji, H.; Hyon, S. H. *Macromolecules* **1987**, *20*, 904-906.
- (35) Milano, G.; Guerra, G. *Prog. Mater. Sci.* **2009**, *54*, 68-88.
- (36) Woo, E. M.; Sun, Y. S.; Yang, C. P. *Prog. Polym. Sci.* **2001**, *26*, 945-983.
- (37) Gowd, E. B.; Tashiro, K.; Ramesh, C. *Prog. Polym. Sci.* **2009**, *34*, 280-315.
- (38) Guerra, G.; Vitagliano, V. M.; De Rosa, C.; Petraccone, V.; Corradini, P. *Macromolecules* **1990**, *23*, 1539-1544.
- (39) De Rosa, C. *Macromolecules* **1996**, *29*, 8460-8465.
- (40) Cartier, L.; Okihara, T.; Lotz, B. *Macromolecules* **1998**, *31*, 3303-3310.
- (41) De Rosa, C.; Rapacciuolo, M.; Guerra, G.; Petraccone, V.; Corradini, P. *Polymer* **1992**, *33*, 1423-1428.
- (42) Chatani, Y.; Shimane, Y.; Ijitsu, T.; Yukinari, T. *Polymer* **1993**, *34*, 1625-1629.
- (43) Chatani, Y.; Shimane, Y.; Inoue, Y.; Inagaki, T.; Ishioka, T.; Ijitsu, T.; Yukinari, T. *Polymer* **1992**, *33*, 488-492.
- (44) Chatani, Y.; Shimane, Y.; Inagaki, T.; Ijitsu, T.; Yukinari, T.; Shikuma, H. *Polymer* **1993**, *34*, 1620-1624.
- (45) De Rosa, C.; Rizzo, P.; de Ballesteros, O.; Petraccone, V.; Guerra, G. *Polymer* **1999**, *40*, 2103-2110.
- (46) Rizzo, P.; Albulnia, A. R.; Guerra, G. *Polymer* **2005**, *46*, 9549-9554.

- 
- (47) De Rosa, C.; Guerra, G.; Petraccone, V.; Pirozzi, B. *Macromolecules* **1997**, *30*, 4147-4152.
- (48) Rizzo, P.; Daniel, C.; De Girolamo Del Mauro, A.; Guerra, G. *Chem. Mater.* **2007**, *19*, 3864-3866.
- (49) Petraccone, V.; Ruiz de Ballesteros, O.; Tarallo, O.; Rizzo, P.; Guerra, G. *Chem. Mater.* **2008**, *20*, 3663-3668.
- (50) Auriemma, F.; Petraccone, V.; Dal Poggetto, F.; De Rosa, C.; Guerra, G.; Manfredi, C.; Corradini, P. *Macromolecules* **1993**, *26*, 3772-3777.
- (51) Ouchi, T.; Nagasaka, S.; Hotta, A. *Macromolecules* **2011**, *44*, 2112-2119.
- (52) Woo, E. M.; Sun, Y. S.; Lee, M. L. *Polymer* **1999**, *40*, 4425-4429.
- (53) Gowd, E. B.; Nair, S. S.; Ramesh, C. *Macromolecules* **2002**, *35*, 8509-8514.
- (54) Gowd, E. B.; Tashiro, K. *Macromolecules* **2007**, *40*, 5366-5371.
- (55) Tashiro, K.; Ueno, Y.; Yoshioka, A.; Kobayashi, M. *Macromolecules* **2000**, *34*, 310-315.
- (56) Kobayashi, M.; Nakaoki, T.; Ishihara, N. *Macromolecules* **1989**, *22*, 4377-4382.
- (57) Tashiro, K.; Yoshioka, A. *Macromolecules* **2001**, *35*, 410-414.
- (58) Immirzi, A.; de Candia, F.; Iannelli, P.; Zambelli, A.; Vittoria, V. *Makromol. Chem. Rapid. Commun.* **1988**, *9*, 761-764.
- (59) Gowd, E. B.; Shibayama, N.; Tashiro, K. *Macromolecules* **2008**, *41*, 2541-2547.
- (60) Gowd, E. B.; Nair, S. S.; Ramesh, C.; Tashiro, K. *Macromolecules* **2003**, *36*, 7388-7397.
- (61) Gowd, E. B.; Shibayama, N.; Tashiro, K. *Macromolecules* **2007**, *40*, 6291-6295.
- (62) Leung, W. M.; St. John Manley, R.; Panaras, A. R. *Macromolecules* **1985**, *18*, 760-771.
- (63) Cheng, S. Z. D.; Chen, J.; Heberer, D. P. *Polymer* **1992**, *33*, 1429-1436.
- (64) Rebenfeld, L.; Makarewicz, P. J.; Weigmann, H.-D.; Wilkes, G. L. *J. Macromol. Sci., Part C* **1976**, *15*, 279-393.
- (65) Sperling, L. H., *Introduction to physical polymer science*. John Wiley & Sons: 2005.
- (66) Tashiro, K.; Yoshioka, A. *Macromolecules* **2002**, *35*, 410-414.
- (67) Miyasaka, K., PVA-Iodine complexes: Formation, structure, and properties. In *Structure in Polymers with Special Properties*, Zachmann, H. G., Ed. Springer Berlin Heidelberg: Berlin, Heidelberg, 1993; pp 91-129.

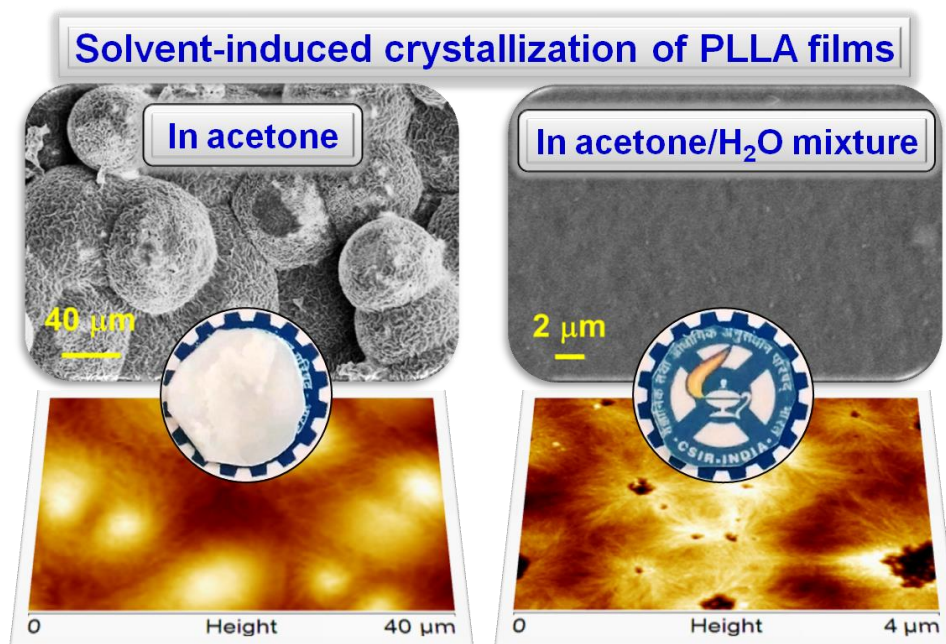
- 
- (68) Haisa, M.; Itami, H. *J. Phys. Chem.* **1957**, *61*, 817-818.
- (69) Choi, Y.-S.; Oishi, Y.; Miyasaka, K. *Polym J* **1990**, *22*, 601-608.
- (70) Tashiro, K.; Kitai, H.; Saharin, S. M.; Shimazu, A.; Itou, T. *Macromolecules* **2015**, *48*, 2138-2148.
- (71) <https://en.wikipedia.org/wiki/Polarizer>
- (72) Marubayashi, H.; Asai, S.; Sumita, M. *J. Phys. Chem. B* **2013**, *117*, 385-397.
- (73) Rizzo, P.; Ianniello, G.; Venditto, V.; Tarallo, O.; Guerra, G. *Macromolecules* **2015**, *48*, 7513-7520.
- (74) Matsuda, Y.; Fukatsu, A.; Wang, Y.; Miyamoto, K.; Mays, J. W.; Tasaka, S. *Polymer* **2014**, *55*, 4369-4378.
- (75) Matsuda, Y.; Fukatsu, A.; Tasaka, S. *Chem. Lett.* **2013**, *42*, 1046-1047.
- (76) Tarallo, O.; Schiavone, M. M.; Petraccone, V.; Daniel, C.; Rizzo, P.; Guerra, G. *Macromolecules* **2010**, *43*, 1455-1466.
- (77) Milano, G.; Venditto, V.; Guerra, G.; Cavallo, L.; Ciambelli, P.; Sannino, D. *Chem. Mater.* **2001**, *13*, 1506-1511.
- (78) Ma, W.; Yu, J.; He, J. *Macromolecules* **2004**, *37*, 6912-6917.
- (79) Petraccone, V.; Tarallo, O.; Venditto, V.; Guerra, G. *Macromolecules* **2005**, *38*, 6965-6971.
- (80) Tarallo, O.; Petraccone, V.; Venditto, V.; Guerra, G. *Polymer* **2006**, *47*, 2402-2410.
- (81) Malik, S.; Rochas, C.; Guenet, J. M. *Macromolecules* **2006**, *39*, 1000-1007.
- (82) Gowd, E. B.; Tashiro, K.; Ramesh, C. *Macromolecules* **2008**, *41*, 9814-9818.
- (83) Daniel, C.; Deluca, M. D.; Guenet, J. M.; Brûlet, A.; Menelle, A. *Polymer* **1996**, *37*, 1273-1280.
- (84) Tarallo, O.; Petraccone, V.; R. Alburnia, A.; Daniel, C.; Guerra, G. *Macromolecules* **2010**, *43*, 8549-8558.
- (85) Tarallo, O.; Auriemma, F.; de Ballesteros, O. R.; Di Girolamo, R.; Diletto, C.; Malafrente, A.; De Rosa, C. *Macromol. Chem. Phys.* **2013**, *214*, 1901-1911.
- (86) Daniel, C.; Montefusco, T.; Rizzo, P.; Musto, P.; Guerra, G. *Polymer* **2010**, *51*, 4599-4605.
- (87) Uda, Y.; Kaneko, F.; Kawaguchi, T. *Polymer* **2004**, *45*, 2221-2229.
- (88) Uda, Y.; Kaneko, F.; Kawaguchi, T. *Macromolecules* **2005**, *38*, 3320-3326.
- (89) Yoshioka, A.; Tashiro, K. *Macromolecules* **2003**, *36*, 3593-3600.

- 
- (90) Kaneko, F.; Kashihara, N.; Tsuchida, T.; Okuyama, K. *Macromol. Rapid Commun.* **2010**, *31*, 554-557.
- (91) Uda, Y.; Kaneko, F.; Kawaguchi, T. *Macromolecules* **2005**, *38*, 3380-3385.
- (92) Gowd, E. B.; Tashiro, K. *Polymer* **2011**, *52*, 822-829.
- (93) Jose, R. C.; Shaiju, P.; Nagendra, B.; Gowd, E. B. *Polymer* **2013**, *54*, 6617-6627.
- (94) Tarallo, O.; Schiavone, M. M.; Petraccone, V. *Polymer* **2011**, *52*, 1426-1435.
- (95) Uda, Y.; Kaneko, F.; Kawaguchi, T. *Macromol. Rapid Commun.* **2004**, *25*, 1900-1904.
- (96) Gowd, E. B.; Shibayama, N.; Tashiro, K. *Macromolecules* **2006**, *39*, 8412-8418.
- (97) Rizzo, P.; D'Aniello, C.; De Girolamo Del Mauro, A.; Guerra, G. *Macromolecules* **2007**, *40*, 9470-9474.
- (98) Reverchon, E.; Guerra, G.; Venditto, V. *J. Appl. Polym. Sci.* **1999**, *74*, 2077-2082.
- (99) Ma, W.; Yu, J.; He, J. *Macromolecules* **2005**, *38*, 4755-4760.
- (100) Figueroa-Gerstenmaier, S.; Daniel, C.; Milano, G.; Vitillo, J. G.; Zavorotynska, O.; Spoto, G.; Guerra, G. *Macromolecules* **2010**, *43*, 8594-8601.
- (101) Figueroa-Gerstenmaier, S.; Daniel, C.; Milano, G.; Guerra, G.; Zavorotynska, O.; Vitillo, J. G.; Zecchina, A.; Spoto, G. *Phys. Chem. Chem. Phys.* **2010**, *12*, 5369-5374.
- (102) Manfredi, C.; Del Nobile, M. A.; Mensitieri, G.; Guerra, G.; Rapacciuolo, M. *J. Polym. Sci., Part B: Polym. Phys.* **1997**, *35*, 133-140.
- (103) Mensitieri, G.; Venditto, V.; Guerra, G. *Sens. Actuators, B* **2003**, *92*, 255-261.
- (104) Pilla, P.; Iadicicco, A.; Contessa, L.; Campopiano, S.; Cutolo, A.; Giordano, M.; Guerra, G.; Cusano, A. *IEEE Photonics Technol. Lett.* **2005**, *17*, 1713-1715.
- (105) Pilla, P.; Cusano, A.; Cutolo, A.; Giordano, M.; Mensitieri, G.; Rizzo, P.; Sanguigno, L.; Venditto, V.; Guerra, G. *Sensors* **2009**, *9*, 9816-9857.
- (106) Buono, A. M.; Immediata, I.; Rizzo, P.; Guerra, G. *J. Am. Chem. Soc.* **2007**, *129*, 10992-10993.
- (107) Mahesh, K. P. O.; Sivakumar, M.; Yamamoto, Y.; Tsujita, Y.; Yoshimizu, H.; Okamoto, S. *J. Membr. Sci.* **2005**, *262*, 11-19.
- (108) Daniel, C.; Alfano, D.; Venditto, V.; Cardea, S.; Reverchon, E.; Larobina, D.; Mensitieri, G.; Guerra, G. *Adv. Mater.* **2005**, *17*, 1515-1518.
- (109) Tanigami, K.; Ishii, D.; Nakaoki, T.; Stroeve, P. *Polym J* **2013**, *45*, 1135-1139.
- (110) Vittoria, V.; de Candia, F.; Iannelli, P.; Immirzi, A. *Makrom. Chem. Rapid Commun.* **1988**, *9*, 765-769.

- 
- (111) Manfredi, C.; De Rosa, C.; Guerra, G.; Rapacciuolo, M.; Auriemma, F.; Corradini, P. *Macromol. Chem. Phys.* **1995**, *196*, 2795-2808.
- (112) De Candia, F.; Guadagno, L.; Vittoria, V. *J. Macromol. Sci., Part B: Phys.* **1995**, *34*, 95-103.
- (113) Yoshioka, A.; Tashiro, K. *Macromolecules* **2003**, *36*, 3001-3003.
- (114) Rastogi, S.; Goossens, J. G. P.; Lemstra, P. J. *Macromolecules* **1998**, *31*, 2983-2998.
- (115) Jaccodine, R. *Nature* **1955**, *176*, 305-306.
- (116) Bassett, D. C.; Keller, A.; Mitsuhashi, S. *Journal of Polymer Science Part A: General Papers* **1963**, *1*, 763-788.
- (117) Geil, P.; Doremus, R.; Roberts, B.; Turnbull, D., Growth and Perfection of Crystals. Wiley, New York: 1958.
- (118) Peterlin, A. *J. Polym. Sci. B* **1963**, *1*, 279-284.
- (119) Dreyfuss, P.; Keller, A. *J. Macromol. Sci., Part B: Phys.* **1970**, *4*, 811-835.
- (120) Yao, Y. F.; Graf, R.; Spiess, H. W.; Rastogi, S. *Macromolecules* **2008**, *41*, 2514-2519.
- (121) Mandelkern, L.; Sharma, R. K.; Jackson, J. F. *Macromolecules* **1969**, *2*, 644-647.
- (122) Dreyfus, P.; Keller, A. *J. Polym. Sci. B* **1970**, *8*, 253-258.
- (123) Rastogi, S.; Spoelstra, A. B.; Goossens, J. G. P.; Lemstra, P. J. *Macromolecules* **1997**, *30*, 7880-7889.
- (124) Barham, P. J.; Keller, A. *J. Polym. Sci., Part B: Polym. Phys.* **1989**, *27*, 1029-1042.
- (125) Tenma, M.; Mieda, N.; Takamatsu, S.; Yamaguchi, M. *J. Polym. Sci., Part B: Polym. Phys.* **2008**, *46*, 41-47.
- (126) Blomenhofer, M.; Ganzleben, S.; Hanft, D.; Schmidt, H.-W.; Kristiansen, M.; Smith, P.; Stoll, K.; Mäder, D.; Hoffmann, K. *Macromolecules* **2005**, *38*, 3688-3695.
- (127) Stehling, F. C.; Speed, C. S.; Westerman, L. *Macromolecules* **1981**, *14*, 698-708.
- (128) Ashizawa, H.; Spruiell, J. E.; White, J. L. *Polym. Eng. Sci.* **1984**, *24*, 1035-1042.
- (129) Alburnia, A. R.; Minucci, T.; Guerra, G. *J. Mater. Chem.* **2008**, *18*, 1046-1050.
- (130) Sicari, V.; Dorato, G.; Giuffrè, A. M.; Rizzo, P.; Alburnia, A. R. *J. Food Process Preserv.* **2016**, e13168-n/a.
- (131) Alburnia, A. R.; Oliva, P.; Grassi, A. *J. Phys. Chem. A* **2011**, *115*, 443-452.



### Water Disrupts Solvent-Induced Crystallization in Poly(L-lactide) to Yield Transparent Films



#### 2.1. Abstract

Water was found to disrupt the formation of spherulites, and thus affect the optical clarity of solvent-crystallized poly(L-lactide) (PLLA) films. This was investigated at multiple length scales using various microscopy techniques (polarized optical, electron, and atomic force), thermal analysis and small-, and wide-angle X-ray scattering. PLLA films crystallized in aqueous miscible organic solvents such as tetrahydrofuran (THF) and acetone, and their water mixtures were examined. PLLA films crystallized in THF and acetone had 40-80 μm spherulites and were optically opaque. When water was present in the solvent, the size decreased to 10-20 μm in THF and the films were translucent, and had completely different rod-like morphology in acetone, and the films were transparent. These differences in morphology and transparency were reflected in surface roughness as determined from AFM and SEM data. Lamellae became thicker upon heating these solvent-crystallized PLLA films as measured by small-

*angle X-ray scattering data. This was attributed to the crystallization of the amorphous chain segments as they diffuse to the crystal growth front of the existing lamellae and are adsorbed and recrystallized into the thicker crystals. These results suggest routes to control the morphologies of polymer films during solvent-induced crystallization and thus influence polymer properties such as optical clarity.*

## **2.2. Introduction**

Consumption and disposal of petroleum-based polymers have been a real concern nowadays due to their finite resources as well as in terms of the environmental pollution.<sup>1, 2</sup> In this regard, biobased polymers have drawn much attention since these can be used as an alternative to petroleum-based plastics. Poly(*L*-lactide) (PLLA), the most common stereoisomer of polylactide, is a widely used biobased polymer and it can be synthesized from renewable natural resources. It has diverse applications in biomedical fields such as bioimplants, surgical sutures, coronary stents, bone fixation devices, etc., and also as commodity plastics such as fibers and packaging films.<sup>3-7</sup> PLLA exists in different polymorphic forms depending on the processing conditions and a wide range of physical properties such as thermal, optical and mechanical properties are influenced by the polymorphic forms. Different polymorphic forms of PLLA are  $\alpha$ ,<sup>8-10</sup>  $\alpha'(\delta)$ ,<sup>11-15</sup>  $\alpha''$ ,<sup>16, 17</sup>  $\beta$ ,<sup>18-20</sup>  $\gamma$ ,<sup>21</sup> and  $\varepsilon$ .<sup>22-25</sup> Besides these, a mesophase of PLLA was also reported.<sup>26-29</sup>

Solvent-induced crystallization of polymers is an important subject from both scientific and technological perspectives. Solvents have frequently been encountered with polymers during polymerization and processing steps. Most of the advanced applications of polymers need advanced polymer processing techniques such as spin-casting, electrospinning, and wet spinning, where the solvent is one of the essential ingredients in processing the polymers. There have been significant efforts carried out to understand the solvent-induced crystallization of semicrystalline polymers.<sup>30-36</sup> Solvents can enhance the segmental mobility of polymer chains by lowering the glass transition temperature

( $T_g$ ) of the polymer to sub-ambient temperature, and as a result, the polymer chains can rearrange themselves to a low free energy state.<sup>34, 36</sup> Depending on the nature of the interaction between the polymer and solvent molecules, in some cases, the solvent molecules crystallize together with polymer chains to form the cocrystals.<sup>22, 30, 37, 38</sup> Extensive studies have been carried out to understand the solvent-induced crystallization behavior of polymers such as syndiotactic polystyrene,<sup>30, 33, 34, 36, 37</sup> poly(ethylene terephthalate),<sup>38</sup> poly(ethylene imine),<sup>35</sup> etc. PLLA is also known to be crystallized into different polymorphic forms in the presence of solvents. Recently, Marubayashi et al. found that the treatment of amorphous PLLA films with certain solvents such as N, N-dimethylformamide, cyclopentanone, tetrahydrofuran, etc. give cocrystals at subambient temperatures.<sup>22</sup> Pan et al. studied the solution crystallization of PLLA in chloroform and found that the PLLA crystallizes into the  $\alpha$  form.<sup>39</sup> Also, they have shown that the chloroform-crystallized PLLA is translucent (semitransparent) and its transparency changes with the annealing temperature. Marubayashi et al. investigated the crystal structure and morphology of PLLA treated under high-pressure CO<sub>2</sub> and showed that the PLLA crystallizes into the  $\alpha''$  form under 7–15 MPa CO<sub>2</sub> at 30 °C, whereas the  $\alpha$  crystals were obtained under 7–15 MPa CO<sub>2</sub> at 50–70 °C.<sup>17</sup> In addition, they demonstrated the formation of both rodlike superstructures on a nanometer scale and spherulites on a micrometer scale in the PLLA films crystallized under high pressure CO<sub>2</sub> at different conditions and correlated the superstructure formation with the transparency of crystallized PLLA. In this way, very few studies demonstrated that under specific conditions a transparent crystalline PLLA could be obtained by solvent-induced crystallization.

When it comes to the practical applications, the optical clarity of the polymer is an important factor for certain applications like packaging and coatings. In general, amorphous polymers are transparent and semicrystalline polymers are opaque in nature with few exemptions.<sup>40</sup> The transparent nature of amorphous polymers is due to the single refractive index of the amorphous phase.<sup>41</sup> The transparency in semicrystalline polymers depends on several factors. If the size of the spherulites formed during the crystallization is smaller than the wavelength of

the light, then the passage of light is not obstructed. On the other hand, if the crystallization resulted in the formation of larger spherulites, the light waves will be scattered. This results in the opaqueness of the material. The dimensions of the spherulites can be reduced by adding nucleating agents or clarifying agents. This reduction in the spherulite size is due to increase in the number of nucleating centers provided by the external additives.<sup>42</sup> The scattering of light can also be related to the different refractive indices of the crystalline and amorphous phases. Scattering of the light due to the surface roughness is considered as another major reason for the opaqueness of the polymer film. However, transparency can be improved by reducing the dimensions of the roughness (pores) below the wavelength of light. Even though most of the amorphous polymers are transparent, poor mechanical properties limit their applications. Therefore, it is necessary to improve the transparency of semicrystalline polymers, since it shows better mechanical properties. Solvent-induced crystallization of polymers is a relatively new method to control the superstructure of the polymers and hence the transparency.<sup>17, 39</sup>

Vyavahare et al. studied the crystallization behavior of poly(lactic acid) in water and demonstrated that water increases the rate of crystallization significantly.<sup>43</sup> It was established that the solvent molecules could promote the segmental mobility of polymer chains due to the disruption of the intermolecular interactions between polymer chains. The structural rearrangements in polymers are intimately related to the segmental mobility of polymer chains. In this chapter, we study the solvent-induced crystallization of PLLA under ambient conditions using aqueous miscible organic solvents such as acetone and THF, and their water mixtures. We investigated the morphologies at different length scales using wide-angle and small-angle X-ray scattering, atomic force microscopy, scanning electron microscopy and polarized light microscopy. In addition, we followed the structural reorganization upon heating of the solvent-crystallized PLLA. A simple model is proposed to explain the lamellar thickening during heating of the solvent-crystallized PLLA.

## 2.3. Experimental

**2.3.1. Materials:** PLLA, having  $M_w \sim 260000$ , and  $D \sim 1.5$  was purchased from Sigma-Aldrich. Acetone (purity  $\geq 99\%$ ) was supplied by SD Fine Chemicals Limited. THF (purity  $\sim 99.9\%$ ) was purchased from Merck. The solvents were used as received.

**2.3.2. Sample Preparation:** Amorphous films were prepared by melting PLLA pellets by keeping it  $\sim 200$  °C, followed by sudden quenching in liquid nitrogen. Such obtained films were directly dipped in various organic solvents such as acetone, THF, acetone/water, and THF/water mixtures for three days. In acetone/water mixture and THF/water mixture, the volume percentages of the solvents were maintained as 50/50 (v/v).

### 2.3.3. Characterization

**X-ray Measurements:** Wide- and small-angle X-ray scattering (WAXS/SAXS) measurements were performed using XEUSS SAXS/WAXS system from Xenocs (Operating voltage: 50 kV and current: 0.60 mA). Source of X-ray was Cu  $K\alpha$  radiation with wavelength,  $\lambda = 1.54$  Å. The measurements were taken in the transmission mode geometry. The 2D images were recorded on a Mar 345 detector (Image plate), and such obtained images were azimuthally averaged using the Fit2D software. Silver behenate and silicon powder were used to calibrate the sample to detector distance for SAXS and WAXS, respectively. The detector was set at 1050 mm and 221.75 mm from the sample in the direction of the beam for SAXS and WAXS data collections, respectively. XEUSS SAXS/WAXS system is equipped with a Linkam THMS 600 hot stage. The peak fitting of the WAXS patterns was performed by using the GRAMS 32 software. The thickness of the films used for the X-ray measurements was  $\sim 1$  mm.

**SAXS Data Analysis:** The 2D SAXS images were azimuthally averaged to obtain 1D scattering intensity profiles as a function of  $q$  ( $q = (4\pi \sin \theta)/\lambda$ ), where  $\theta$  is the scattering angle and  $\lambda$  is the wavelength of X-ray radiation). The resulting scattering intensity SAXS profiles were corrected for background scattering. One-

dimensional electron density correlation function ( $K(z)$ ) was calculated from the SAXS data to determine the lamellar parameters.  $K(z)$  for stacked lamellar structure is defined as follows.<sup>44</sup>

$$K(z) = \int_0^\infty q^2 I(q) \cos(qz) dq \quad (1)$$

Where  $z$  is the direction along which the electron density is measured and,  $I(q)$  is the scattered intensity. The various lamellar structural parameters such as long period ( $L$ ), lamellar thickness ( $l_c$ ) and amorphous thickness ( $l_a$ ) were calculated from the  $K(z)$  curve as shown in Figure 2.1.

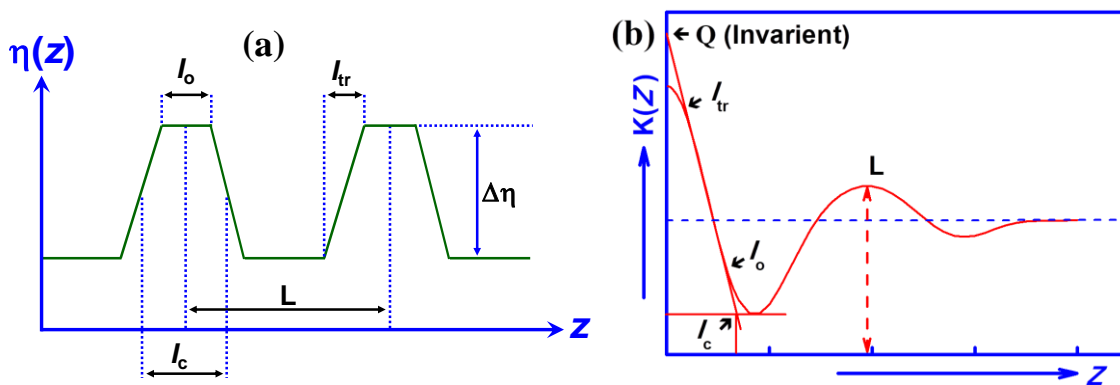


**Figure 2.1.** Electron density distribution  $\eta(z)$  and the one-dimensional electron density correlation function  $K(z)$  for the lamellar system.  $L$  is the long period and  $l_a$  is the amorphous thickness. The mean lamellar thickness ( $l_c$ ) is obtained by subtracting  $l_a$  from the  $L$  ( $l_c = L - l_a$ ).

**Differential Scanning Calorimetry (DSC):** DSC measurements were carried out using TA Instruments DSC Q2000 model equipped with a refrigerated cooling system. The solvent-crystallized samples were heated from 0 to 200 °C at a heating rate of 10 °C/min, under the nitrogen atmosphere.

**Thermogravimetric Analysis (TGA):** The solvent content in the PLLA films (thickness  $\sim 1$  mm) treated with various solvents was measured using TA Instruments TGA Q50. The measurements were carried out under nitrogen atmosphere, at a heating rate of 10 °C/min.

**UV-vis Spectroscopy Measurements:** The optical transmittance of the films (thickness  $\sim 500 \mu\text{m}$ ) was measured using Shimadzu UV-vis spectrophotometer (UV-2600). The films were attached on a quartz plate and the percentage of transmittance was measured as a function of wavelength.

**Polarized Optical Microscopy (POM) Measurements:** Spherulitic morphology of the samples (thickness  $\sim 100 \mu\text{m}$ ) was analyzed using Leica DFC 490 polarized light optical microscope, equipped with Mettler Toledo FP82HT Hot Stage. For the temperature-dependent measurements, the sample was heated from  $30 \text{ }^\circ\text{C}$  to  $180 \text{ }^\circ\text{C}$  at a rate of  $10 \text{ }^\circ\text{C}/\text{min}$  and the images were captured at every  $10 \text{ }^\circ\text{C}$  interval.

**Atomic Force Microscopy (AFM) Measurements:** Surface morphology of solvent-crystallized PLLA films was probed using Bruker Multimode AFM-3COCF in the tapping-mode at room temperature. Antimony doped Silicon cantilever tips with a resonance frequency of  $300 \text{ kHz}$  and a spring constant of  $40 \text{ N/m}$  were used. Films (thickness  $\sim 200 \mu\text{m}$ ) pasted on a silicon wafer substrate were used for the imaging.

**Scanning Electron Microscopy (SEM) Measurements:** SEM analyses were performed using Zeiss EVO 18 cryo scanning electron microscope. The film (thickness  $\sim 1 \text{ mm}$ ) was directly pasted onto a stub using a double face adhesive tape and subjected to a thin gold coating before the analysis. The measurements were carried out at an accelerating voltage of  $20 \text{ kV}$ .

**Dynamic Mechanical Analysis (DMA):** Amorphous samples for the DMA measurements were prepared by melting the PLLA pellets by keeping in between two aluminium plates at  $\sim 200 \text{ }^\circ\text{C}$ , followed by sudden quenching in liquid nitrogen. These samples were dipped in various solvents for three days. The measurements were performed in the tension mode at a frequency of  $1 \text{ Hz}$  with amplitude of  $5 \mu\text{m}$ . The samples, having the dimension  $35 \times 4 \times 1 \text{ mm}^3$ , were heated from room temperature to  $150 \text{ }^\circ\text{C}$  at a heating rate of  $2 \text{ }^\circ\text{C}/\text{min}$ .

## 2.4. Results and Discussion

### 2.4.1. Solvent-Induced Crystallization of Amorphous PLLA in Various Solvents

Crystallization of amorphous PLLA films was induced by direct immersion of films into various solvents at  $30 \text{ }^\circ\text{C}$  for three days. Figure 2.2a shows the WAXS patterns of solvent-crystallized PLLA samples in acetone, THF,

acetone/water mixture (50/50 v/v) and THF/water mixture (50/50 v/v) at room temperature. Irrespective of the solvent used for the crystallization, well-defined X-ray reflections appeared at  $2\theta = 12.5^\circ$ ,  $14.8^\circ$ ,  $16.8^\circ$ ,  $19.1^\circ$ , and  $22.5^\circ$ , which were assigned to the  $\alpha$  form.<sup>8</sup> The absence of the characteristic reflection of  $\alpha'$ ( $\delta$ ) form at  $2\theta = 24.6^\circ$ , indicates that the amorphous PLLA crystallized exclusively into the  $\alpha$  form in the presence of solvents.<sup>12, 13, 15</sup>

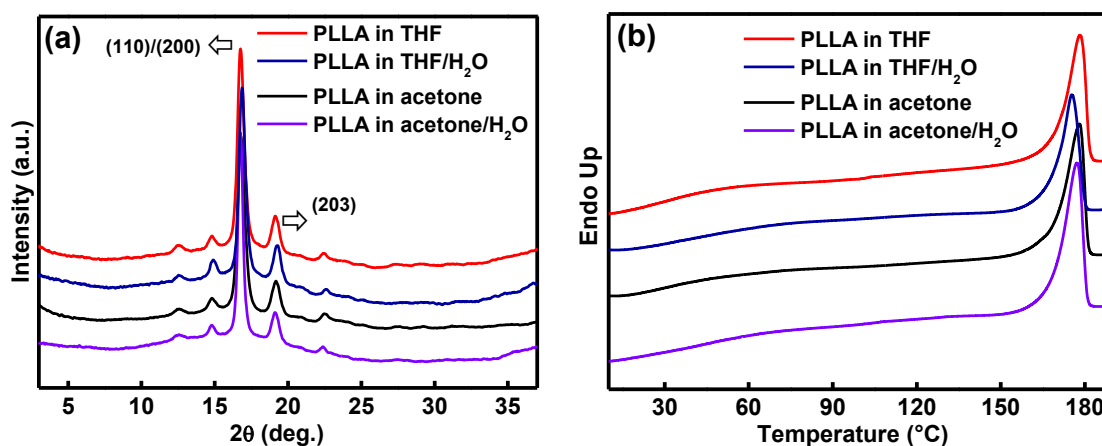


**Figure 2.2.** (a) WAXS patterns and (b) DSC thermograms obtained for PLLA films crystallized in various solvents at 30 °C for three days. DSC thermograms are taken in the heating process.

Figure 2.2b shows the DSC thermograms of solvent-crystallized PLLA samples in various solvents. DSC thermograms show an endotherm at  $\sim 177^\circ\text{C}$  corresponding to the melting of the  $\alpha$  form of PLLA. It is worth mentioning here that no transitions corresponding to the  $\alpha'$ ( $\delta$ )-to- $\alpha$  or  $\varepsilon$ -to- $\alpha$  were detected in the DSC thermograms indicating that all the solvent-crystallized samples were directly crystallized into the  $\alpha$  form. Marubayashi et al. reported that the PLLA crystallizes into the  $\varepsilon$  form (cocrystal) in THF at  $-25^\circ\text{C}$ .<sup>22</sup> However, in the present study, the PLLA crystallized into the  $\alpha$  form at  $30^\circ\text{C}$  as confirmed by the WAXS and DSC results. In addition to the melting peak, broad endotherms were observed in each thermogram in the temperature range of 30–120 °C.

TGA measurements (Figure 2.3) were carried out to understand the amount of residual solvents present in the crystallized samples. It is evident from the TGA thermograms that around 8, 10, 13, and 15 wt% of residual solvents were present in acetone, acetone/water, THF and THF/water crystallized PLLA samples,

respectively. Unlike the cocrystals, in the  $\alpha$  form, the residual solvents mainly reside in the amorphous phase. These results are also consistent with the observations made by Pan et al. where the chloroform-crystallized PLLA showed  $\sim 8.5$  wt% residual solvent.<sup>39</sup>

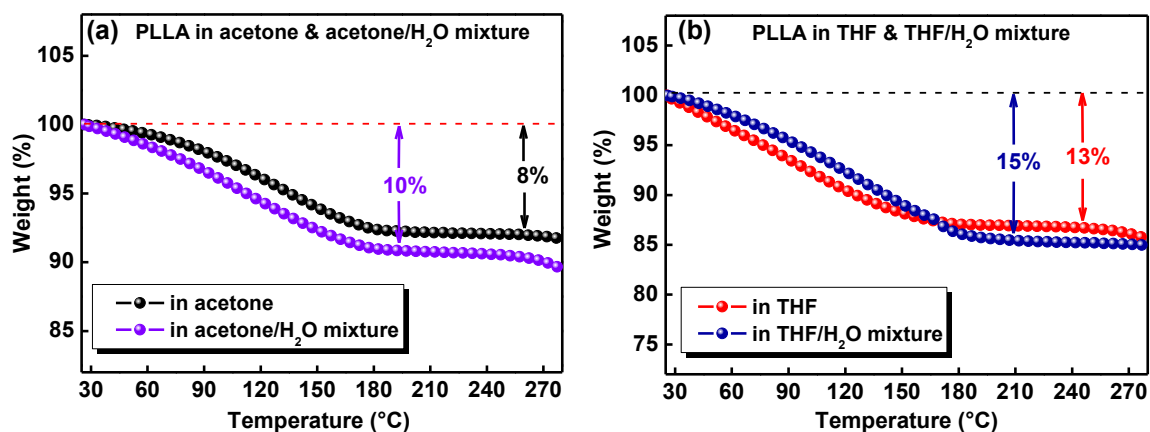


**Figure 2.3.** TGA thermograms obtained for PLLA films crystallized in (a) acetone and acetone/water mixture and (b) THF and THF/water mixture.

Another noteworthy observation from the TGA data is that the samples crystallized in acetone/water mixture and THF/water mixture showed  $\sim 2$  wt% more residual solvent compared to that of the samples crystallized in acetone and THF and it might be due to the presence of  $\sim 2$  wt% of excess water molecules in the amorphous phase of PLLA. Vyavahare et al. showed that the equilibrium water uptake in PLLA was low in the solid state ( $\sim 1$  wt%).<sup>43</sup> Compared to the organic solvents, water uptake in PLLA is very low because of its hydrophobic nature. Based on the TGA results, broad endotherms observed in DSC thermograms in the temperature range of 30–120 °C can be assigned to the evaporation of residual solvents from the amorphous phase of PLLA.

#### 2.4.2. Morphology of Solvent-Crystallized PLLA Films

Figure 2.4 shows the POM images of PLLA thin films crystallized in THF, acetone, THF/water mixture, and acetone/water mixture. PLLA film crystallized in THF shows spherical particles (spherulites) with the diameter between 40 and 80  $\mu\text{m}$  (Figure 2.4a). Unlike the melt-crystallized spherulites, irregular growth of the highly disordered spherulitic crystallites was observed. Acetone-crystallized PLLA

films also showed similar morphology (Figure 2.4b). Pan et al. observed similar kind of spherulitic patterns in chloroform-crystallized PLLA films.<sup>39</sup> PLLA films crystallized in THF/water mixture showed spherulites (Figure 2.4c) in the size range of  $\sim 10\text{--}20\ \mu\text{m}$ . On the other hand, PLLA films crystallized in acetone/water mixture showed uniformly sized tiny crystallites (Figure 2.4b) probably in the nanometer size range.

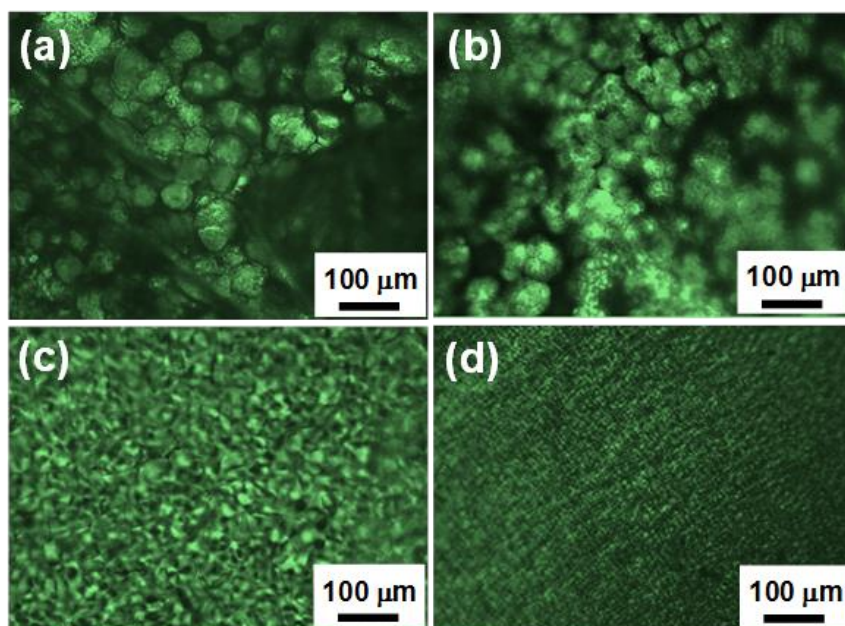


**Figure 2.4.** POM images obtained at room temperature of PLLA films crystallized in (a) THF, (b) acetone, (c) THF/water mixture, and (d) acetone/water mixture.

However, it is difficult to identify the boundaries and hence the spherulite sizes from the POM images. To gain more insight about the morphologies and their sizes, AFM measurements were carried out on the thin films of PLLA crystallized in various solvents.

The AFM images of PLLA films crystallized in acetone and acetone/water mixture were shown in Figure 2.5. In agreement with the POM results, PLLA film crystallized in acetone showed larger spherical particles ( $\sim 30\ \mu\text{m}$ ) with very high surface roughness. Porosity and surface roughness of the acetone-crystallized samples will be discussed in the later section with the help of SEM images. On the other hand, the PLLA film crystallized in acetone/water mixture showed a unique morphology with nanosized cavities all over the surface. We are speculating here

that the nanosized cavities might be formed due to the gradual evaporation and desorption of solvent molecules upon drying of the swollen PLLA film. AFM image revealed that the crystalline lamellae were grown from the surface of the cavities. The magnified AFM image of Figure 2.5(b) clearly showed the formation of rodlike lamellar morphology. This kind of morphology was reported in solution-crystallized polymers. For example, Xue et al. reported the rodlike lamellar morphology in solution-cast films of ultrahigh molecular weight polyethylene (UHMWPE).<sup>45</sup> Marubayashi et al. reported the formation of rodlike lamellar morphology in PLLA thin films crystallized under high-pressure CO<sub>2</sub> at appropriate conditions.<sup>17</sup>

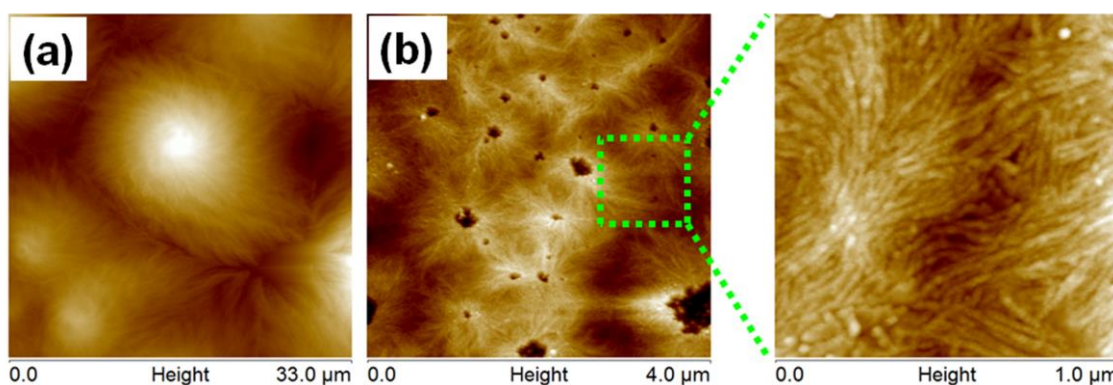


**Figure 2.5.** AFM height images of PLLA films crystallized in (a) acetone, (b) acetone/water mixture.

However, the morphology observed for the PLLA film crystallized in THF/water mixture is different from that of the film crystallized in acetone/water mixture. Figure 2.6 shows the AFM image of PLLA film crystallized in THF/water mixture. In this case, in agreement with the POM results, spherulitic morphology was observed with an average diameter of 10  $\mu\text{m}$ . Here also nanosized cavities are observed. However, these cavities are formed within the spherulitic structures. These results clearly showed that the solvents used for the crystallization have a strong effect on the crystallization rate and the morphology of PLLA. Naga et al. investigated the crystallization of PLA in various organic solvents including acetone, THF, etc. and found that acetone was the effective solvent for expediting the crystallization of PLA.<sup>31</sup> Recently, Wu et al. studied the crystallization behavior of PLLA ultrathin films induced by dichloromethane, acetone, and

chloroform, and found that the solvent-specific competition between solvent-induced crystallization and dissolution effects play an important role in determining the crystallization rate and morphology of PLLA.<sup>32</sup> They found that acetone-annealed PLLA ultrathin films (ca. 80 nm) showed spherulitic morphology (5–10  $\mu\text{m}$  in diameter) and the spherulite sizes remain unchanged with prolonged annealing in acetone vapors.

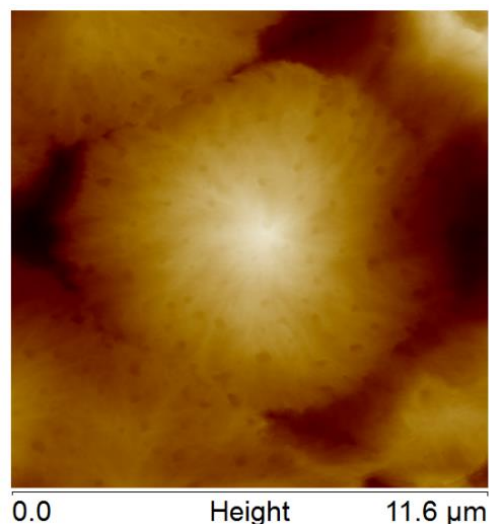


**Figure 2.6.** AFM height image of PLLA film crystallized in THF/water mixture.

It is well-known that the polymer-solvent interactions affect the solvent-induced crystallization of the polymer. However, because of the difficulties in examining the structural changes of polymers during the solvent-induced crystallization, a limited number of studies are available in understanding the structural characteristics of solution-crystallized polymers. Tashiro and co-workers investigated the solvent-induced crystallization of syndiotactic polystyrene (sPS) and demonstrated that the accelerating rate of molecular motion of the amorphous chain and the formation rate of crystalline domains were found to be dependent on the nature of the solvent used for the crystallization of the polymer.<sup>34, 36</sup> They also measured the  $T_g$  of sPS in different solvent environments using both FTIR and molecular dynamics calculations and showed that the  $T_g$  was shifted to subambient temperatures (–80 to –20 °C) depending on the solvent used for the swelling experiments.<sup>36</sup> Such experiments are difficult to conduct with high boiling solvents.

In the present study, we used the mixture of solvents for the crystallization of PLLA. In order to understand the origin of the formation of different morphologies in different solvent environments and polymer-solvent interactions, we attempted to measure the  $T_g$  of PLLA crystallized in various solvents. DSC thermograms depicted in Figure 2.2b did not show the  $T_g$  of PLLA due to its crystalline nature. The  $T_g$  of PLLA films crystallized in various solvents was measured by dynamic mechanical analysis (DMA). Figure 2.7 shows the temperature-dependent loss tangent ( $\tan \delta$ ) of amorphous PLLA and PLLA films crystallized in various solvents.

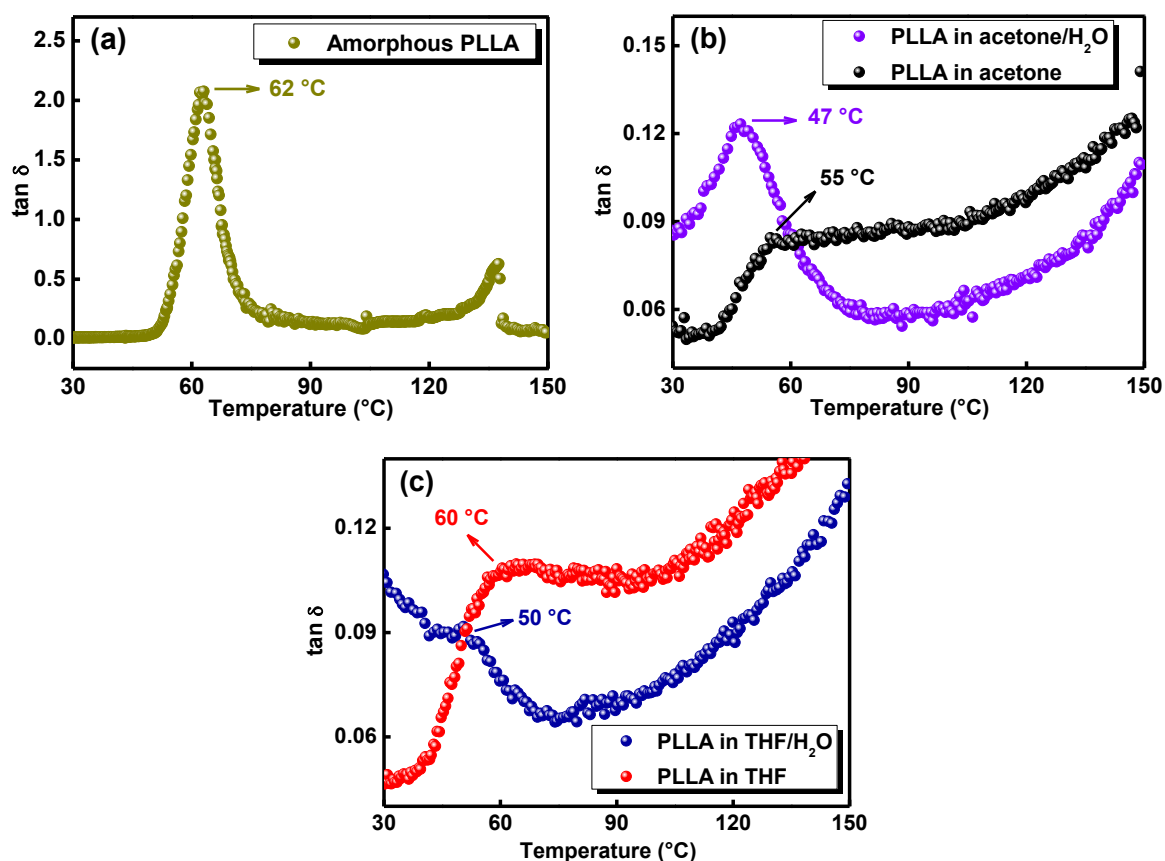


**Figure 2.7.** Temperature-dependent  $\tan \delta$  curves measured in the heating process for (a) amorphous PLLA, (b) PLLA films crystallized in acetone and acetone/water mixture, and (c) THF and THF/water mixture.

The  $T_g$  observed in the  $\tan \delta$  curve for the amorphous PLLA is  $\sim 62$  °C (Figure 2.7a), which is in good agreement with the  $T_g$  measured by DSC. As seen in Figure 2.7, the  $T_g$  of the solvent-crystallized PLLA is different and it is lower than that of the amorphous PLLA. The reduction of the  $T_g$  of solvent-crystallized

PLLA films is due to the plasticization effect of the residual solvent remaining in the polymer matrix. PLLA crystallized in acetone/water mixture showed lowest  $T_g$  ( $\sim 47$  °C) among the solvents used for the crystallization of PLLA. On the other hand, PLLA sample crystallized in THF showed higher  $T_g$  ( $\sim 60$  °C), which is almost similar to the amorphous PLLA, even though the amount of residual solvent estimated for this sample  $\sim 13$  wt% (Figure 2.3). Pan et al. reported that the  $T_g$  of chloroform-crystallized PLLA is around 35 °C, which is having residual solvent  $\sim 8.5$  wt% similar to the acetone-crystallized PLLA.<sup>39</sup> Based on the literature and the results of the present study, we may say that the strength of the interaction between the polymer and solvent is dependent on the type of solvent used for the crystallization. These results are very helpful to explain the morphologies formed in different solvent environments.

PLLA films immersed in acetone/water mixture have high enough mobility and upon solvent evaporation, a large number of crystal nuclei can be formed because of the high degree of supercooling ( $T_m - T_c$ ). It has been showed that the crystal growth rate  $G$  is diffusion-controlled and linearly proportional to supercooling  $\Delta T$  in solution-grown crystals.<sup>46</sup> Additionally, the evaporation rate of acetone/water mixture from the PLLA matrix also has a strong influence on the crystal nuclei formation and its growth. It was observed that the evaporation of the solvent from the PLLA matrix is very slow in the case of water mixtures compared to the individual organic solvent and this might influence the degree of supercooling ( $T_m - T_c$ ). These results clearly indicate that polymer-solvent interaction, solvent evaporation rate, and film shrinking upon the removal of the solvent from the thin films are responsible for the formation of rodlike lamellar morphology in the case of PLLA film crystallized in acetone/water mixture. On the other hand, in the case of acetone and THF crystallized films, the solvent evaporation rate is quite rapid and the shrinkage of the film is fast, as a result, the larger spherulites are formed because of the low degree of supercooling.

To further understand the surface morphology and surface roughness of PLLA films crystallized in various solvents, the SEM images are taken. In agreement with the POM and AFM results, spherical aggregates of PLLA are

observed in the case of PLLA films crystallized in acetone and THF (Figures 2.8a and 2.8b). These spheres are similar to the polyethylene “globs” observed by quenching the polyethylene solutions in xylene.<sup>47</sup> Such kind of globs were reported in solution-crystallized samples and these globs are formed due to the precipitation/phase separation process occurred during the solidification process. The crystalline lamellae are packed in each sphere, which is evident from the strong appearance of birefringence in POM images (Figures 2.4a and 2.4b). High porosity was also observed in these samples with high surface roughness. On the other hand, no such structure was observed in the case of PLLA films crystallized in acetone/water mixture and THF/water mixture with negligible surface roughness. Little roughness was observed in the films crystallized in THF/water mixture.

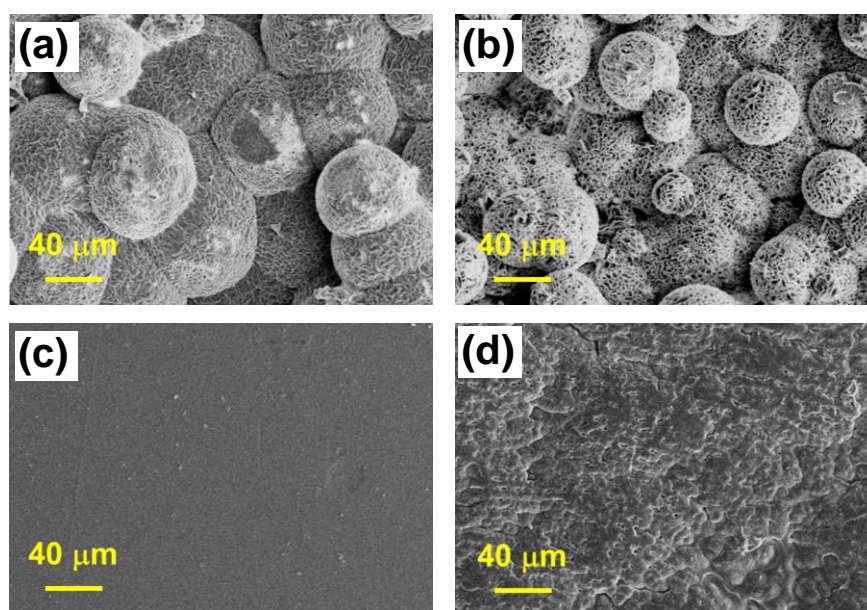


**Figure 2.8.** SEM images of PLLA films crystallized in (a) acetone, (b) THF, (c) acetone/water mixture, and (d) THF/water mixture.

### 2.4.3. Transparency of Solvent-Crystallized PLLA Films

Figure 2.9 shows the photographs of PLLA films crystallized in various solvents along with the melt-quenched amorphous PLLA. As seen, the melt-quenched PLLA is transparent because of its amorphous nature. The films crystallized in organic solvents (acetone and THF) appeared completely opaque.

On the other hand, the films crystallized in the mixture of solvents (acetone/water and THF/water) are translucent. Further, the transparency of PLLA film is varied with the nature of the solvent used for the crystallization of PLLA in solvent/water mixture. The transparency of the PLLA film crystallized in acetone/water mixture is almost comparable with the melt-quenched amorphous PLLA. Conversely, the PLLA film crystallized in THF/water mixture is more translucent compared to the film crystallized in acetone/water mixture.



**Figure 2.9.** Photographs showing the transparency of PLLA films crystallized in various solvents. For the purpose of comparison, photograph of amorphous PLLA is also shown.

To quantify the transparency of the samples, the percentage of transmittance was measured using UV-vis spectrophotometer, as a function of wavelength. Figure 2.10 is the UV-visible transmittance spectra obtained in the visible region (400–700 nm) for the melt-quenched amorphous PLLA and PLLA crystallized in various solvents. The melt-quenched amorphous film and the PLLA film crystallized in acetone/water mixture display almost the same transmittance. A slight decrease in the transmittance was observed in the PLLA film crystallized in THF/water mixture. On the other hand, in agreement with the photographs shown in Figure 2.9, acetone and THF crystallized films showed lower transmittance values. As discussed in the preceding section, it is obvious that the change in the transparency of crystalline PLLA films is a result of the changes in the crystalline morphology of PLLA films that takes place during the crystallization process in various solvents. PLLA films crystallized in acetone/water mixture possess rodlike lamellar morphology in the nanometer length scales and sizes of the cavities formed were below the wavelength of the light. As a result, no scattering is observed in these films, and these samples appeared almost transparent equivalent to that of the amorphous film. Marubayashi

et al. reported the formation of crystalline and transparent PLLA films showing the similar kind of morphology after the treatment with high-pressure CO<sub>2</sub>. On the other hand, PLLA films crystallized in THF/water mixture are translucent because of the presence of smaller sized spherulites with relatively smooth surface. However, the films crystallized in acetone and THF are completely opaque because of the formation of larger spherical particles with high surface roughness and porosity. In this way, we have clearly demonstrated the intimate relation between the morphology of the PLLA films with their transparency.

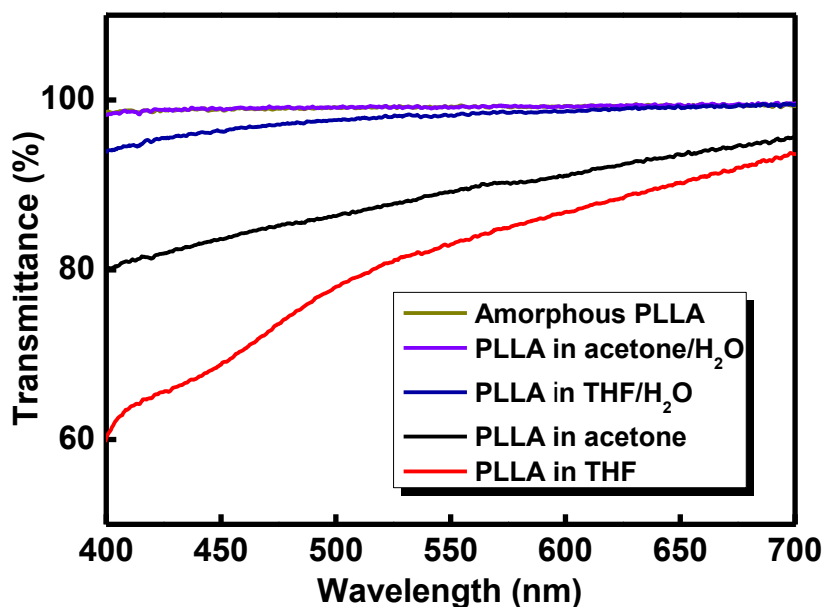


**Figure 2.10.** Transmittance measured using ultraviolet–visible (UV-vis) spectrophotometer, for PLLA films crystallized in various solvents. For the purpose of comparison, UV-vis spectrum of amorphous PLLA is also shown.

#### 2.4.4. Structural Reorganization of Solvent-Crystallized PLLA Films during Heating

Since the maximum transparency was observed for the acetone/water treated film, this sample was further used for detailed studies. The variation in the transparency of the PLLA film crystallized in acetone/water mixture was analyzed at different temperatures using POM, AFM, and SAXS. Figure 2.11 shows the POM images of PLLA films crystallized in acetone/water mixture at different temperatures. The photographs of the PLLA films annealed at different temperatures are shown in the inset of Figure 2.11. As seen in the POM images, no

significant differences were observed in the size of the spherulites at different temperatures, however, a slight variation in the transparency is seen in the pictures at higher temperatures, above the  $T_g$  of PLLA.



**Figure 2.11.** POM images of PLLA films crystallized in acetone/water mixture measured at (a) 30 °C, (b) 100 °C, and (c) 160 °C. Photographs showing the transparency of PLLA films at different temperatures are shown in the inset.

In order to probe the changes happening in the nanometer length scales, the AFM analysis of PLLA films crystallized in acetone/water mixture at different temperatures were carried out and the images are shown in Figure 2.12. As discussed in the preceding section, PLLA film crystallized in acetone/water mixture shows rodlike morphology with the regular stacking of lamellae at room temperature (Figure 2.12a). The bright regions in the AFM image are crystalline lamellae, whereas the dark regions are corresponding to the amorphous part. The average lamellar thickness observed is of the order of 20 nm, which is higher than the average lamellar thickness evaluated from the SAXS data as mentioned later. This discrepancy can be attributed to the AFM tip surface convolution effects.<sup>48</sup> In this study, the values reported for the lamellar thickness from the AFM images are not corrected for tip convolution effects since the precise nano-tip shape and its size are unknown. When the film is heated to a temperature  $\sim 160$  °C, the rodlike morphology of the sample remains intact, but a significant increase in lamellar thickness is observed in the AFM image (Figure 2.12b). The average lamellar thickness measured at 160 °C ( $\sim 40$  nm) is significantly higher than the thickness measured at room temperature.

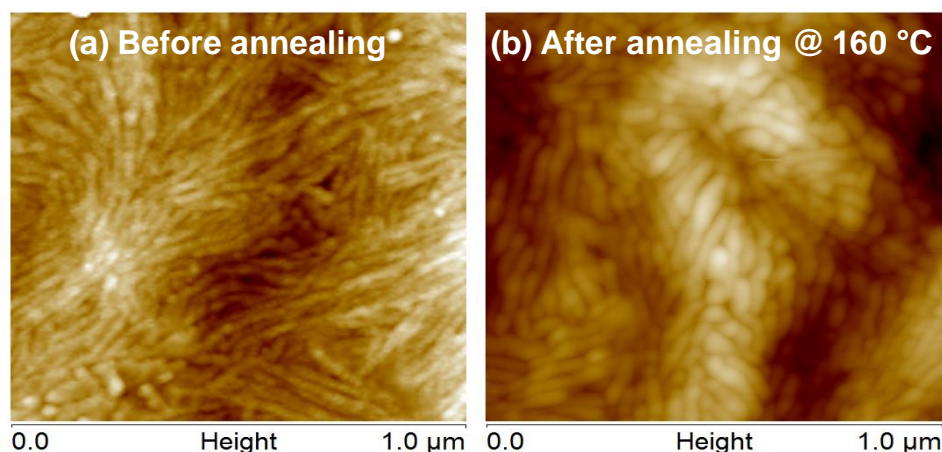


**Figure 2.12.** AFM height images of PLLA films crystallized in acetone/water mixture measured at (a) 30 °C (before annealing) and, (b) after annealing at 160 °C.

It is known that the polymer chains fold to form lamellae during the crystallization process. In solution-crystallized samples, the folded polymer chains are kinetically trapped and acquire a compact nonequilibrium conformation. In this state, the structure will be away from the equilibrium state, and it shows high free energy due to the presence of folded chains, but with the minimum stable thermodynamic value. Hence on heating, the lamellae show a tendency to thicken at high temperatures, to reduce their free energy. In the present study, similar to the solution-crystallized PE, the polymer chains in PLLA samples crystallized in acetone/water mixture adopt a nonequilibrium state, and upon heating, the structural reorganization occurs by lamellar thickening to reach the equilibrium state. Two major mechanisms have been proposed to explain the lamellar thickening phenomena in semicrystalline polymers: One is the sliding diffusion mechanism in which the lamellar thickening occurs via a mutual chain rearrangement along the chain axis between the adjacent lamellae,<sup>45, 49, 50</sup> and the other one is the lamellar thickening via the melt-recrystallization process.<sup>51, 52</sup> However, by the *ex-situ* annealing experiments, it is rather difficult to understand the mechanism of lamellar thickening. Further *in-situ* experiments were conducted to understand the lamellar thickening in solvent-crystallized PLLA by using temperature-dependent SAXS.

Figure 2.13a shows the Lorentz-corrected SAXS patterns collected during the heating of PLLA films crystallized in acetone/water mixture. A broad

scattering peak was observed at 30 °C with a maximum at  $q \sim 0.36 \text{ nm}^{-1}$  ( $L = 17.3 \text{ nm}$ ), and this value is smaller than that of the melt-crystallized  $\alpha$  form ( $L = 24 \text{ nm}$ ) (data not shown here). Welch and Muthukumar showed that the initial lamellar thickness in solution-crystallized polymers is dictated by entropic barriers and the growth at the crystalline interface is happened by simultaneous chain adsorption and crystallographic registry.<sup>46</sup> Upon heating, no major changes were observed in the SAXS patterns up to 140 °C. On further heating, the peak shifted to lower  $q$  and became sharper with increasing intensity. The lamellar structure parameters were estimated from the SAXS data by calculating the 1D electron density correlation function ( $K(z)$ ) curves at various temperatures in the heating process.

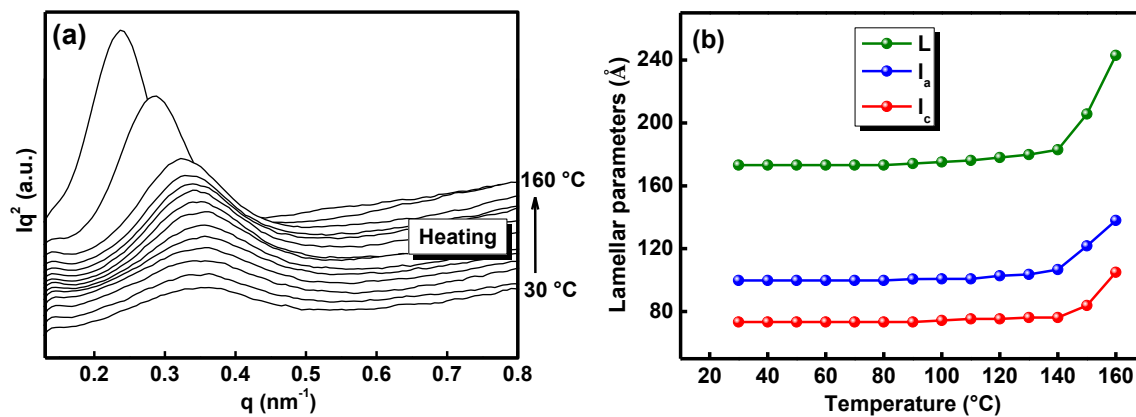


**Figure 2.13.** Temperature dependence of (a) SAXS patterns (Lorentz-corrected) and (b) long period ( $L$ ), lamellar thickness ( $l_c$ ), and amorphous thickness ( $l_a$ ) obtained for PLLA film crystallized in acetone/water mixture upon heating.

Figure 2.14 shows the representative  $K(z)$  curves calculated at 30 and 160 °C. The lamellar structure parameters such as long period ( $L$ ), lamellar thickness ( $l_c$ ) and amorphous thickness ( $l_a$ ) are plotted as a function of temperature in Figure 2.13b.  $L$  and  $l_c$  increased rapidly above 150 °C, suggesting that the crystalline lamellae undergo major structural reorganization above 150 °C.  $L$  and  $l_c$  values are increased by  $\sim 7 \text{ nm}$  and  $\sim 3 \text{ nm}$ , respectively. On the other hand, the increase in the amorphous thickness was  $\sim 4 \text{ nm}$ . Thus the increase in the long period value can be related to the lamellar thickening upon heating. These observations are in good agreement with the AFM results as discussed in the preceding section albeit the lamellar thickness was more due to the tip deconvolution effect. Such lamellar

thickening in semicrystalline polymers during heating has been reported in the literature both in solution and melt crystallized samples such as PE, nylon 6,6, poly(ethylene terephthalate) and poly(butylene terephthalate).<sup>45, 49, 53-56</sup>

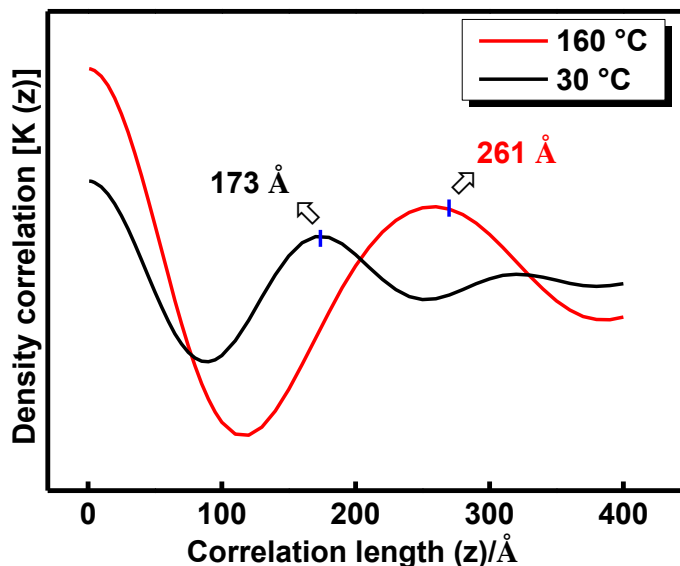


**Figure 2.14.** 1D electron density correlation function calculated based on the SAXS data collected at 30 and 160 °C for the PLLA film crystallized in acetone/water mixture.

Rastogi et al. observed lamellar doubling in solution-crystallized UHMWPE where the lamellar thickening occurred via mutual chain arrangement between the adjacent lamellae along the chain axis.<sup>45, 49</sup> During the lamellar doubling process, the intensity of the SAXS peak decreased significantly, and the peak broadening happened suggesting the loss of long range order. Similar to the present study, Murthy et al. reported the lamellar thickening in nylon 6,6 at the higher temperature, where the SAXS peak became sharp and the intensity of the peak increased above the Brill transition temperature.<sup>54</sup> The increased intensity was assigned to the changes in the density of the interlamellar amorphous phase rather than the increase in the volume fraction of the crystalline lamellae. This conclusion was drawn based on the decrease in the degree of crystallinity during the Brill transition.

Temperature-dependent WAXS measurements were carried out to understand the changes in the degree of crystallinity and the crystal structure of PLLA film crystallized in acetone/water mixture during heating as shown in

Figure 2.15a. As already discussed, the PLLA film treated with acetone/water mixture was crystallized into the  $\alpha$  form. On heating, there was no change in the crystal structure and the  $\alpha$  structural form remained unchanged up to the melting. However, the half-width and peak intensity of all the diffraction peaks were significantly changed upon heating at around 140 °C. By using the curve-fitting software, the peak intensity and half-width of (110/200) reflection were carefully estimated and are plotted against temperature as shown in Figure 2.15b. A significant increase in the peak intensity was observed above 140 °C, and at the same time, the half-width of the peak reduced significantly at the same temperature. The decrease in the half-width of the crystalline reflection (110/200) suggests that the lateral crystal size along a/b axis increased significantly. These changes confirmed the structural regularization of the crystalline lamellae at the higher temperature.

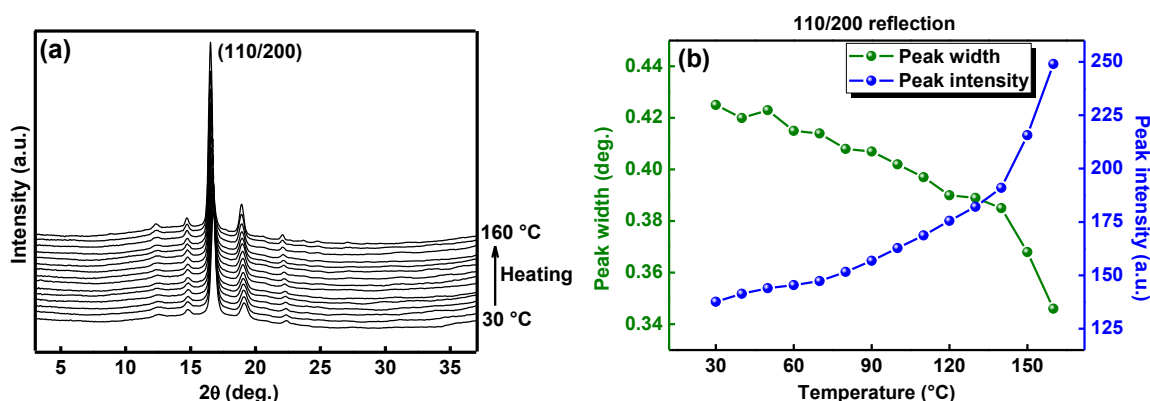


**Figure 2.15.** Temperature-dependent (a) WAXS patterns and (b) peak-width and intensity (110/200) of PLLA film crystallized in acetone/water mixture collected upon heating.

Temperature dependent POM, WAXS and SAXS measurements offer no evidence of melting of crystals during the lamellar thickening process. Therefore, we ruled out the possibility of melt-recrystallization mechanism. In the sliding diffusion mechanism, it has been reported that the thickness of the resultant lamellae is doubled.<sup>45, 49</sup> Since the lamellar doubling was not observed in the *in-situ* SAXS experiments, the possibility of sliding diffusion mechanism can be also eliminated. On the basis of molecular modelling, Welch and Muthukumar proposed that the enhanced mobility of the chain segments gives rise to a highly cooperative process in solution-crystallized polymers to bring about a

rearrangement of the growth front to form stems at the crystal growth front and increase lamellar thickness.<sup>46</sup> In PLLA, the residual solvent molecules reside in the amorphous phase of the  $\alpha$  form (see Figure 2.3) and the activated mobility of PLLA chains at high temperature solution-crystallized polymer may promote this chain diffusion, and the crystallization of the amorphous phase into the stable  $\alpha$  form. At a higher temperature, above 140 °C, amorphous chains diffuse to the crystal growth front and finally adsorbed and crystallized into the thicker crystals. Lamellar thickening happens both in lateral direction and chain axis direction as confirmed by the decrease in the half-width of the WAXS reflections and  $q$  value in the SAXS pattern at a higher temperature.

The invariant  $Q$ , which represents the total integrated scattering of the SAXS, is the difference in the electron density between the crystalline and amorphous regions also changed drastically above 140 °C (Figure 2.16). By combining the SAXS and WAXS data, we speculate here that the volume fraction of the crystallites increases significantly at higher temperature due to the crystallization of the amorphous phase.

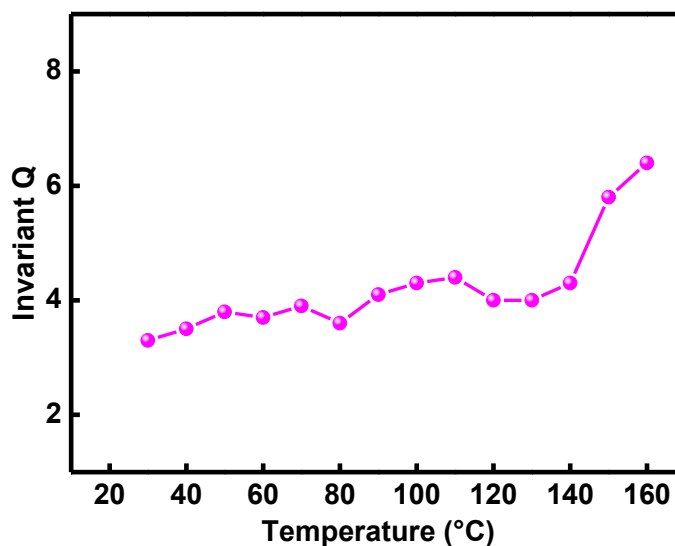


**Figure 2.16.** Changes in SAXS invariant ( $Q$ ) obtained for PLLA film crystallized in acetone/water mixture upon heating.

Based on the results obtained in the present study, a schematic model is proposed to explain the lamellar thickening of the solvent-treated PLLA at a higher temperature as shown in Figure 2.17.

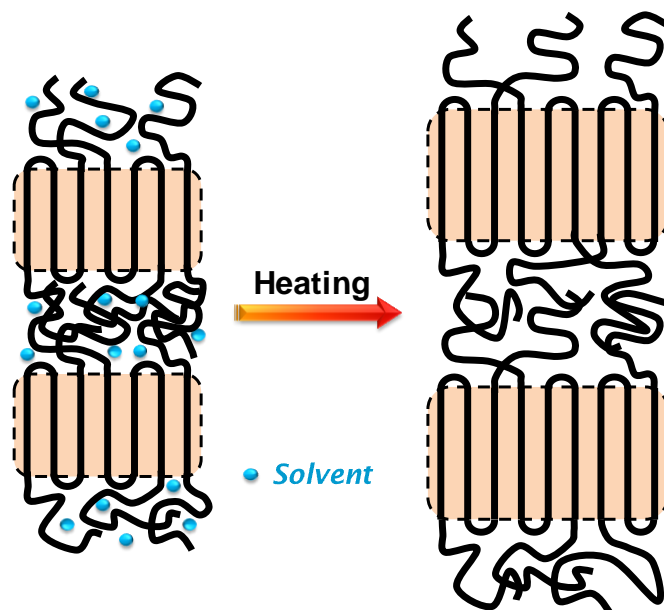


**Figure 2.17:** Schematic model for explaining the lamellar thickening process in solvent-treated PLLA at higher temperatures.

The initial lamellar thickness of the PLLA crystallized in acetone/water mixture is dictated by free energy barriers, and it is smaller than the lamellar thickness of the melt-crystallized PLLA. Upon heating, no major change in the thickness of the lamellae was observed up to 140 °C. At a higher temperature, above 140 °C, amorphous chains diffuse to the crystal growth front and finally adsorbed and recrystallized into the thicker crystals. The residual solvent, which is residing in the amorphous phase of the solution-crystallized polymer, may also play an important role in the chain diffusion at a higher temperature.

## 2.5. Conclusions

We investigated the solvent-induced crystallization of PLLA using aqueous miscible organic solvents such as acetone and THF, and their water mixtures at ambient conditions. PLLA crystallized into the stable  $\alpha$  form irrespective of the solvent used for the crystallization. However, the morphology of PLLA was found to depend on the nature of the solvent used for the crystallization. It was observed that PLLA films crystallized in acetone, THF and THF/water mixture showed spherulitic morphology while the film crystallized in acetone/water mixture showed rodlike morphology. Polymer-solvent interaction, solvent evaporation rate

and film shrinking upon the removal of the solvent from the films are responsible for the formation of different morphologies. The difference in the transparency of PLLA films crystallized in various solvents appeared to be directly related to the observed morphology, surface roughness, and porosity. Lamellar thickness of the solution-crystallized PLLA films is smaller than the melt-crystallized PLLA, the initial lamellar thickness of the solvent treated films being primarily controlled by entropic barriers. Upon heating or annealing at elevated temperatures, the lamellar thickness of the solvent treated PLLA films increases. Activated amorphous chains at higher temperatures diffuse to the crystal growth front of the existing lamellae, are adsorbed to form thicker crystals.

## 2.6. References

- (1) Hopewell, J.; Dvorak, R.; Kosior, E. *Phil. Trans. R. Soc. B* **2009**, *364*, 2115-2126.
- (2) Thompson, R. C.; Moore, C. J.; vom Saal, F. S.; Swan, S. H. *Philosophical Transactions of the Royal Society B: Biological Sciences* **2009**, *364*, 2153-2166.
- (3) Lasprilla, A. J. R.; Martinez, G. A. R.; Lunelli, B. H.; Jardini, A. L.; Filho, R. M. *Biotechnology Advances* **2012**, *30*, 321-328.
- (4) Lim, L. T.; Auras, R.; Rubino, M. *Prog. Polym. Sci.* **2008**, *33*, 820-852.
- (5) Auras, R.; Lim, L.-T.; Selke, S. E. M.; Tsuji, H., *Poly(lactic acid): Synthesis, Structures, Properties, Processing, and Applications*. John Wiley & Sons: Hoboken, NJ: 2010.
- (6) Anderson, K. S.; Schreck, K. M.; Hillmyer, M. A. *Polymer Reviews* **2008**, *48*, 85-108.
- (7) Ma, Z.; Gao, C.; Gong, Y.; Shen, J. *Biomaterials* **2005**, *26*, 1253-1259.
- (8) Sasaki, S.; Asakura, T. *Macromolecules* **2003**, *36*, 8385-8390.
- (9) Hoogsteen, W.; Postema, A. R.; Pennings, A. J.; Ten Brinke, G.; Zugenmaier, P. *Macromolecules* **1990**, *23*, 634-642.
- (10) Wasanasuk, K.; Tashiro, K.; Hanesaka, M.; Ohhara, T.; Kurihara, K.; Kuroki, R.; Tamada, T.; Ozeki, T.; Kanamoto, T. *Macromolecules* **2011**, *44*, 6441-6452.
- (11) Wasanasuk, K.; Tashiro, K. *Polymer* **2011**, *52*, 6097-6109.
- (12) Kawai, T.; Rahman, N.; Matsuba, G.; Nishida, K.; Kanaya, T.; Nakano, M.; Okamoto, H.; Kawada, J.; Usuki, A.; Honma, N.; Nakajima, K.; Matsuda, M. *Macromolecules* **2007**, *40*, 9463-9469.

- 
- (13) Zhang, J.; Tashiro, K.; Tsuji, H.; Domb, A. J. *Macromolecules* **2008**, *41*, 1352-1357.
- (14) Zhang, J.; Duan, Y.; Sato, H.; Tsuji, H.; Noda, I.; Yan, S.; Ozaki, Y. *Macromolecules* **2005**, *38*, 8012-8021.
- (15) Pan, P.; Kai, W.; Zhu, B.; Dong, T.; Inoue, Y. *Macromolecules* **2007**, *40*, 6898-6905.
- (16) Marubayashi, H.; Asai, S.; Sumita, M. *Polymer* **2012**, *53*, 4262-4271.
- (17) Marubayashi, H.; Akaishi, S.; Akasaka, S.; Asai, S.; Sumita, M. *Macromolecules* **2008**, *41*, 9192-9203.
- (18) Eling, B.; Gogolewski, S.; Pennings, A. J. *Polymer* **1982**, *23*, 1587-1593.
- (19) Puiggali, J.; Ikada, Y.; Tsuji, H.; Cartier, L.; Okihara, T.; Lotz, B. *Polymer* **2000**, *41*, 8921-8930.
- (20) Sawai, D.; Takahashi, K.; Sasashige, A.; Kanamoto, T.; Hyon, S.-H. *Macromolecules* **2003**, *36*, 3601-3605.
- (21) Cartier, L.; Okihara, T.; Ikada, Y.; Tsuji, H.; Puiggali, J.; Lotz, B. *Polymer* **2000**, *41*, 8909-8919.
- (22) Marubayashi, H.; Asai, S.; Sumita, M. *Macromolecules* **2012**, *45*, 1384-1397.
- (23) Marubayashi, H.; Asai, S.; Sumita, M. *J. Phys. Chem. B* **2013**, *117*, 385-397.
- (24) Rizzo, P.; Ianniello, G.; Venditto, V.; Tarallo, O.; Guerra, G. *Macromolecules* **2015**, *48*, 7513-7520.
- (25) Shaiju, P.; Murthy, N. S.; Gowd, E. B. *Macromolecules* **2016**, *49*, 224-233.
- (26) Lv, R.; Na, B.; Tian, N.; Zou, S.; Li, Z.; Jiang, S. *Polymer* **2011**, *52*, 4979-4984.
- (27) Lan, Q.; Li, Y.; Chi, H. *Macromolecules* **2016**, *49*, 2262-2271.
- (28) Nagarajan, S.; Gowd, E. B. *Macromolecules* **2015**, *48*, 5367-5377.
- (29) Nagarajan, S.; Deepthi, K.; Gowd, E. B. *Polymer* **2016**, *105*, 422-430.
- (30) Gowd, E. B.; Tashiro, K.; Ramesh, C. *Prog. Polym. Sci.* **2009**, *34*, 280-315.
- (31) Naga, N.; Yoshida, Y.; Inui, M.; Noguchi, K.; Murase, S. *J. Appl. Polym. Sci.* **2011**, *119*, 2058-2064.
- (32) Wu, N.; Lang, S.; Zhang, H.; Ding, M.; Zhang, J. *J. Phys. Chem. B* **2014**, *118*, 12652-12659.
- (33) Milano, G.; Guerra, G. *Prog. Mater. Sci.* **2009**, *54*, 68-88.
- (34) Tashiro, K.; Ueno, Y.; Yoshioka, A.; Kobayashi, M. *Macromolecules* **2001**, *34*, 310-315.

- 
- (35) Hashida, T.; Tashiro, K.; Aoshima, S.; Inaki, Y. *Macromolecules* **2002**, *35*, 4330-4336.
- (36) Yoshioka, A.; Tashiro, K. *Macromolecules* **2004**, *37*, 467-472.
- (37) Vittoria, V.; de Candia, F.; Iannelli, P.; Immirzi, A. *Makrom. Chem. Rapid. Commun.* **1988**, *9*, 765-769.
- (38) Ouyang, H.; Lee, W.-H.; Ouyang, W.; Shiue, S.-T.; Wu, T.-M. *Macromolecules* **2004**, *37*, 7719-7723.
- (39) Pan, P.; Han, L.; Shan, G.; Bao, Y. *Macromolecules* **2014**, *47*, 8126-8130.
- (40) Isaacson, R. B.; Kirshenbaum, I.; Feist, W. C. *J. Appl. Polym. Sci.* **1964**, *8*, 2789-2799.
- (41) Brydson, J. A., *Plastics materials*. Butterworth-Heinemann: 1999.
- (42) Tsuji, H.; Takai, H.; Fukuda, N.; Takikawa, H. *Macromolecular Materials and Engineering* **2006**, *291*, 325-335.
- (43) Vyavahare, O.; Ng, D.; Hsu, S. L. *J. Phys. Chem. B* **2014**, *118*, 4185-4193.
- (44) Strobl, G. R.; Schneider, M. *Journal of Polymer Science: Polymer Physics Edition* **1980**, *18*, 1343-1359.
- (45) Xue, Y. Q.; Tervoort, T. A.; Rastogi, S.; Lemstra, J. *Macromolecules* **2000**, *33*, 7084-7087.
- (46) Welch, P.; Muthukumar, M. *Physical review letters* **2001**, *87*, 218302.
- (47) Garber, C. A.; Geil, P. H. *Makromol. Chem.* **1966**, *98*, 304-306.
- (48) Tranchida, D.; Piccarolo, S.; Deblieck, R. A. C. *Measurement Science and Technology* **2006**, *17*, 2630.
- (49) Rastogi, S.; Spoelstra, A. B.; Goossens, J. G. P.; Lemstra, P. J. *Macromolecules* **1997**, *30*, 7880-7889.
- (50) Dreyfuss, P.; Keller, A. *Journal of Macromolecular Science, Part B* **1970**, *4*, 811-835.
- (51) Peterlin, A. *J. Polym. Sci. B* **1963**, *1*, 279-284.
- (52) Mandelkern, L.; Sharma, R.; Jackson, J. *Macromolecules* **1969**, *2*, 644-647.
- (53) Keller, T.; Grosch, M.; Jandt, K. D. *Macromolecules* **2007**, *40*, 5812-5819.
- (54) Murthy, N. S.; Wang, Z.-G.; Hsiao, B. S. *Macromolecules* **1999**, *32*, 5594-5599.
- (55) Konishi, T.; Sakatsuji, W.; Fukao, K.; Miyamoto, Y. *Macromolecules* **2016**, *49*, 2272-2280.

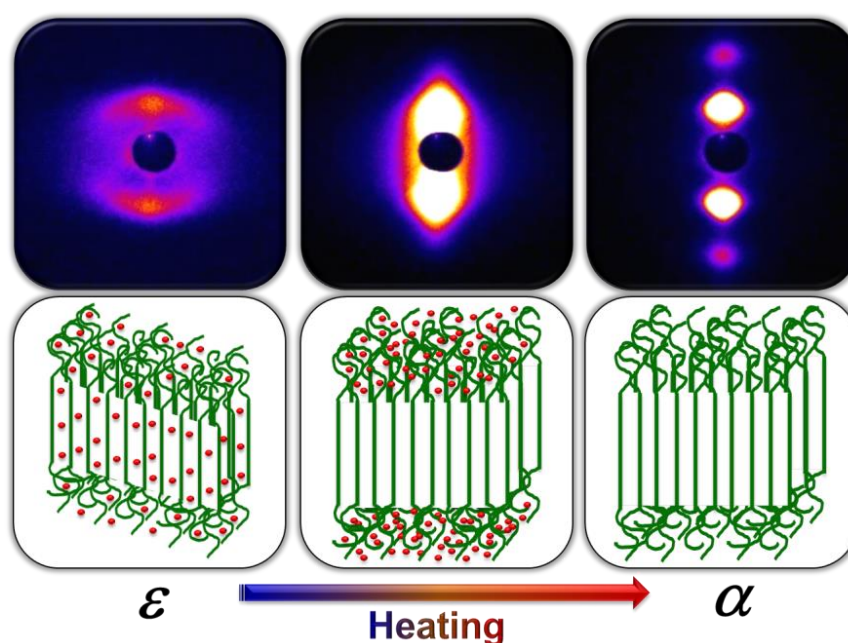
- (56) Ivanov, D. A.; Amalou, Z.; Magonov, S. N. *Macromolecules* **2001**, *34*, 8944-8952.

---

---

## Poly(L-lactide) (PLLA) Cocrystals: Structural Changes on Multiple Length Scales during Cyclopentanone (CPO) Desorption in PLLA/CPO Cocrystals

---



### 3.1. Abstract

*Structural changes in poly(L-lactide) (PLLA)/cyclopentanone (CPO) cocrystals were studied at molecular, crystalline and lamellar length-scales using different characterization techniques. Treatment of amorphous PLLA with certain organic solvent like CPO at subambient temperatures results in the formation of  $\epsilon$  cocrystal, where the solvent molecules are incorporated into the crystal lattice of PLLA. The transformation of this structure into the  $\alpha$  form during solvent desorption and the accompanying changes in the lamellar structure were followed by various analytical measurements on PLLA/CPO cocrystals. SANS data suggested that CPO is present stoichiometrically in the crystal lattice and as clusters in the interlamellar amorphous regions in the touch dried samples. DSC thermogram showed a sharp endotherm during this  $\epsilon$  to  $\alpha$  transition. X-ray fiber*

diagrams showed that the  $\varepsilon$  form transforms to the  $\alpha$  form over a temperature range (40–55 °C) as the solvent molecules are expelled from the crystalline lattice, while maintaining chain orientation. Infrared spectra showed the splitting of the  $\text{CH}_3$  symmetric deformation band at  $1383\text{ cm}^{-1}$  into a doublet ( $1382$  and  $1386\text{ cm}^{-1}$ ) at  $\varepsilon$  to  $\alpha$  transition indicating the desorption of CPO molecules from the crystal lattice. Changes in the invariant in SAXS data are interpreted as due to the migration of the solvent from the crystalline phase to the amorphous phase during the  $\varepsilon$  to  $\alpha$  transition followed by the evaporation of the solvent from the entire polymer. During this transition, lamellae that are tilted in the presence of CPO in the crystal lattice become perpendicular to the chain axis. In addition, there are changes in long period, lamellar thickness, and amorphous thickness. Continuing the desorption to dryness by further heating results in the removal of the solvent molecules in the amorphous phase of the  $\alpha$  form. This is accompanied by increased crystallinity. These studies show that the solvent desorption results in a precise sequence of quantifiable structural changes at multiple length scales.

### 3.2. Introduction

PLLA, the most common stereoisomer of poly(lactic acid), is a widely used biobased polymer in degradable plastics. It is also used as a degradable biomaterial in many medical devices and tissue engineering.<sup>1-3</sup> One of the major drawbacks of PLLA is its poor crystallization rate and low crystallinity. Several methods have been reported for improving the crystallization rate of PLLA like the incorporation of fillers such as carbon nanotube and blending with other polymers etc.<sup>25-30</sup> Crystallization of glassy PLLA could be effectively improved by using solvent-induced crystallization,<sup>31, 32</sup> a method commonly used to obtain crystalline forms in many polymers.<sup>33-40</sup> This method has been successfully used to accelerate the crystallization process of polymers and also to enhance the crystallinity of polymers.<sup>31</sup> Diffusion of the solvent through the glassy polymer plays a crucial role in the crystallization process. The interaction between the random coils and the solvent molecules induces the micro-Brownian motion of the amorphous chains by reducing the glass transition temperature of the polymer.<sup>41</sup> This widens

the temperature window between the glass transition and melting temperatures, which in turn facilitates crystallization at lower temperatures. It was shown that the solvent-specific competition between solvent-induced crystallization and dissolution in PLLA thin films control the crystallinity of the polymer.<sup>32</sup> However, in certain cases, the polymers are known to form cocrystals by incorporating the solvent molecules inside their crystal lattice.<sup>18, 33-36, 38, 39, 42</sup> Several reports are available on the formation of cocrystals by polymers like syndiotactic polystyrene (sPS),<sup>34, 36-40</sup> poly(vinyl alcohol) (PVA),<sup>43-45</sup> polyethyleneimine (PEI),<sup>35, 46, 47</sup> etc.

Recently, it was found that PLLA can form  $\varepsilon$  cocrystals in the presence of certain solvents like N, N-dimethylformamide (DMF), cyclopentanone (CPO), tetrahydrofuran(THF), etc. at subambient temperatures.<sup>18, 19</sup> Rizzo et al. showed that PLLA chains exhibit the 10/7 helical conformation in PLLA/CPO cocrystals and 16 CPO guest molecules are packed according to the space group P2<sub>1</sub>2<sub>1</sub>2<sub>1</sub> in an orthorhombic lattice (a = 1.61 nm, b = 1.26 nm, and c = 2.90 nm).<sup>48</sup> PLLA was also found to produce gels in the presence of certain solvents, which is capable of producing  $\varepsilon$  cocrystals.<sup>49, 50</sup> The solvent in the gel can be exchanged with other solvents, like water by dipping the gel in the corresponding solvents.<sup>49</sup> The  $\varepsilon$  to  $\alpha$  transition was also observed in the case of gels, without altering the morphology during the solvent exchange.<sup>49</sup> The  $\varepsilon$  cocrystal is less stable and transforms into the  $\alpha$  form at room temperature with solvent desorption.<sup>18</sup>

Since the cocrystal formation of PLLA with solvents is a recent observation in PLLA crystallization, solvent desorption process from the cocrystals during heating and its influence on the crystalline transitions and the lamellar morphology have not been investigated. Therefore, temperature-dependent wide-angle and small-angle X-ray scattering (WAXS/SAXS), small-angle neutron scattering (SANS), differential scanning calorimetry (DSC), and thermogravimetric analysis (TGA) measurements were carried out using uniaxially drawn  $\varepsilon$  form samples to elucidate the structural changes involved in the solvent desorption process. Since crystal-crystal transitions in semicrystalline polymers are concomitant with the changes in polymer chain conformation, the conformational changes in the PLLA

$\varepsilon$  form during the heating process were investigated using in-situ Fourier transform infrared spectroscopy (FTIR). In this chapter, a structural model is proposed to explain the changes that accompany heat-induced solvent desorption process during  $\varepsilon$  to  $\alpha$  transition.

### 3.3. Experimental

**3.3.1. Materials:** PLLA ( $M_w \sim 260000$ ,  $D \sim 1.5$ ) was purchased from Sigma-Aldrich. The glass transition and melting temperature of PLLA were 60 and 177 °C, respectively. The solvent cyclopentanone (CPO) [purity  $\geq 99\%$ ] was purchased from Merck and used as received.

#### 3.3.2. Sample Preparation

**Amorphous Samples:** Amorphous films of PLLA were prepared by quenching the melt into liquid nitrogen.

**Uniaxially Drawn Samples:** Uniaxially drawn samples were prepared by stretching a small rectangular piece ( $\sim 12 \times 2$  mm; thickness  $\sim 1$  mm) of the amorphous film to about four times its original length above a hot plate  $\sim 60$  °C i.e. near the glass transition temperature of PLLA.

**PLLA Cocrystals:** Uniaxially drawn and undrawn films were immersed in CPO and DMF for 30 days and in THF for 7 days at around  $-15$  °C to obtain the cocrystals. The samples removed from the solvents were wiped dry with tissue and kept at ambient temperature for 5 min before measurements. These samples are referred to as touch dry samples.

#### 3.3.3. Characterization

**Differential Scanning Calorimetry (DSC):** DSC measurements were carried out using Perkin-Elmer Pyris 6 DSC. The  $\varepsilon$  cocrystal was heated from 0 to 190 °C at the rate of 10 °C/min to observe the transitions involved in the heating process.

**Thermogravimetric Analysis (TGA):** The amount of solvent present in the  $\varepsilon$  cocrystal was measured using TGA (TA instruments Q50). The measurements were performed at a heating rate of 10 °C/min under the nitrogen atmosphere.

**Small-angle Neutron Scattering (SANS):** Amorphous PLLA samples were immersed in deuterated CPO (C/D/N Isotopes Inc. Quebec, Canada) for six months in a refrigerator. SANS experiments were performed on the extended Q-range small-angle neutron scattering (EQ-SANS, BL-6) beam line at the Spallation Neutron Source (SNS) located at Oak Ridge National Laboratory (ORNL). In 60 Hz operation mode, a 4 m sample-to-detector distance with 2.5-6.1 and 10.0-13.6 Å wavelength bands were used to obtain the relevant wave vector transfer,  $q = 4\pi \sin(\theta)/\lambda$ , where  $2\theta$  is the scattering angle.<sup>51</sup> Samples were loaded into 1 mm path length circular-shaped quartz cuvettes (Hellma USA, Plainville, NY) and SANS measurements performed at 10 °C. Data reduction followed standard procedures using Mantid Plot.<sup>52</sup> The measured scattering intensity was corrected for the detector sensitivity and scattering contribution from the solvent and empty cells, and then placed on absolute scale using a calibrated standard.<sup>53</sup>

**X-ray Measurements:** Wide-angle and small-angle X-ray scattering (WAXS/SAXS) measurements were performed using XEUSS SAXS/WAXS system by Xenocs, operated at 50 kV and 0.60 mA. For more details, please refer to chapter 2.

The degree of crystallinity was determined from the area under the X-ray reflections by profile fitting the 1D WAXD scans using the GRAMS 32 software. The degree of crystallinity ( $X_c$ ) was calculated using the following equation based on the scattering intensities of crystalline ( $A_c$ ) and amorphous ( $A_a$ ) phases.

$$X_c = 100 \times A_c / (A_c + A_a) \quad (1)$$

**SAXS Data Analysis:** The two-dimensional SAXS images were azimuthally integrated to obtain 1D scattering intensity profiles as a function of  $q$ , with  $2\theta$  being the scattering angle and  $\lambda$  is the X-ray wavelength. The resulting scattering intensity SAXS profiles were corrected for background scattering. To resolve the structure parameters of the lamellar structure such as long period ( $L$ ), lamellar thickness ( $l_c$ ) and amorphous thickness ( $l_a$ ), normalized one-dimensional electron density correlation function was derived from the small-angle X-ray scattering curves.

With the assumption of stacked lamellar structure (crystalline and amorphous layers), the normalized one-dimensional electron density correlation function ( $K(z)$ ) is defined as follows.<sup>55</sup>

$$K(z) = \int_0^\infty q^2 I(q) \cos(qz) dq \quad (2)$$

Where  $z$  is normal to the layer faces in the lamellar stack, and  $I(q)$  is the scattered intensity. The various lamellar structural parameters were calculated from the  $K(z)$  curve as shown in Figure 3.1. The invariant  $Q$ , which represents the total integrated scattering, was calculated from the Lorentz-corrected SAXS patterns using the following equation.

$$Q = \int_0^\infty q^2 I(q) dq \quad (3)$$

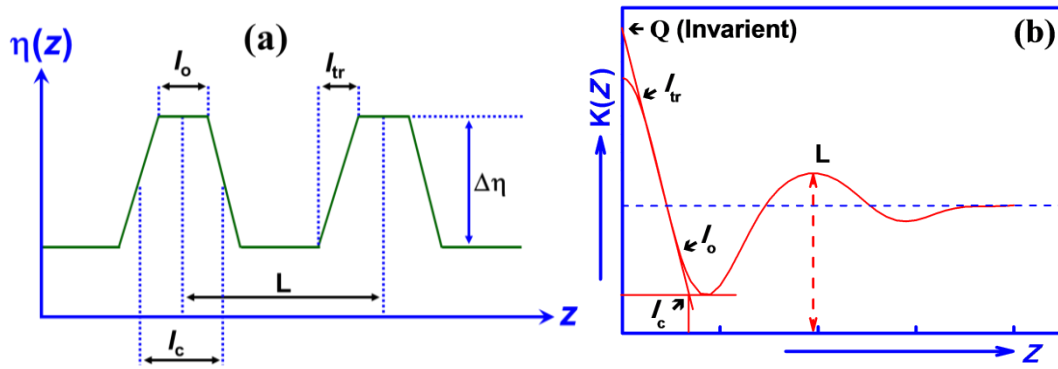


**Figure 3.1.** Electron density distribution  $\eta(z)$  and the one-dimensional electron density correlation function  $K(z)$  for the lamellar system.  $Q$  is the invariant,  $l_{tr}$  the thickness of the transition zone between the crystalline lamella and amorphous part,  $l_o$  the thickness of the lamellar core,  $l_c$  the mean lamellar thickness, and  $L$  the long period.

The change in invariant value reflects the changes in the difference in the electron density between the crystalline and amorphous regions. The  $Q$  values estimated using equation (3) gives the change in the electron density gap ( $\Delta\eta$ ) between the crystalline ( $\eta_c$ ) and amorphous ( $\eta_a$ ) regions.<sup>56</sup>

$$Q = V\phi_c(1-\phi_c)(\eta_c-\eta_a)^2 \quad (4)$$

Where  $V$  is the volume fraction of the lamellar stacks calculated by  $X_c/\phi_c$  and  $\phi_c$  is the crystallinity estimated from the lamellar thickness  $\langle d \rangle$  and the long period ( $L$ ):

$$\phi_c = \langle d \rangle / L \quad (5)$$

**Infrared Measurements:** Infrared spectra were collected using Perkin Elmer FTIR spectrometer-2. For these measurements, very thin amorphous films (thickness  $\sim 15\mu\text{m}$ ) were prepared by drop casting a dilute solution of PLLA in chloroform onto the surface of KBr pellet, followed by evaporation of the solvent at a faster rate. These samples were further immersed in CPO for 30 days to obtain the  $\varepsilon$  form films. The FTIR spectra were collected with a resolution of  $2\text{ cm}^{-1}$  and 32 scans were accumulated. The variable temperature infrared spectra were collected using the same Linkam hot stage used for the WAXS/SAXS measurements.

### 3.4. Results and Discussion

#### 3.4.1. Stability of PLLA Cocrystals at Room Temperature

Cocrystals of PLLA were prepared using different solvents such as CPO, DMF and THF. The structure of the samples was confirmed from the WAXS results. In order to check the stability of the prepared cocrystals, WAXS measurements of the cocrystals were performed after keeping at room temperature for 1 day. The results were compared with that of touch dry samples (samples that are wiped dry with tissue and kept at ambient temperature for 5 min.) as shown in Figure 3.2. It has been already reported by Marubayashi et al. that the  $\varepsilon$  cocrystal is unstable at room temperature and gets transformed into the  $\alpha$  form with solvent desorption.<sup>18</sup> Moreover, they have explained the dependence of solvent desorption on the  $\varepsilon$  to  $\alpha$  transition, in terms of solvent solubility. Thickness of the sample affects the diffusion behavior of solvent molecules in the amorphous region. Hence the time taken for the solvent desorption will be more, and as a result the transition from  $\varepsilon$  to  $\alpha$  becomes slow. Therefore, in the present study, films having thickness  $\sim 1\text{ mm}$  were used for all the X-ray measurements.

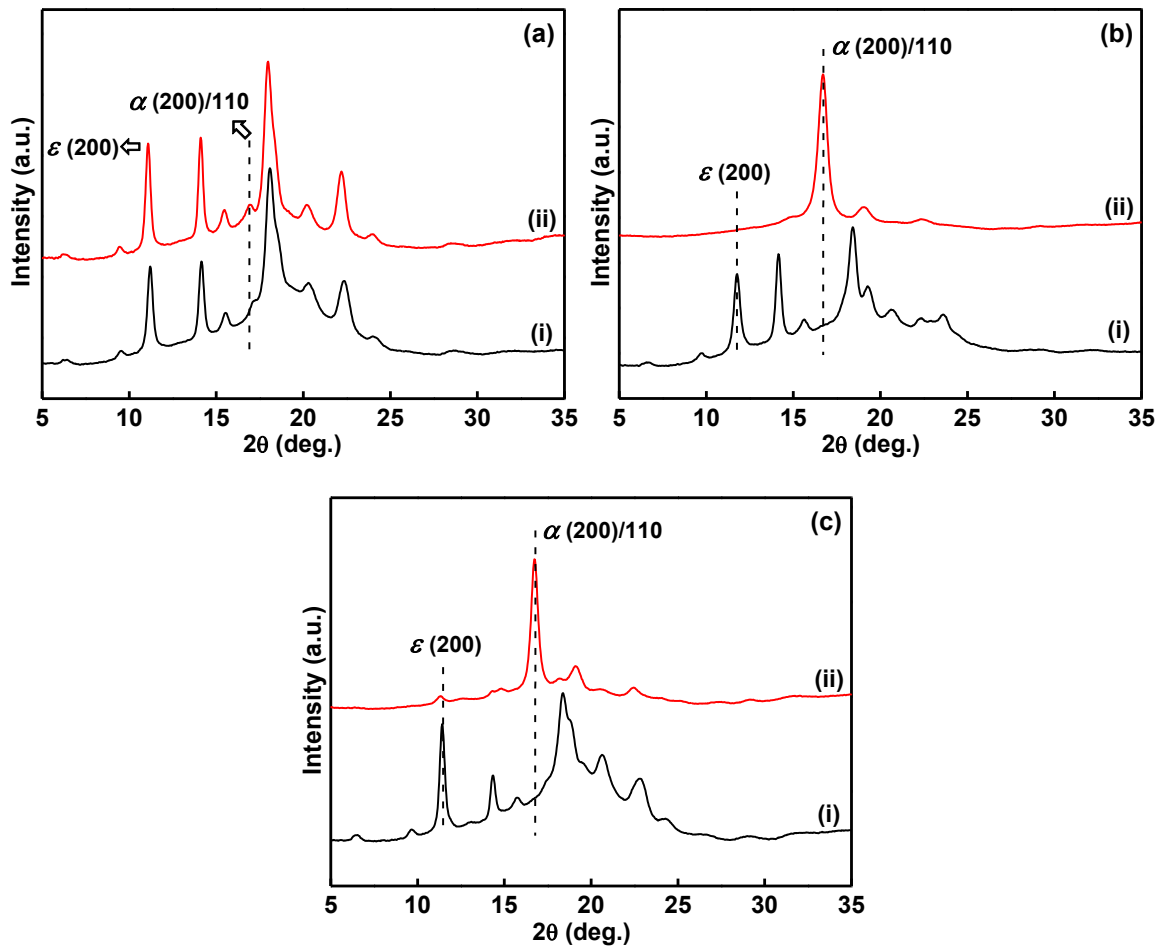


**Figure 3.2.** WAXS patterns obtained for (a) PLLA/CPO cocrystal (b) PLLA/DMF cocrystal (c) PLLA/THF cocrystal, (i) touch dry samples and (ii) after keeping at room temperature for one day.

It is evident from Figure 3.2a that in the intensity of  $\varepsilon$  form reflection (200) in PLLA/CPO cocrystal remains almost unchanged even after keeping at room temperature for one day. However, the simultaneous appearance of  $\alpha$  form reflection (200/110) with low intensity indicates the slow transition from  $\varepsilon$  to  $\alpha$ . On the other hand, for PLLA/DMF and PLLA/THF cocrystals, the  $\varepsilon$  form reflection (200) has almost vanished after keeping the samples at room temperature for one day and at the same time  $\alpha$  form reflection (200/110) with predominant intensity has appeared (Figure 3.2b and 3.2c). Moreover, the other peaks of  $\varepsilon$  form at  $2\theta = 6.3^\circ$ ,  $14.1^\circ$ ,  $18.1^\circ$ ,  $20.2^\circ$ , and  $22.2^\circ$  has also disappeared, which indicates the complete transition from  $\varepsilon$  to  $\alpha$ . These results specify that the  $\varepsilon$  to  $\alpha$  transition is quite rapid in the case of PLLA/DMF and PLLA/THF cocrystals

compared to PLLA/CPO cocrystal. Therefore, PLLA/CPO cocrystal was further used for a detailed study.

### 3.4.2. Thermal Behavior of PLLA/CPO Cocrystal ( $\epsilon$ )

Figure 3.3a shows the TGA thermogram of touch dry PLLA/CPO cocrystal ( $\epsilon$  form) films. Upon heating from room temperature, the weight loss due to the evaporation of CPO started at  $\sim 45$  °C. No further weight loss occurs after the melting of PLLA (175 °C), suggesting the complete evaporation of CPO molecules from the PLLA/CPO cocrystal film at this temperature. It is obvious from the TGA thermogram that the total content of the CPO in a touch dry sample is  $\sim 27$  wt%. It is to be noted that in such dried samples, the solvent molecules are known to be distributed both in crystalline and amorphous regions.<sup>57, 58</sup>

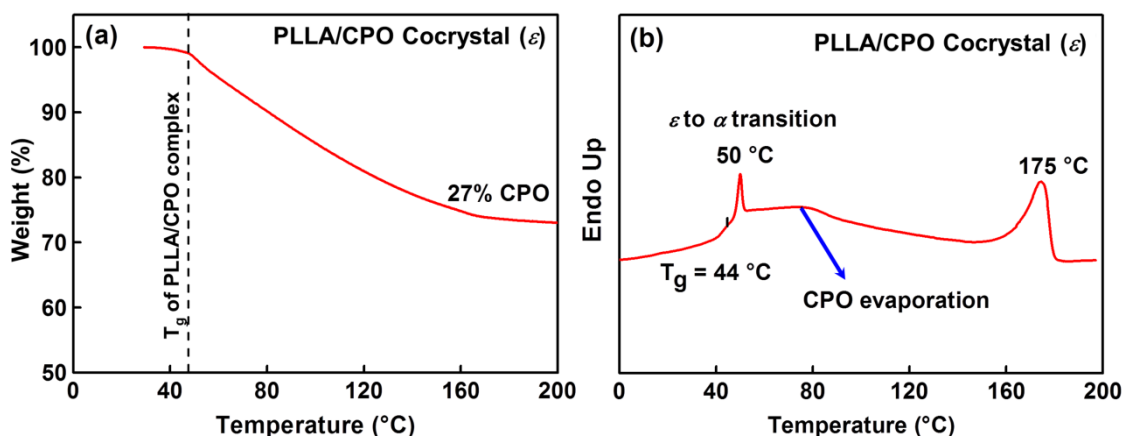


**Figure 3.3.** (a) TGA thermogram of PLLA/CPO cocrystal measured in the heating process (b) DSC thermogram of PLLA/CPO cocrystal measured in the heating process.

DSC thermogram of touch dry PLLA/CPO cocrystal film was measured during the heating process. As seen in Figure 3.3b, there are multiple overlapping transitions observed in the temperature range of 40–80 °C. Upon heating from 0 °C, a shift in the baseline is observed first in the temperature range of 40–47 °C. This can be assigned to the glass transition temperature ( $T_g$ ) of PLLA/CPO cocrystal. The observed reduction of the  $T_g$  from 60 °C in PLLA to 44 °C in PLLA/CPO cocrystals can be attributed to the plasticization of the polymer by CPO molecules, which reside in the amorphous phase of the touch dry sample. Similar observation was also reported in syndiotactic polystyrene/solvent

complexes.<sup>41, 58</sup> On further heating, three additional transitions are observed: a sharp endothermic peak  $\sim 50$  °C, a broad endothermic peak  $\sim 80$  °C, and a sharp endothermic peak at 175 °C. Temperature-dependent WAXS, SAXS and FTIR measurements discussed later show that these transitions are due to the  $\varepsilon$  to  $\alpha$  transition accompanied by expulsion of the CPO molecules from the crystal lattice to the amorphous phase, to the complete evaporation of CPO molecules, and to the melting of PLLA, respectively.

### 3.4.3. Crystalline Transition during Heating by *in-situ* WAXS

The phase transition behavior of the  $\varepsilon$  form of PLLA during the heating was studied by utilizing the uniaxially drawn samples to avoid the overlap of equatorial and meridional reflections in the X-ray diffraction patterns. Figure 3.4 shows the X-ray fiber diagrams collected at different temperatures starting from the  $\varepsilon$  form of PLLA/CPO cocrystals.

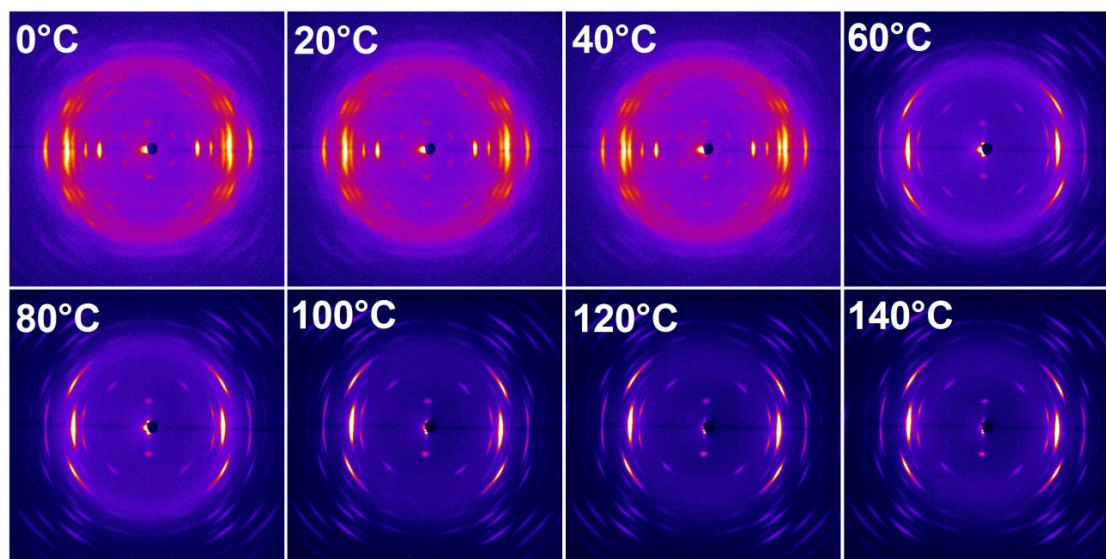


**Figure 3.4.** Two-dimensional WAXS images obtained at different temperatures during heating process for the uniaxially drawn PLLA/CPO cocrystal.

The fiber diagram at 0 °C is very similar to that from the  $\varepsilon$  form of PLLA obtained by Marubayashi et al.<sup>18</sup> In this 0 °C pattern, the Bragg reflections of the  $\varepsilon$  form structure are superimposed on a broad diffuse scattering. On heating, at  $\sim 50$  °C, a new fiber diagram appears indicating a major structural change. This new

fiber diagram can be attributed to the  $\alpha$  form of PLLA.<sup>18</sup> DSC thermogram showed a sharp endotherm in this temperature range indicating the structural transition from  $\varepsilon$  to  $\alpha$ . The molecular chain orientation remains unchanged during the transition as evident from the X-ray fiber diagrams. No evidence of structural disorder was observed in the X-ray fiber diagrams above the transition temperature.

To further understand the structural changes, the fiber diagrams were azimuthally averaged [ $I(2\theta) = \int I(2\theta, \phi) d\phi$ ] to obtain 1D scans shown in Figure 3.5a. The reflections corresponding to the  $\varepsilon$  form ( $2\theta = 6.3^\circ, 11.1^\circ, 14.1^\circ, 18.1^\circ, 20.2^\circ$ , and  $22.2^\circ$ ) started to decrease its intensity at 40 °C and completely disappear at 55 °C. Simultaneously, new reflections characteristic of the  $\alpha$  form ( $2\theta = 6.0^\circ, 12.5^\circ, 14.8^\circ, 16.6^\circ, 19.1^\circ$ , and  $25.0^\circ$ ) appear at 40 °C and their intensity increases up to 120 °C. The Miller indices of  $\varepsilon$  and  $\alpha$  forms shown in the figure are those reported in the literature.<sup>5, 18</sup> The changes in the integrated intensities of the 200 reflection of the  $\varepsilon$  form and the 200/110 reflection of the  $\alpha$  form was evaluated by profile fitting the 1D scans and plotted against temperature in Figure 3.5b. It is evident from Figure 3.5 that the  $\varepsilon$  form transformed to the  $\alpha$  form over a broad temperature range (40–55 °C) and both these forms coexist in this temperature range.

Marubayashi et al. reported that the  $\varepsilon$  to  $\alpha$  transition occurs in PLLA-solvent complexes due to the solvent desorption.<sup>18</sup> This implies that the CPO molecules residing in the crystal lattice of the  $\varepsilon$  form have been ejected into the amorphous phase of PLLA in the temperature range of 40–55 °C and, as a result, the  $\varepsilon$  form is transformed to the  $\alpha$  form. In this context,  $T_g$  plays an important role on the solvent desorption from the crystal lattice of PLLA. The  $T_g$  observed for the PLLA/CPO cocrystals is around 44 °C (Figure 3.3b). Just above the  $T_g$ , a sharp endothermic peak was observed at 50 °C in the DSC thermogram that could be due to the expulsion of CPO molecules from the crystal lattice of PLLA. It can also be seen from the TGA thermogram (Figure 3.3a) that the solvent desorption starts at the  $T_g$  of PLLA cocrystal (44 °C). We speculate that the CPO molecules in the

crystal lattice of PLLA are kinetically stable. Once the amorphous phase becomes mobile at elevated temperatures, the CPO molecules readily diffuse out of the crystal lattice into the amorphous domain and stay in the amorphous phase until the boiling point of CPO (131 °C). It is worth mentioning here that Gowd et al. showed that the  $T_g$  of host polymer plays an important role in expelling out the solvent from the sPS-solvent complexes.<sup>58</sup> The  $\delta$  cocrystal to  $\gamma$  transition in sPS-solvent complexes occurs by solvent desorption over a broad temperature range just above the  $T_g$  of sPS (97 °C).<sup>42, 58-64</sup>

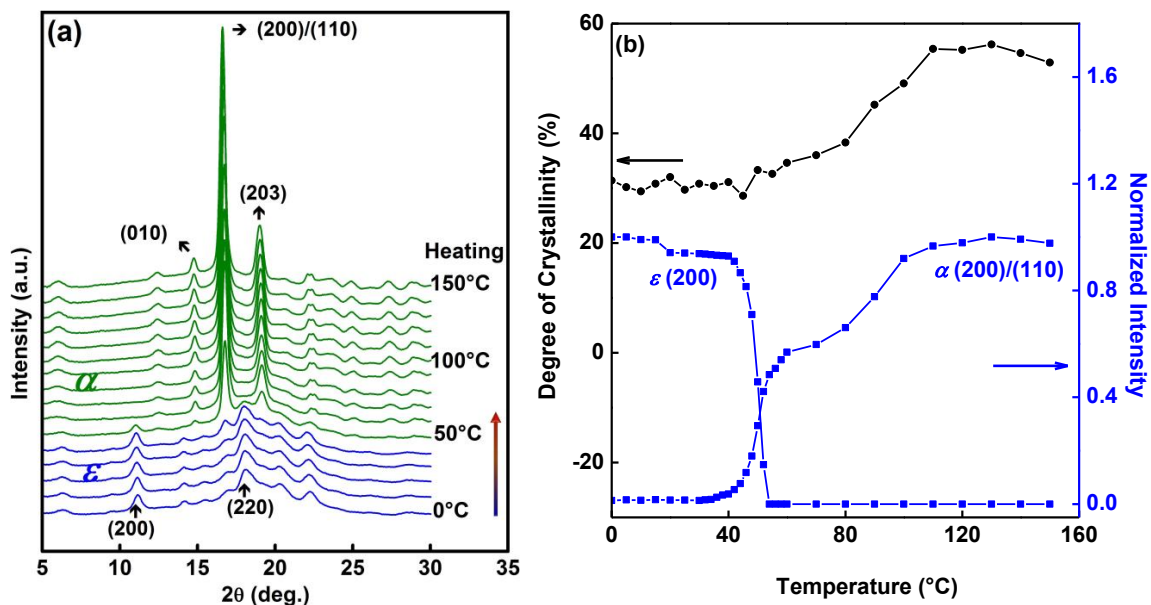


**Figure 3.5.** (a) Temperature dependence of (a) one-dimensional WAXS patterns evaluated from Figure 3.4 (b) the normalized intensity of the reflections at  $2\theta = 11.2^\circ$  ( $\epsilon$ ), and  $16.6^\circ$  ( $\alpha$ ) and degree of crystallinity evaluated from (a).

The X-ray diffraction scans did not show any evidence of new crystalline phase in the temperature range of 40–55 °C. It means no intermediate phase or emptied crystal lattice is observed during the  $\epsilon$  to  $\alpha$  transition. The  $\epsilon$  form becomes unstable after the solvent desorption and on further heating, the unstable lattice readily transforms to the more stable  $\alpha$  form because of the thermal mobility of the PLLA chains. Both  $\epsilon$  and  $\alpha$  forms coexist over a broad temperature range of 40–55 °C. The temperature-dependent infrared spectra were measured for the PLLA/CPO cocrystal to understand the conformational changes and the solvent desorption and the details will be discussed in the later section.

Figure 3.5b shows the temperature dependence of the degree of crystallinity estimated from the 1D WAXS scans shown in Figure 3.5a. The degree of crystallinity estimated for the PLLA/CPO cocrystal at 0 °C is ~30%, and it remains constant in the temperature range of 0–60 °C. The degree of crystallinity increased with increasing temperature up to 120 °C and it remains essentially constant above 120 °C, up to the melting temperature of PLLA. The integrated intensities of the 200/110 reflection of the  $\alpha$  form plotted against temperature show the stepwise increase of the intensity of the  $\alpha$  form reflection. The increase in the intensity of the 200/110 reflection in the temperature range of 40–60 °C corresponds to the  $\varepsilon$  to  $\alpha$  transition. On further heating, the intensity value of the 200/110 reflection shows a distinct deviation from linearity above the  $\varepsilon$  to  $\alpha$  transition in the temperature range of 60–120 °C. The broad diffuse scattering observed in the fiber diagrams (Figure 3.4) also disappears in the same temperature range. This could be attributed to the evaporation of the solvent and the crystallization of some of the amorphous phase of the PLLA into the ordered  $\alpha$  form in the temperature range of 60–120 °C. The DSC thermogram does not show any exotherm due to PLLA crystallization in this temperature range probably because it overlaps the broad endotherm due to the evaporation of CPO molecules. We speculate that CPO molecules expelled from the crystal lattice of the  $\varepsilon$  form during  $\varepsilon$  to  $\alpha$  transition occupy the amorphous region transiently and are responsible for the crystallization of some parts of the amorphous PLLA. DSC and TGA thermograms shown in Figure 3.3 also confirmed the presence of CPO molecules at higher temperatures above the  $\varepsilon$  to  $\alpha$  transition. The CPO molecules residing in the amorphous phase of the  $\alpha$  form above the  $\varepsilon$  to  $\alpha$  transition may partially dissolve the amorphous phase of PLLA at high temperature. The activated mobility of PLLA chains at high temperature may further induce crystallization of the amorphous phase into the stable  $\alpha$  form. This increases the crystallinity in the temperature range of 60–120 °C as shown in Figure 3.5b. Gowd et al. reported the similar situation in sPS-solvent complexes, where the solvent molecules that are

residing in the amorphous phase could influence the crystallization behavior of sPS in thicker films or uniaxially drawn films.<sup>42, 58, 61</sup>

Recently, Matsuda et al. reported the structural changes in PLLA gel at different temperatures and showed that the  $\varepsilon$  to  $\alpha$  transition occurs over a broad temperature range of 27–42 °C in PLLA/DMF gel and both the forms coexist in this temperature range.<sup>49, 50</sup> They reported that the intensity of the birefringence decreased drastically in the temperature range of 27–42 °C, where the  $\varepsilon$  to  $\alpha$  transition occurred and then increased from 42–46 °C. It was also observed that the spherulitic structure was the same before and after  $\varepsilon$  to  $\alpha$  transition indicating that PLLA crystals did not melt or dissolve during the transition. The decrease in the intensity of the birefringence during the  $\varepsilon$  to  $\alpha$  transition could be because of the expulsion of solvent molecules from the crystal lattice of the  $\varepsilon$  form to the amorphous phase while retaining its shape. On further heating, again the intensity of the birefringence increased due to the crystallization of some of the amorphous phase in the presence of excess solvent molecules.

#### 3.4.4. Conformational Change by Temperature-Dependent FTIR

In order to understand the conformational changes involved in the  $\varepsilon$  to  $\alpha$  transition, temperature-dependent infrared spectra were measured in the heating process of PLLA/CPO cocrystal. The infrared spectra measured for the amorphous PLLA,  $\alpha$  form,  $\varepsilon$  form of PLLA/CPO cocrystal and CPO (solvent) were compared in Figure 3.6. It has to be noted that the infrared spectrum of the  $\varepsilon$  form is measured at 5 °C. The formation of PLLA/CPO cocrystals was supported by the presence of CPO bands in the  $\varepsilon$  form films. The infrared spectrum of the  $\varepsilon$  form looks almost similar to the spectrum of the  $\alpha$  form, except for the characteristic bands of the CPO. The presence of the crystalline band at 922 cm<sup>-1</sup>, which is associated with  $\nu(\text{CH}_3) + \nu(\text{C-COO})$  vibrational mode, confirms that the  $\varepsilon$  form takes  $10_7$  (left-handed  $10_3$ ) helical conformation, similar to that of the  $\alpha$  form.<sup>8, 65</sup>

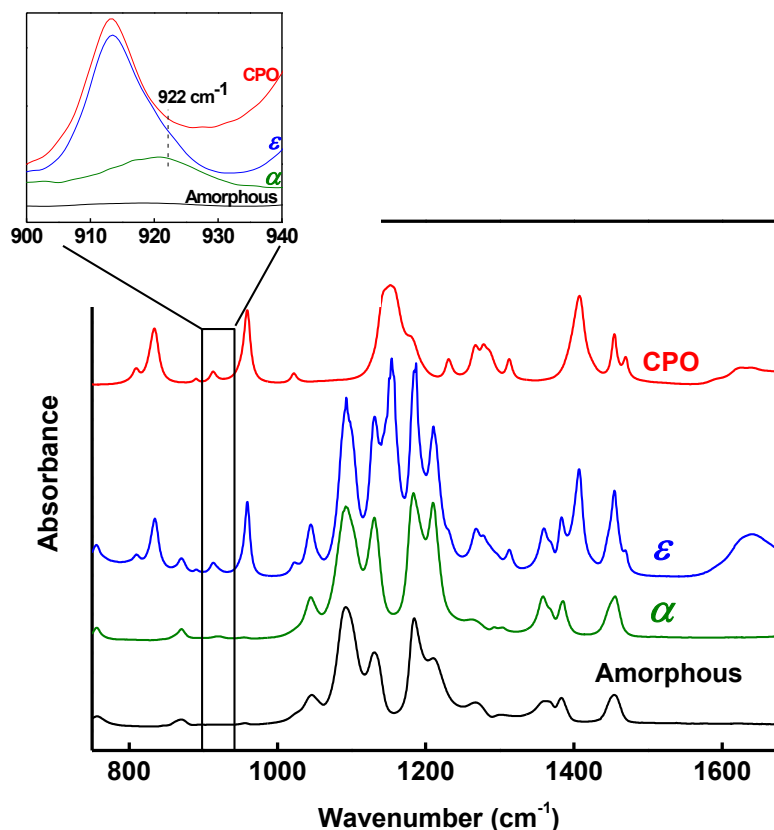


**Figure 3.6.** FTIR spectra of the amorphous,  $\alpha$ ,  $\epsilon$ , forms and CPO in the frequency region of 780–1650  $\text{cm}^{-1}$ . The Inset shows the expanded region of 900–940  $\text{cm}^{-1}$  region.

Marubayashi et al. showed that the PLLA chains in the  $\epsilon$  form take  $10_7$  (left-handed  $10_3$ ) helical conformation using the fiber diagram analysis.<sup>18</sup> The frequency region 1375–1395  $\text{cm}^{-1}$ , which is associated with the  $\text{CH}_3$  symmetric deformation showed clear spectral differences between  $\epsilon$  and  $\alpha$  forms.<sup>8, 66</sup> Figure 3.7a shows the temperature-dependent infrared spectra in the frequency region 1375–1440  $\text{cm}^{-1}$  collected during heating at 10  $^\circ\text{C}/\text{min}$  for the PLLA/CPO cocrystal. The vibrational frequency of the IR bands that are characteristic of the  $\epsilon$  form,  $\alpha$  form and CPO are plotted against temperature in Figure 3.7b. The pure crystalline band of the  $\epsilon$  form at 1383  $\text{cm}^{-1}$ , which is associated with the  $\text{CH}_3$  symmetric deformation splits into a doublet (1382 and 1386  $\text{cm}^{-1}$ ) at  $\epsilon$  to  $\alpha$  transition. It was reported that the band associated with the  $\text{CH}_3$  symmetric deformation is sensitive to the chain packing in  $\alpha'$  and  $\alpha$  forms.<sup>8, 66</sup> The  $\alpha'$  form shows a singlet at 1386  $\text{cm}^{-1}$  and on heating this band splits into a doublet (1381 and 1386  $\text{cm}^{-1}$ ) when the structure transforms to the  $\alpha$  form. This suggests that the

interaction between PLLA chains and CPO molecules affect the  $\text{CH}_3$  symmetric deformation mode of PLLA. Based on these results, we can summarize here that the frequency region  $1375\text{--}1395\text{ cm}^{-1}$ , which is associated with the  $\text{CH}_3$  symmetric deformation is sensitive to the chain packing and noticeable differences can be seen for the amorphous form (1381),  $\alpha'$  (1386),  $\alpha$  (1382 and 1386) and  $\varepsilon$  (1383) forms.

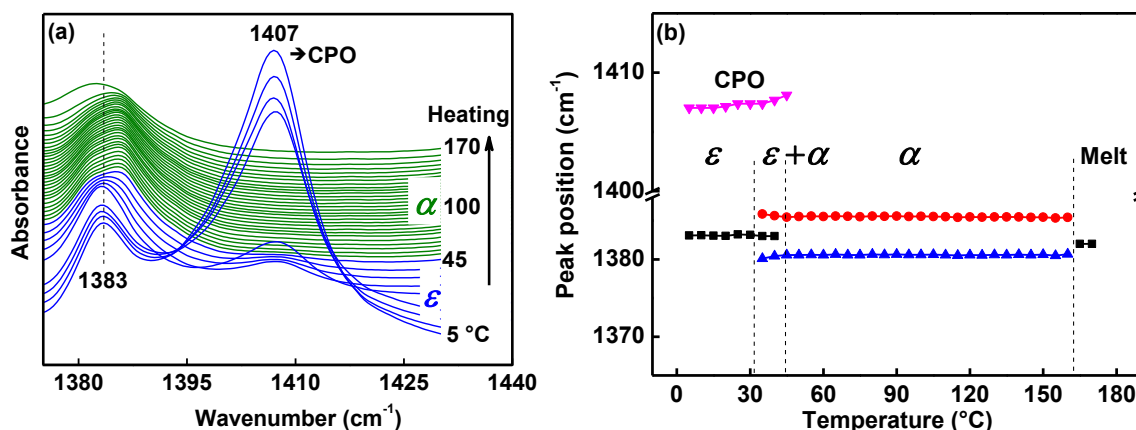


**Figure 3.7.** (a) Temperature-dependent infrared spectra of PLLA/CPO cocrystal measured during heating process from 5 to 170 °C in the frequency region of 1370–1440  $\text{cm}^{-1}$  and (b) temperature dependence of wavenumber shifts for FTIR bands of CPO,  $\varepsilon$ ,  $\alpha$ , and amorphous PLLA (melt).

It can be seen that on heating, the bands corresponding to the  $\varepsilon$  form ( $1383\text{ cm}^{-1}$ ) and CPO ( $1407\text{ cm}^{-1}$ ) disappeared at  $45\text{ }^{\circ}\text{C}$  and simultaneously the bands corresponding to the  $\alpha$  form ( $1382$  and  $1386\text{ cm}^{-1}$ ) appeared above  $35\text{ }^{\circ}\text{C}$ . The features for both the  $\varepsilon$  and  $\alpha$  forms overlap in the temperature range of  $30\text{--}45\text{ }^{\circ}\text{C}$ . The intensity of the CPO band at  $1407\text{ cm}^{-1}$  is high at  $5\text{ }^{\circ}\text{C}$ , and this band completely disappears at  $50\text{ }^{\circ}\text{C}$ , indicating the transition from  $\varepsilon$  to  $\alpha$ . The IR band at  $1407\text{ cm}^{-1}$  is assigned to the  $\text{CH}_2$  deformation of the CPO.<sup>67</sup> The  $\varepsilon$  to  $\alpha$  transition occurs slightly at lower temperatures in thin films used for the IR studies due to the faster solvent desorption. The solvent band completely disappeared at  $45\text{ }^{\circ}\text{C}$  indicating the complete evaporation of solvent from the entire polymer due to the thinner samples ( $\sim 15\mu\text{m}$ ) used for IR measurements. Gowd et al. reported that thickness of the sample affects the diffusion rate of solvent molecules in the amorphous phase as it determines the path length and the residual time of the solvent molecules in the amorphous phase.<sup>61</sup>

Another spectral region sensitive to the conformation, intra- and intermolecular interaction of PLLA chains is the carbonyl stretching region (1700–1800  $\text{cm}^{-1}$ ).<sup>8, 68, 69</sup> In this frequency region, clear differences between the disordered  $\alpha$  ( $\alpha'$ ) and  $\alpha$  forms have been reported. In the disordered  $\alpha$  ( $\alpha'$ ) form, no spectral splitting was observed in the carbonyl stretching band at 1759  $\text{cm}^{-1}$ . On the other hand, this band showed two shoulders on each side at 1749  $\text{cm}^{-1}$  and 1776  $\text{cm}^{-1}$  in the ordered  $\alpha$  form. The ordered chain packing and the strong intermolecular dipole-dipole interactions in the crystal lattice of the ordered  $\alpha$  form resulted in such splitting of the carbonyl stretching band.

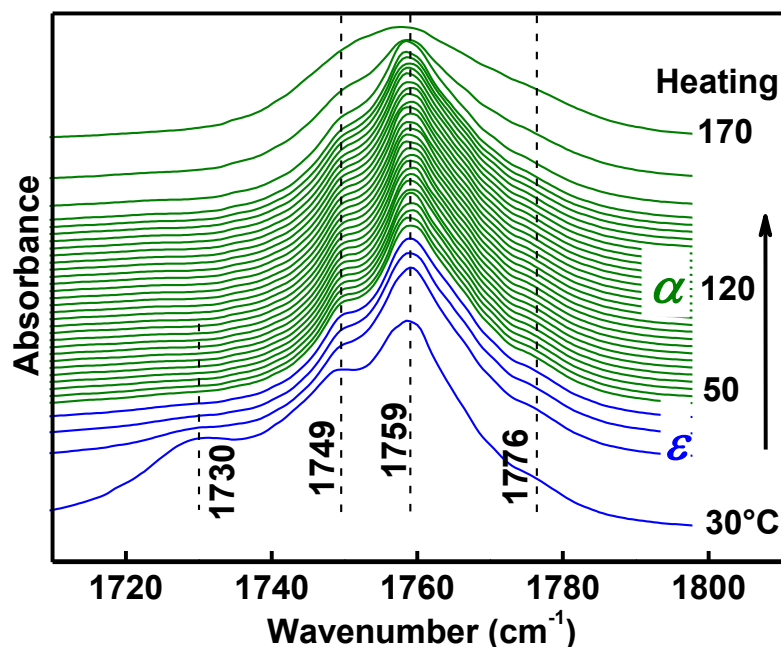


**Figure 3.8.** (a) Temperature-dependent infrared spectra of PLLA/CPO cocrystal measured during heating process from 30 to 170 °C in the frequency region of 1710–1800  $\text{cm}^{-1}$ .

Figure 3.8 shows the temperature-dependent IR spectra in the frequency region 1700–1800  $\text{cm}^{-1}$  collected in the heating process of PLLA/CPO cocrystal. No differences were observed up to the melting of PLLA other than the disappearance of the solvent band (1730  $\text{cm}^{-1}$ ) at 45 °C. It means the interaction between the carbonyl peak of PLLA and the solvent molecules is almost negligible. In this way, the infrared spectra were very useful to understand the solvent desorption and the  $\epsilon$  to  $\alpha$  transition in PLLA-solvent complexes.

### 3.4.5. Solvent Distribution by SANS

Figure 3.9 shows the SANS patterns of the PLLA/CPO complex at three different levels (100, 50 and 25%) of deuterated CPO (dCPO). The lamellar peak decreases in intensity as the dCPO concentration is reduced and disappears at 25% dCPO. This can be interpreted as follows.<sup>70</sup> When lamellae are present, the inherent contrast due to the higher density of the crystalline lamellae is sufficient to give rise to SANS peak. When dCPO is present, the difference in the amount of dCPO in the crystalline and the amorphous interlamellar regions alters this contrast. Since PLLA was immersed in dCPO for six months, CPO was incorporated into both amorphous and crystalline regions. The strong peak at 100% dCPO suggests that the amount of dCPO in the amorphous regions is much greater than in the crystalline regions.

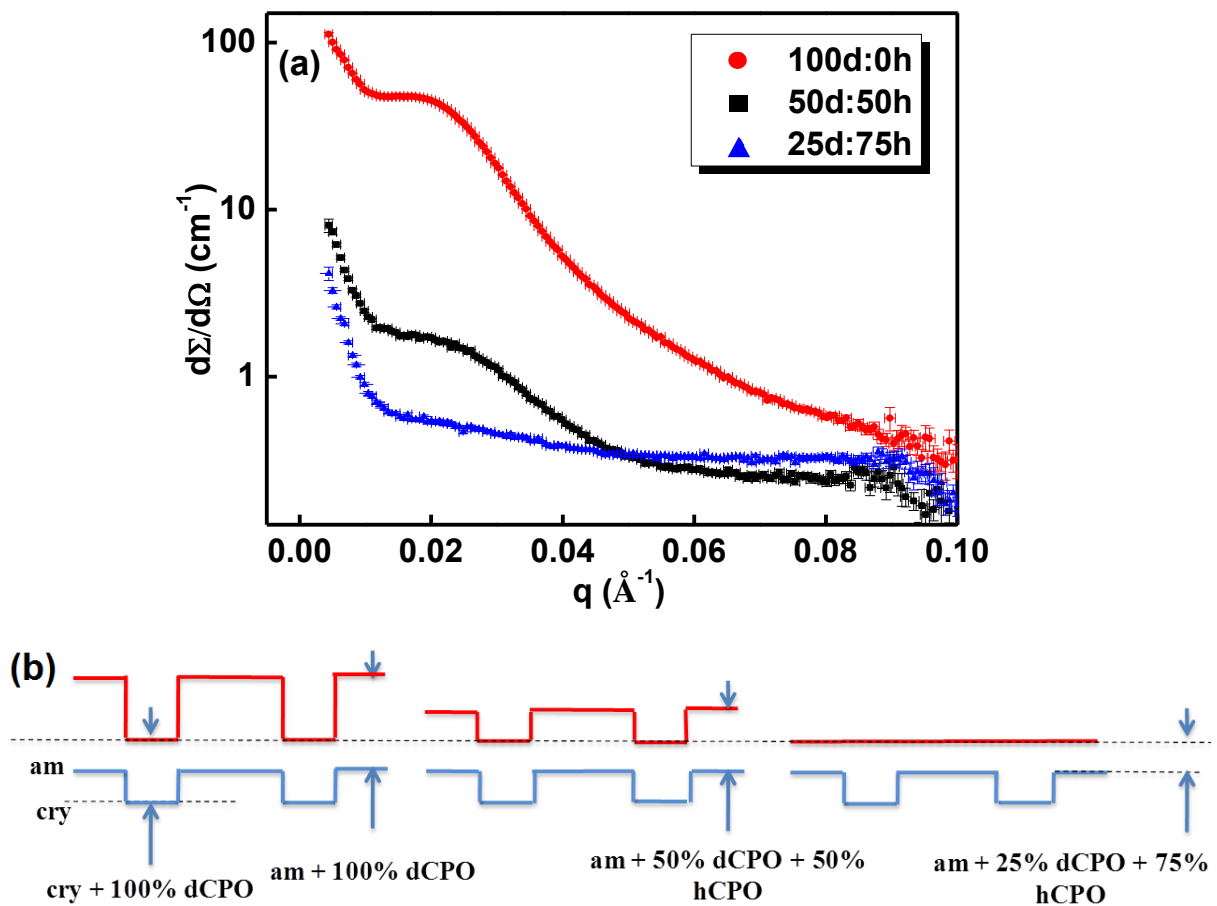


**Figure 3.9.** (a) SANS patterns of the PLLA/CPO complex at three different levels of deuterated CPO (100, 50 and 25%). (b) Changes in the SANS contrast due to the presence of dCPO (top figures) indicated by the changes from the contrast when there is no CPO present (bottom figures).

It is likely CPO is present as clusters in the amorphous domains, as indicated by the presence of diffuse scattering in the WAXS patterns. As the % dCPO is reduced, this contrast decreases, and correspondingly lamellar peak is weaker. At 25% dCPO, the scattering length density in the amorphous regions is equivalent to that of the 100% dCPO in the crystalline regions. Therefore, there is no lamellar scattering. Thus, SANS data suggests that CPO is present as clusters in the amorphous regions and is incorporated stoichiometrically in the crystalline regions. Rizzo et al. showed that 16 CPO guest molecules are packed within the crystal lattice of PLLA/CPO cocrystal.<sup>48</sup>

#### **3.4.6. Lamellar Morphology Changes during Heating by *in-situ* SAXS.**

To understand the intimate connection between the changes in crystal structure and stacked lamellar structure during the  $\varepsilon$  to  $\alpha$  transition, temperature-dependent SAXS measurements were carried out in the heating process of PLLA/CPO cocrystal. Figure 3.10 shows the 2D SAXS patterns at different temperatures starting from the PLLA/CPO cocrystal in the heating process. The 2D SAXS patterns were azimuthally averaged to give 1D scans and are shown in Figure 3.11a. A careful observation of the SAXS patterns indicate the drastic changes in the full width at half maximum, SAXS intensity and position of the scattering peak with the increase in temperature. The SAXS pattern at 0 °C shows overlapping features. This pattern changes to a two-point pattern and the intensity increases above 40 °C as the structure changes from  $\varepsilon$  to  $\alpha$ . At the same time, the peak position is also shifted to lower  $q$  indicating the increase in the long period. The SAXS pattern observed at 0 °C is due to the PLLA/CPO cocrystals. It is worth mentioning here that the SAXS pattern of sPS cocrystals show a typical two-point SAXS pattern at room temperature and no diffuse scattering was observed in WAXS patterns due to the presence of solvent molecules. On the other hand, in the emptied  $\delta$  ( $\delta_e$ ) form, the two-point scattering pattern was completely masked by strong diffused scattering arising from the empty cavities in the crystal lattice due to the removal of solvent molecules.<sup>59</sup>

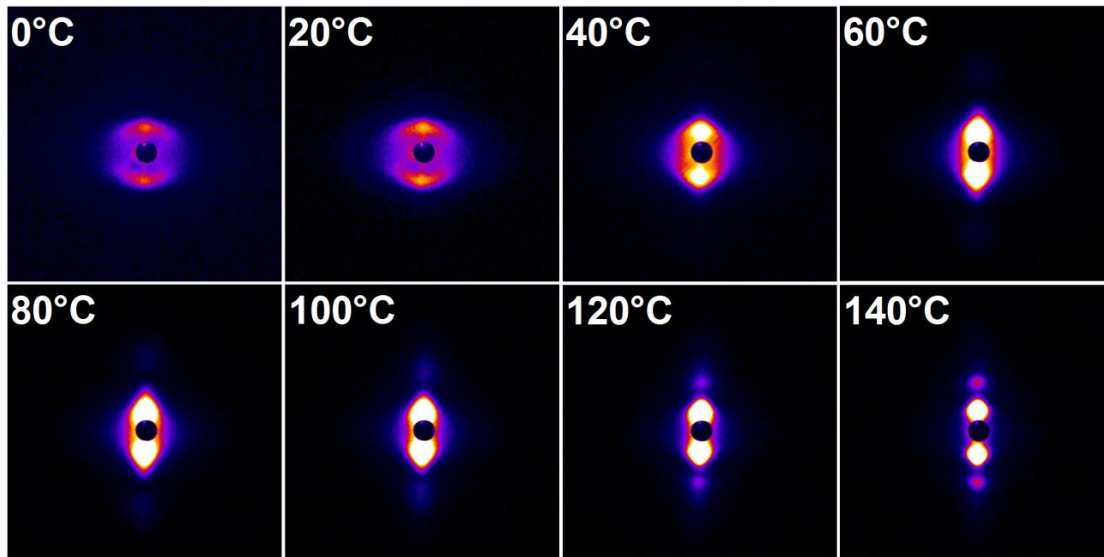


**Figure 3.10.** Two-dimensional SAXS patterns obtained at different temperatures during the heating process for the uniaxially drawn PLLA/CPO cocrystal.

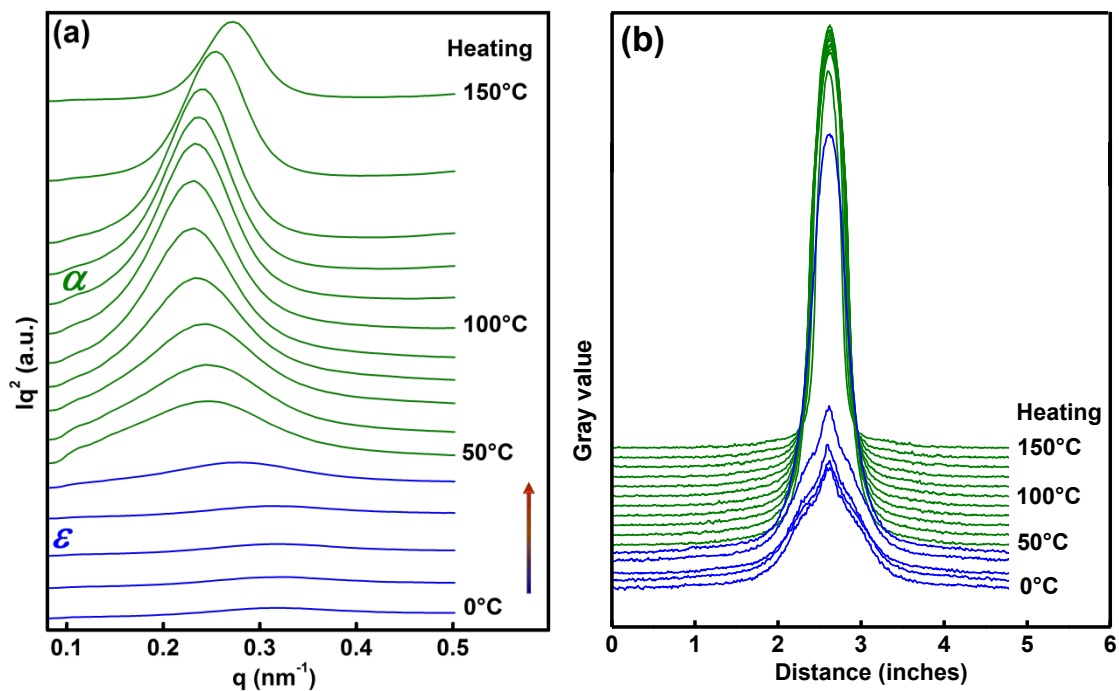


**Figure 3.11.** (a) Temperature dependence of SAXS patterns (Lorentz-corrected) (b) Temperature-dependent azimuthal scans through the reflections extracted from Figure 3.10.

In order to estimate the lamellar structure parameters, SAXS data were analyzed by calculating the 1D electron density correlation function curves.<sup>55, 59</sup> The calculated 1D electron density correlation function ( $K(z)$ ) curves at various temperatures in the heating process are shown in Figure 3.12.

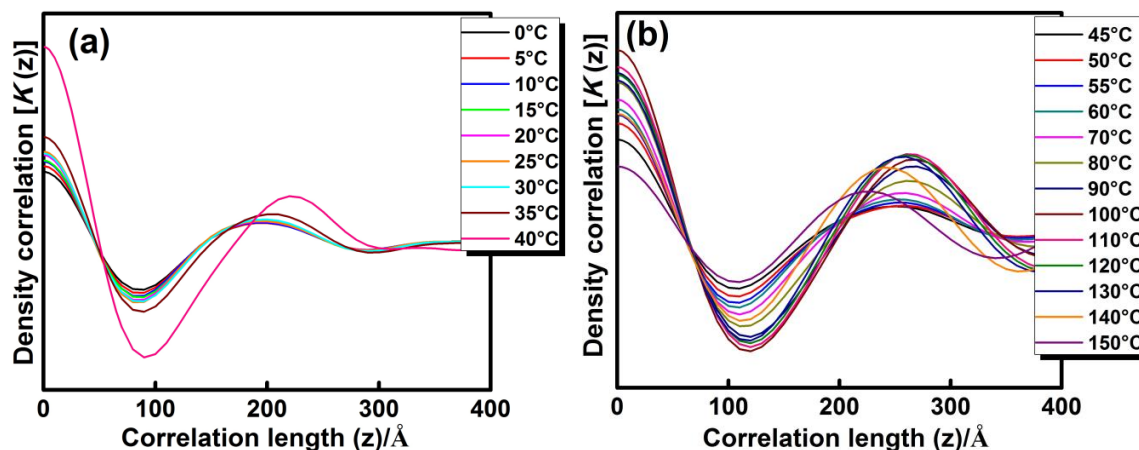


**Figure 3.12.** 1D electron density correlation function calculated based on the SAXS data shown in Figure 3.11. (a) 0–40 °C and (b) 45–150 °C.

The temperature-dependent long period ( $L$ ), lamellar thickness ( $l_c$ ) and amorphous thickness ( $l_a$ ) are displayed in Figure 3.13a. The values of  $L$ ,  $l_c$ , and  $l_a$  remain unchanged up to 40 °C and then abruptly increased in the temperature range 40 to 55 °C. For example, the  $l_c$  value increased from 70 to 85 Å (21% increase) when the temperature increased from 40 to 55 °C, whereas the  $l_a$  increased from 132 to 172 Å (30% increase) in this temperature range. These results suggest that the % increase in the thickness of the amorphous layer is more than that of the crystalline layer. In the same temperature range, the WAXS, DSC, and IR data revealed that the crystalline phase undergoes a structural phase transition from the  $\varepsilon$  to  $\alpha$  transition. At this transition, the CPO molecules residing in the crystalline phase diffuse into the amorphous phase. We speculate here that the solvent molecules that are residing in the amorphous phase also contribute to the increase in the long period and amorphous thickness. On further heating, the slight increase in the  $l_a$  values were observed in the temperature range of 60–90 °C and then the  $l_a$  values decreased in a broad temperature range 100–150 °C. The decrease in  $l_a$  values could be due to the evaporation of CPO molecules in the amorphous phase and the concomitant crystallization of a fraction of the amorphous PLLA segments at high temperature into the stable  $\alpha$  form. The later process also accounts for the increase in  $l_c$  from 85 to 95 Å in the temperature range of 60–110 °C, which then remains the same until melting.

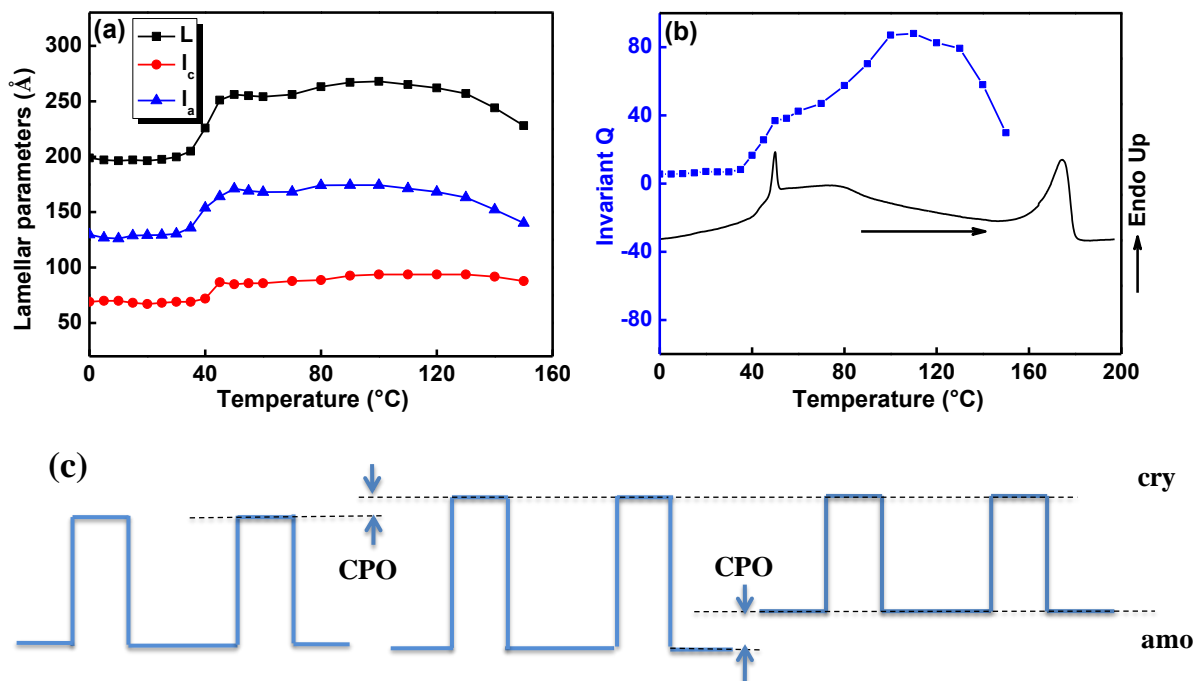


**Figure 3.13.** (a) Long period ( $L$ ), lamellar thickness ( $l_c$ ), and amorphous thickness ( $l_a$ ) of PLLA/CPO cocrystal obtained at different temperatures during the heating process (b) change in SAXS invariant ( $Q$ ) of PLLA/CPO cocrystal obtained at different temperatures during the heating process. DSC thermogram of PLLA/CPO cocrystal measured in the heating process is included for the purpose of comparison (c) changes in the SAXS contrast due to changes in the CPO content in the crystalline and the amorphous regions.

The change in  $Q$  values was plotted against the temperature in Figure 3.13b. The DSC thermogram of PLLA/CPO cocrystals is shown in the heating process for the purpose of comparison. The changes in the SAXS intensity (the invariant, Figure 3.13b) can be explained by both the density difference between the crystalline and the amorphous domains, and to the excess CPO in the amorphous regions (Figure 3.13c). At 40 °C, as the CPO from the crystalline regions is expelled, the electron density increases in the crystalline regions. At the same time, the volume fraction of the lamellar stacks increased in this temperature range. This increases the contrast and accounts for the large increase in  $Q$  between 40–100 °C after the  $\varepsilon$  to  $\alpha$  transition. Above 100 °C, as the solvent in the amorphous regions also evaporates, it increases the density of the amorphous regions, thus reducing the contrast and hence the scattered intensity and  $Q$ .

There is one other interesting feature in the SAXS pattern, which is the appearance of the banana-shaped pattern at 0 and 20 °C (Figure 3.10). Azimuthal

scans through the reflections indicate two components in the low-temperature scans (Figure 3.11b). One is the central peak with a high degree of orientation in the 2D patterns, and the other corresponding to the halo with the low degree of orientation. This has been observed before in polymers with folded chains lamellae.<sup>71, 72</sup> By comparing with the degree of orientation of the SAXS reflection and the WAXS crystalline peaks (Figures 3.4, 3.10 and 3.14), the sharp peak can be attributed to the crystalline lamellae with the lamellar surface perpendicular to the chain axis. This component is weak at low temperatures, increases in intensity with temperature, and is the only feature at  $T \geq 40$  °C. The broad SAXS component remains essentially unchanged up to 40 °C and disappears at 40 °C. We attribute this feature to the tilted lamellae. When the solvent is present, the polymer chains are relaxed, occupy a larger interface area, and this causes lamellae to tilt. As the solvent is removed from the crystalline lamellae and from the surface of the lamellae, the chains are no longer relaxed. This change results in the amorphous chain segments being in line with the crystalline segments. The interface area decreases. As a result, the lamellar surface becomes perpendicular to the chain axis. Tilted lamellae give rise to a four-point pattern that appears to be banana shaped because of the inherent disorder. This becomes a two-point pattern when the lamellae are perpendicular to the chain axis.

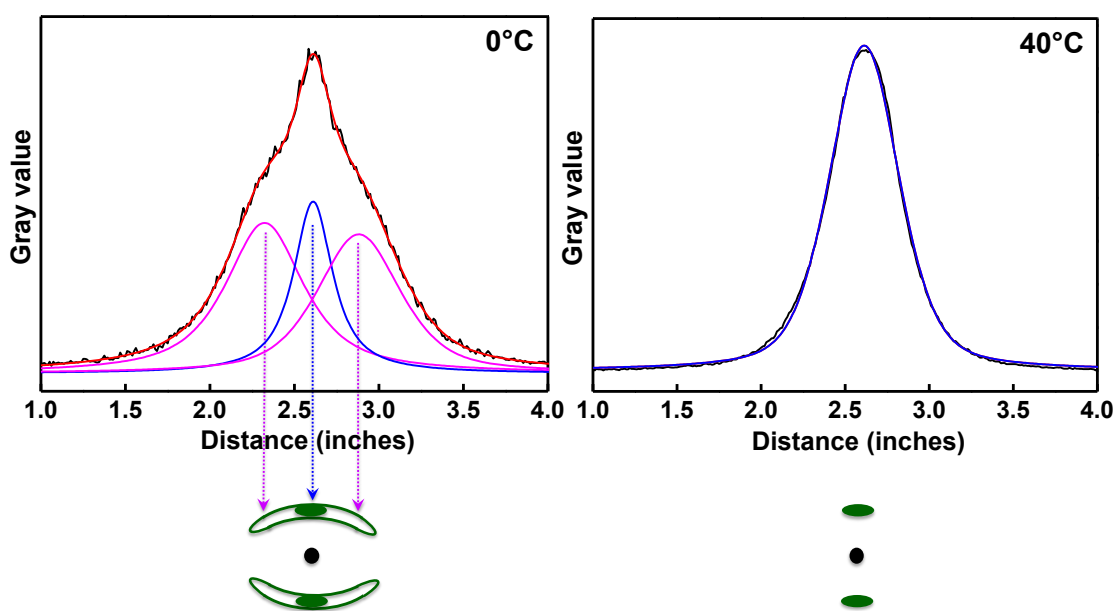
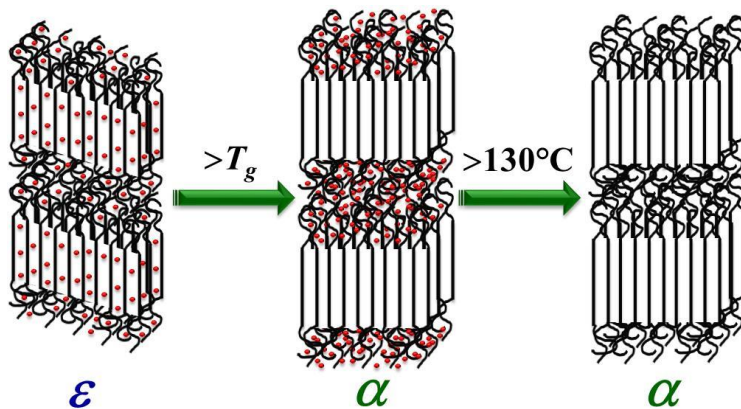


Figure 3.14. Azimuthal scans through the reflections of SAXS patterns collected at 0 °C and 40 °C.

The change in the tilt of the lamellae also causes shear or the sliding of the crystalline stems as the crystalline transformation occurs from the  $\varepsilon$  to the  $\alpha$  form. Thus, removal of solvent in the PLLA/CPO cocrystals brings about  $\varepsilon$  to  $\alpha$  crystalline transformation that is accompanied by the shear of the crystalline stems within the lamellae.



**Figure 3.15.** Schematic illustration of structural changes of PLLA/CPO cocrystal obtained at different temperatures during the heating process.

Based on the WAXS/SAXS, infrared spectroscopy, and DSC results, the structural changes occur during heating of the PLLA/CPO cocrystal can be explained schematically as shown in Figure 3.15. In the starting  $\varepsilon$  form, most of the solvent molecules are packed within the crystal lattice of PLLA. On heating, the  $\varepsilon$  form changed to the  $\alpha$  form by the expulsion of solvent molecules into the amorphous phase of PLLA by retaining the helical conformation. During this transition, the stacked lamellar structure stays intact. The thickness of the amorphous phase increased drastically after the  $\varepsilon$  to  $\alpha$  transition due to the presence of solvent molecules. As the temperature increases, the solvent molecules, which are residing in the amorphous phase of the  $\alpha$  form, activate the thermal motion of molecular chains (at high temperature) and as a result, some of the amorphous phase crystallizes into the  $\alpha$  form. When the temperature reaches the boiling point of the solvent, the solvent molecules evaporate from the amorphous phase resulting in the shrinkage of the amorphous layer. In this way, the structural changes in the PLLA/CPO cocrystals are intimately related to the

changes in the lamellar stacking while retaining the helical chain conformation during the  $\varepsilon$  to  $\alpha$  transition.

### 3.5. Conclusions

SANS results suggest that CPO is stoichiometrically incorporated into the crystal lattice of the  $\varepsilon$  form, but is present as clusters in the amorphous phase. Data at three different length scales from different techniques revealed the intimate connection between the crystal structure and the lamellar structure during the  $\varepsilon$  to  $\alpha$  transition in PLLA/CPO cocrystals. DSC and WAXS data show that just above the  $T_g$  of PLLA, in the temperature range of 40–55 °C, the  $\varepsilon$  form of the PLLA/CPO cocrystals transforms to the  $\alpha$  form. FTIR data revealed that the chain conformation is preserved during  $\varepsilon$  to  $\alpha$  transition. SAXS data show that this transformation occurs as the solvent molecules residing in the crystal lattice migrate into the amorphous phase, and the tilted lamellae of the  $\varepsilon$  form become untilted in the  $\alpha$  form. Large-scale reorganization was observed in the lamellar structure during the  $\varepsilon$  to  $\alpha$  transition as indicated by the changes in the lamellar parameters (long period, lamellar thickness, amorphous thickness and invariant). Upon further heating, in the temperature range of 100–130 °C, as the CPO is evaporated from the polymer, the amorphous phase crystallizes into the  $\alpha$  form. It was also observed that the polymer chain orientation was preserved during the entire desorption process.

### 3.6. References

- (1) Auras, R. L., L.-T.; Selke, S. E. M.; Tsuji, H. , Poly(lactic acid): Synthesis, Structures, Properties, Processing, and Applications. John Wiley & Sons: Hoboken, NJ: 2010.
- (2) Lasprilla, A. J. R.; Martinez, G. A. R.; Lunelli, B. H.; Jardini, A. L.; Filho, R. M. *Biotechnology Advances* **2012**, *30*, 321-328.
- (3) Ma, Z.; Gao, C.; Gong, Y.; Shen, J. *Biomaterials* **2005**, *26*, 1253-1259.
- (4) Hoogsteen, W.; Postema, A. R.; Pennings, A. J.; Ten Brinke, G.; Zugenmaier, P. *Macromolecules* **1990**, *23*, 634-642.

- 
- (5) Sasaki, S.; Asakura, T. *Macromolecules* **2003**, *36*, 8385-8390.
  - (6) Wasanasuk, K.; Tashiro, K.; Hanesaka, M.; Ohhara, T.; Kurihara, K.; Kuroki, R.; Tamada, T.; Ozeki, T.; Kanamoto, T. *Macromolecules* **2011**, *44*, 6441-6452.
  - (7) Zhang, J.; Tashiro, K.; Tsuji, H.; Domb, A. J. *Macromolecules* **2008**, *41*, 1352-1357.
  - (8) Zhang, J.; Duan, Y.; Sato, H.; Tsuji, H.; Noda, I.; Yan, S.; Ozaki, Y. *Macromolecules* **2005**, *38*, 8012-8021.
  - (9) Pan, P.; Kai, W.; Zhu, B.; Dong, T.; Inoue, Y. *Macromolecules* **2007**, *40*, 6898-6905.
  - (10) Kawai, T.; Rahman, N.; Matsuba, G.; Nishida, K.; Kanaya, T.; Nakano, M.; Okamoto, H.; Kawada, J.; Usuki, A.; Honma, N.; Nakajima, K.; Matsuda, M. *Macromolecules* **2007**, *40*, 9463-9469.
  - (11) Wasanasuk, K.; Tashiro, K. *Polymer* **2011**, *52*, 6097-6109.
  - (12) Marubayashi, H.; Akaishi, S.; Akasaka, S.; Asai, S.; Sumita, M. *Macromolecules* **2008**, *41*, 9192-9203.
  - (13) Marubayashi, H.; Asai, S.; Sumita, M. *Polymer* **2012**, *53*, 4262-4271.
  - (14) Puiggali, J.; Ikada, Y.; Tsuji, H.; Cartier, L.; Okihara, T.; Lotz, B. *Polymer* **2000**, *41*, 8921-8930.
  - (15) Eling, B.; Gogolewski, S.; Pennings, A. J. *Polymer* **1982**, *23*, 1587-1593.
  - (16) Sawai, D.; Takahashi, K.; Sasashige, A.; Kanamoto, T.; Hyon, S.-H. *Macromolecules* **2003**, *36*, 3601-3605.
  - (17) Cartier, L.; Okihara, T.; Ikada, Y.; Tsuji, H.; Puiggali, J.; Lotz, B. *Polymer* **2000**, *41*, 8909-8919.
  - (18) Marubayashi, H.; Asai, S.; Sumita, M. *Macromolecules* **2012**, *45*, 1384-1397.
  - (19) Marubayashi, H.; Asai, S.; Sumita, M. *J. Phys. Chem. B* **2013**, *117*, 385-397.
  - (20) Kobayashi, J.; Asahi, T.; Ichiki, M.; Oikawa, A.; Suzuki, H.; Watanabe, T.; Fukada, E.; Shikinami, Y. *J. Appl. Phys.* **1995**, *77*, 2957-2973.
  - (21) Cho, T.-Y.; Strobl, G. *Polymer* **2006**, *47*, 1036-1043.
  - (22) Ikada, Y.; Jamshidi, K.; Tsuji, H.; Hyon, S. H. *Macromolecules* **1987**, *20*, 904-906.
  - (23) Tsuji, H.; Hyon, S. H.; Ikada, Y. *Macromolecules* **1991**, *24*, 5651-5656.
  - (24) Tsuji, H.; Ikada, Y. *Macromolecules* **1993**, *26*, 6918-6926.

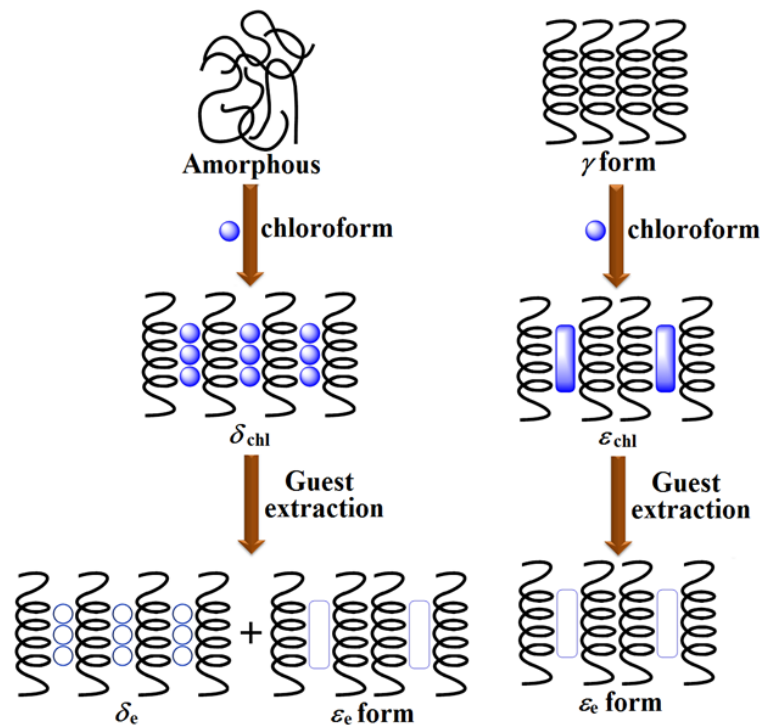
- 
- (25) Hu, X.; An, H.; Li, Z.-M.; Geng, Y.; Li, L.; Yang, C. *Macromolecules* **2009**, *42*, 3215-3218.
- (26) Xu, J.-Z.; Chen, T.; Yang, C.-L.; Li, Z.-M.; Mao, Y.-M.; Zeng, B.-Q.; Hsiao, B. S. *Macromolecules* **2010**, *43*, 5000-5008.
- (27) Sakai, F.; Nishikawa, K.; Inoue, Y.; Yazawa, K. *Macromolecules* **2009**, *42*, 8335-8342.
- (28) Stoclet, G.; Seguela, R.; Lefebvre, J. M. *Polymer* **2011**, *52*, 1417-1425.
- (29) Qiu, Z.; Li, Z. *Ind. Eng. Chem. Res.* **2011**, *50*, 12299-12303.
- (30) Pan, P.; Shan, G.; Bao, Y. *Ind. Eng. Chem. Res.* **2014**, *53*, 3148-3156.
- (31) Naga, N.; Yoshida, Y.; Inui, M.; Noguchi, K.; Murase, S. *J. Appl. Polym. Sci.* **2011**, *119*, 2058-2064.
- (32) Wu, N.; Lang, S.; Zhang, H.; Ding, M.; Zhang, J. *J. Phys. Chem. B* **2014**, *118*, 12652-12659.
- (33) Gowd, E. B.; Tashiro, K.; Ramesh, C. *Prog. Polym. Sci.* **2009**, *34*, 280-315.
- (34) Tashiro, K.; Ueno, Y.; Yoshioka, A.; Kobayashi, M. *Macromolecules* **2001**, *34*, 310-315.
- (35) Hashida, T.; Tashiro, K.; Aoshima, S.; Inaki, Y. *Macromolecules* **2002**, *35*, 4330-4336.
- (36) Vittoria, V.; Russo, R.; de Candia, F. *Polymer* **1991**, *32*, 3371-3375.
- (37) Milano, G.; Guerra, G. *Prog. Mater. Sci.* **2009**, *54*, 68-88.
- (38) Chatani, Y.; Shimane, Y.; Inoue, Y.; Inagaki, T.; Ishioka, T.; Ijitsu, T.; Yukinari, T. *Polymer* **1992**, *33*, 488-492.
- (39) Chatani, Y.; Shimane, Y.; Inagaki, T.; Ijitsu, T.; Yukinari, T.; Shikuma, H. *Polymer* **1993**, *34*, 1620-1624.
- (40) Petraccone, V.; Ruiz de Ballesteros, O.; Tarallo, O.; Rizzo, P.; Guerra, G. *Chem. Mater.* **2008**, *20*, 3663-3668.
- (41) Yoshioka, A.; Tashiro, K. *Macromolecules* **2004**, *37*, 467-472.
- (42) Gowd, E. B.; Shibayama, N.; Tashiro, K. *Macromolecules* **2007**, *40*, 6291-6295.
- (43) Choi, Y.-S.; Miyasaka, K. *J. Appl. Polym. Sci.* **1993**, *48*, 313-317.
- (44) Choi, Y.-S.; Miyasaka, K. *J. Appl. Polym. Sci.* **1994**, *51*, 613-618.
- (45) Tashiro, K.; Kitai, H.; Saharin, S. M.; Shimazu, A.; Itou, T. *Macromolecules* **2015**, *48*, 2138-2148.

- 
- (46) Chatani, Y.; Tadokoro, H.; Saegusa, T.; Ikeda, H. *Macromolecules* **1981**, *14*, 315-321.
- (47) Chatani, Y.; Kobatake, T.; Tadokoro, H. *Macromolecules* **1983**, *16*, 199-204.
- (48) Rizzo, P.; Ianniello, G.; Venditto, V.; Tarallo, O.; Guerra, G. *Macromolecules* **2015**, *48*, 7513-7520.
- (49) Matsuda, Y.; Fukatsu, A.; Wang, Y.; Miyamoto, K.; Mays, J. W.; Tasaka, S. *Polymer* **2014**, *55*, 4369-4378.
- (50) Matsuda, Y.; Fukatsu, A.; Tasaka, S. *Chem. Lett.* **2013**, *42*, 1046-1047.
- (51) Zhao, J. K.; Gao, C. Y.; Liu, D. *J. Appl. Crystallogr.* **2010**, *43*, 1068-1077.
- (52) Arnold, O.; Bilheux, J. C.; Borreguero, J. M.; Buts, A.; Campbell, S. I.; Chapon, L.; Doucet, M.; Draper, N.; Ferraz Leal, R.; Gigg, M. A.; Lynch, V. E.; Markvardsen, A.; Mikkelsen, D. J.; Mikkelsen, R. L.; Miller, R.; Palmen, K.; Parker, P.; Passos, G.; Perring, T. G.; Peterson, P. F.; Ren, S.; Reuter, M. A.; Savici, A. T.; Taylor, J. W.; Taylor, R. J.; Tolchenov, R.; Zhou, W.; Zikovskiy, J. *Nuclear Instruments and Methods in Physics Research Section A: Accelerators, Spectrometers, Detectors and Associated Equipment* **2014**, *764*, 156-166.
- (53) Wignall, G. D.; Bates, F. S. *J. Appl. Crystallogr.* **1987**, *20*, 28-40.
- (54) Nagarajan, S.; Gowd, E. B. *Macromolecules* **2015**, *48*, 5367-5377.
- (55) Strobl, G. R.; Schneider, M. *J. Polym. Sc., Polym. Phys. Ed.* **1980**, *18*, 1343-1359.
- (56) Krueger, K. N.; Zachmann, H. G. *Macromolecules* **1993**, *26*, 5202-5208.
- (57) Albulnia, A. R.; Di Masi, S.; Rizzo, P.; Milano, G.; Musto, P.; Guerra, G. *Macromolecules* **2003**, *36*, 8695-8703.
- (58) Gowd, E. B.; Tashiro, K.; Ramesh, C. *Macromolecules* **2008**, *41*, 9814-9818.
- (59) Gowd, E. B.; Shibayama, N.; Tashiro, K. *Macromolecules* **2008**, *41*, 2541-2547.
- (60) Gowd, E. B.; Shibayama, N.; Tashiro, K. *Macromolecules* **2006**, *39*, 8412-8418.
- (61) Gowd, E. B.; Tashiro, K. *Macromolecules* **2007**, *40*, 5366-5371.
- (62) Manfredi, C.; De Rosa, C.; Guerra, G.; Rapacciuolo, M.; Auriemma, F.; Corradini, P. *Macromol. Chem. Phys.* **1995**, *196*, 2795-2808.
- (63) Gowd, E. B.; Nair, S. S.; Ramesh, C. *Macromolecules* **2002**, *35*, 8509-8514.
- (64) Rizzo, P.; D'Aniello, C.; De Girolamo Del Mauro, A.; Guerra, G. *Macromolecules* **2007**, *40*, 9470-9474.
- (65) Meaurio, E.; Zuza, E.; López-Rodríguez, N.; Sarasua, J. R. *J. Phys. Chem. B* **2006**, *110*, 5790-5800.

- 
- (66) Pan, P.; Yang, J.; Shan, G.; Bao, Y.; Weng, Z.; Cao, A.; Yazawa, K.; Inoue, Y. *Macromolecules* **2012**, *45*, 189-197.
- (67) Cataliotti, R.; Paliani, G. *Chem. Phys. Lett.* **1973**, *20*, 280-283.
- (68) Meaurio, E.; Martinez de Arenaza, I.; Lizundia, E.; Sarasua, J. R. *Macromolecules* **2009**, *42*, 5717-5727.
- (69) Pan, P.; Han, L.; Shan, G.; Bao, Y. *Macromolecules* **2014**, *47*, 8126-8130.
- (70) Murthy, N. S.; Akkapeddi, M. K.; Orts, W. J. *Macromolecules* **1998**, *31*, 142-152.
- (71) Murthy, N. S.; Grubb, D. T. *J. Polym. Sci., Part B: Polym. Phys.* **2003**, *41*, 1538-1553.
- (72) Murthy, N. S.; Grubb, D. T. *J. Polym. Sci., Part B: Polym. Phys.* **2002**, *40*, 691-705.



## Syndiotactic Polystyrene (sPS) Cocrytals: Structural Phase Transitions of sPS upon the Guest Exchange and Guest Extraction Processes



### 4.1. Abstract

*The host preparation method as well as the nature of guest molecules used for the preparation of cocrytals has a strong influence on the structural phase transitions of syndiotactic polystyrene (sPS) upon guest exchange and guest extraction processes. In order to investigate this, sPS with different initial morphologies like amorphous,  $\alpha$  and  $\gamma$  forms were used for preparing cocrytals with chloroform and toluene. Such obtained cocrytals were further utilized for the guest exchange process with a series of *n*-alkanes. When the guest exchange was performed with *n*-alkanes, toluene treated amorphous and  $\alpha$  form samples (i.e. monoclinic  $\delta$  cocrystal) transformed into the triclinic  $\delta$  cocrystal irrespective of the starting morphology. However, the toluene treated  $\gamma$  form transformed back to*

- ❖ R.C. Jose, P. Shaiju, B. Nagendra, E. Bhoje Gowd\*, *Polymer* 2013, 54, 6617-6627.
- ❖ P. Shaiju and E. Bhoje Gowd\*, *Polymer* 2015, 56, 581-589.
- ❖ P. Shaiju and E. Bhoje Gowd\*, *Macromolecular Symposia*, 2016, 359, 104-110.

*the  $\gamma$  form in presence of n-alkanes. On the other hand, chloroform treated amorphous sample (i.e. monoclinic  $\delta$  cocrystal) converted into a mixture of  $\delta$  cocrystal and  $\varepsilon$  cocrystal, while chloroform treated  $\alpha$  and  $\gamma$  forms transformed into triclinic  $\delta$  cocrystal and  $\varepsilon$  cocrystal, respectively. To explore the structural changes of sPS upon the guest extraction process, chloroform treated amorphous and  $\gamma$  form films were used as the starting materials. Selective extraction of guest molecules resulted in the complex phase transitions of the host structure. In the case of chloroform treated amorphous samples, the structure transformed to a mixture of nanoporous  $\delta$  ( $\delta_e$ ) and  $\varepsilon$  ( $\varepsilon_e$ ) forms after the solvent extraction. On the other hand, the guest extraction from chloroform treated  $\gamma$  form samples resulted in the formation of nanoporous  $\varepsilon$  ( $\varepsilon_e$ ) form with channel-shaped cavities.*

## 4.2. Introduction

Polymorphism exhibited by sPS has been extensively studied using X-ray diffraction, electron diffraction, Fourier transform infrared spectroscopy and solid-state NMR.<sup>1-17</sup> sPS crystallizes as  $\alpha$  and  $\beta$  forms with all-trans planar zigzag ( $T_4$ ) conformation by melt processing or by thermal treatments on the glassy samples.<sup>1-3, 12, 18-22</sup> In addition to these crystalline forms, sPS also crystallizes as  $\gamma$ ,  $\delta$  and  $\varepsilon$  forms with helical  $s(2/1)2$  conformation  $[-(T_2G_2)_2-]$  by solvent swelling of glassy or semicrystalline samples.<sup>3-9, 13-15, 23-25</sup>  $\delta$  and  $\varepsilon$  forms are termed as cocrystals due to the presence of solvent molecules within their crystal lattice. On the other hand,  $\gamma$  form is solvent-free, even though the conformation is similar to that of  $\delta$  and  $\varepsilon$  cocrystals.<sup>26</sup> Nanoporous  $\delta$  ( $\delta_e$ ) and  $\varepsilon$  ( $\varepsilon_e$ ) forms are also obtained via suitable guest extraction procedures from the cocrystals. The packing of these nanoporous crystalline phases is distinct; the empty pores occupied by solvent molecules, are distributed as cavities and channels, respectively.<sup>27-30</sup>

The studies on the guest exchange phenomena using sPS cocrystals are prolific since this process is a simple route for the preparation of the composite materials in molecular level with a range of functional molecules.<sup>14, 31-38</sup> Many authors including some of us explored the utility of guest exchange process for

incorporating a variety of guest molecules into the cavity of sPS.<sup>14, 37-44</sup> In particular, guest exchange process with *n*-alkanes is interesting from the structural perspective of both in terms of host and guest.<sup>31, 35-38</sup> For example, in the year 2011, three papers appeared in the literature on the structural characterization of sPS-*n*-alkane complexes where both  $\delta$  *clathrates* and  $\epsilon$  *clathrates* were used for the guest exchange process with a series of *n*-alkanes.<sup>36-38</sup> Gowd et al., reported that when the sPS/chloroform  $\delta$  *clathrate* sample is used for the guest exchange process with longer *n*-alkanes (above *n*-octane), traces  $\epsilon$  cocrystal is observed along with the  $\delta$  *clathrate*.<sup>36</sup> On the other hand, Tarallo et al., used the same sPS/chloroform  $\delta$  *clathrate* as the starting sample and observed that the host structure completely transforms into the triclinic  $\delta$  *clathrates*, after guest exchange with longer *n*-alkanes (above *n*-octane).<sup>37</sup> It is also worth mentioning here that the same group used sPS/chloroform  $\epsilon$  *clathrates* for the guest exchange with a series of *n*-alkanes and found that the crystal packing of the  $\epsilon$  *clathrates* remain unaltered independent of the chain-length of the *n*-alkane.<sup>38</sup> In this way, the observations made so far on the structures sPS/*n*-alkane complexes are inconclusive and hence necessitates a thorough and systematic investigation of the structure-controlling factors upon guest exchange process.

Herein we have carried out a systematic investigation of the effect of the host structure and different guest molecules used, on the structural changes of sPS upon the guest exchange and guest extraction processes. For current studies we used both undrawn and uniaxially drawn samples; the structural variations were analyzed using WAXS and FTIR techniques. It should be emphasized here that for the first time we have utilized sPS/toluene  $\delta$  *clathrate* samples for the detailed investigation of the structural changes upon the guest exchange. The *n*-alkanes (ranging from *n*-octane to *n*-decane) used in this study were selected in such a way that their molecular volume should be higher than that of the cavity of the  $\delta_e$  form.

### 4.3. Experimental

**4.3.1. Materials:** sPS pellets ( $M_w \sim 272000$ ,  $D \sim 2.28$ ) used in this study were kindly supplied by Idemitsu Petrochemical Co., Ltd. *N*-alkanes were purchased from Alfa Aesar with a purity of 99%. Chloroform, toluene and acetone were supplied by SD Fine Chemicals Limited. Acetonitrile was purchased from Sisco Research Laboratories Pvt. Ltd. All these solvents were used without further purification.

#### 4.3.2. Sample Preparation

**Amorphous Samples:** The amorphous samples were prepared by quenching the melt into ice water. Both thinner (100  $\mu\text{m}$ ) and thicker samples (400  $\mu\text{m}$ ) were prepared for FTIR and X-ray diffraction measurements, respectively. Uniaxially drawn samples were prepared by stretching a small piece of rectangular shaped film by about 5 times of the original length, above a hot plate kept at 100 °C (glass transition temperature of sPS).

**$\alpha$  form:** Undrawn  $\alpha$  form samples were prepared by annealing the amorphous samples at 160 °C in a vacuum oven and uniaxially drawn  $\alpha$  form samples were prepared by annealing the stretched samples at 170 °C for 12 h by keeping the ends fixed.

**$\gamma$  form:** Undrawn  $\gamma$  form samples were prepared by dipping the amorphous samples in acetone for 3 days. Uniaxially drawn  $\gamma$  form samples have been obtained by annealing the uniaxially drawn  $\delta$  cocrystal samples at 145 °C for 1 hour.

Both undrawn and uniaxially drawn amorphous,  $\alpha$  form and  $\gamma$  form samples were dipped in toluene for 3 days and chloroform for 12 h at room temperature in order to obtain the sPS/toluene and sPS/chloroform cocrystals, respectively. The samples removed from solvents were kept at ambient temperature until they became dry. Guest exchange process was carried out by dipping sPS/toluene and sPS/chloroform samples in *n*-alkanes ranging from *n*-octane to *n*-decane for 32

days. Guest extraction was carried out by dipping the chloroform treated amorphous and  $\gamma$  form samples in acetonitrile for 12 h at room temperature.

### **4.3.3. Characterization**

**X-ray Diffraction:** The X-ray diffraction measurements of undrawn samples were performed using Rigaku Dmax 2500 diffractometer. The system consists of a rotating anode generator with a copper target and a wide-angle powder goniometer, having diffracted beam graphite monochromator. The generator was operated at 40 kV and 150 mA. All the experiments were performed in the reflection mode in the  $2\theta$  range of 4–35° at scanning rate of 2°/min. In the case of uniaxially drawn samples, the X-ray fiber diffractograms were recorded on a Rigaku Micromax 7 (rotating anode generator with micro focus geometry) X-ray system with a copper source and a flat image plate as the detector. The corresponding one-dimensional patterns were obtained from circular integration of the intensities of the 2D pattern.

Some of the WAXS measurements were performed using XEUSS SAXS/WAXS system by Xenocs. The source used in the instrument is Cu  $K\alpha$  with a wavelength,  $\lambda = 1.54 \text{ \AA}$ . The 2D images obtained from the Mar 345 detector were converted into 1D patterns using Fit2D software. The measurements were carried out in the transmission mode.

**FTIR:** Infrared spectra were measured with a Perkin-Elmer FTIR Spectrometer (model PC 16) at a resolution of  $2 \text{ cm}^{-1}$  in the range of 450–4400  $\text{cm}^{-1}$ . A total of 32 scans were used for signal averaging.

## **4.4. Results and Discussion**

### **4.4.1. Guest Exchange Process Using Toluene Treated Amorphous Samples**

Undrawn amorphous films were treated with toluene to obtain the sPS/toluene complex and the samples thus obtained were used for guest exchange process with a series of *n*-alkanes. Figure 4.1 shows the X-ray diffraction patterns of sPS/toluene complex together with the sPS/*n*-alkane complexes obtained upon guest exchange process. X-ray diffraction pattern of sPS/toluene complex shows

strong reflections at  $2\theta = 8.0, 10.3, 17.4, 20.1,$  and  $23.4^\circ$ , which are characteristic reflections of the monoclinic  $\delta$  cocrystal. Upon guest exchange with  $n$ -alkanes, a new X-ray pattern different from the monoclinic  $\delta$  cocrystal is observed. As the X-ray reflections in the  $2\theta \sim 5\text{--}15^\circ$  region are very weak, we further utilized the uniaxially drawn samples to understand the complicated phase transition behavior upon guest exchange process.

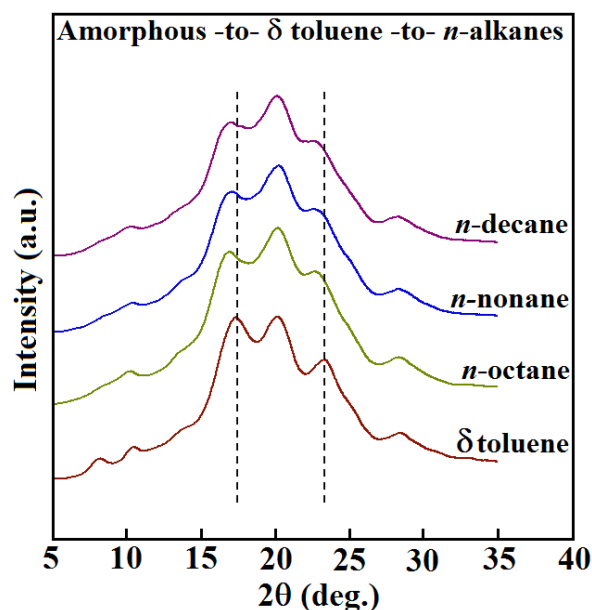


**Figure 4.1.** X-ray diffraction patterns of toluene treated amorphous films after dipping in  $n$ -alkanes for 32 days. Toluene treated amorphous sample is also shown for the purpose of comparison.

Figure 4.2 shows representative two-dimensional (2D) X-ray diffraction fiber patterns and one-dimensional (1D) X-ray diffraction patterns of  $\delta$  cocrystal of sPS/toluene complex together with  $n$ -octane and  $n$ -nonane treated  $\delta$  cocrystal. The  $n$ -decane treated samples are not included in the case of uniaxially drawn samples as the guest exchange process is not fully completed within 32 days. This observation clearly indicates that the chain orientation has a significant effect in controlling the diffusion behavior of  $n$ -alkanes in the oriented amorphous phase. X-ray diffraction pattern of the sPS/toluene complex shows reflections characteristic of the monoclinic  $\delta$  cocrystal ( $8.0, 10.3, 17.4, 20.1,$  and  $23.4^\circ$ ). As a consequence of  $n$ -alkanes treatment, positions and relative intensities of these reflections changed in the resultant diffraction pattern. It was also noticed that the

full width at half maximum (FWHM) of all the observed reflections increased, indicating the presence of some disorder upon guest exchange and the  $d_{010}$  spacing of the sPS/*n*-alkane complexes is lower than that of the starting sPS/toluene complex. Tarallo et al. reported a criterion to discriminate between the monoclinic and triclinic clathrates based on the  $d_{010}$  spacing.<sup>39</sup> The observed  $d_{010}$  spacing of sPS/*n*-alkane complexes ( $d_{010} = 1.06$  nm) is less than that of the empty ( $\delta_e$ ) form suggesting the phase transition from the monoclinic  $\delta$  cocrystal to the triclinic  $\delta$  cocrystal upon guest exchange with longer *n*-alkanes. It was already demonstrated that longer *n*-alkanes adopt bent conformations within the cavities of the triclinic  $\delta$ -clathrates. In the aforementioned complex close packing of polymer chains in the *ac* layers is partially disturbed and guest molecular planes lie inclined with respect to the helical chain axes.<sup>31, 35, 37</sup>

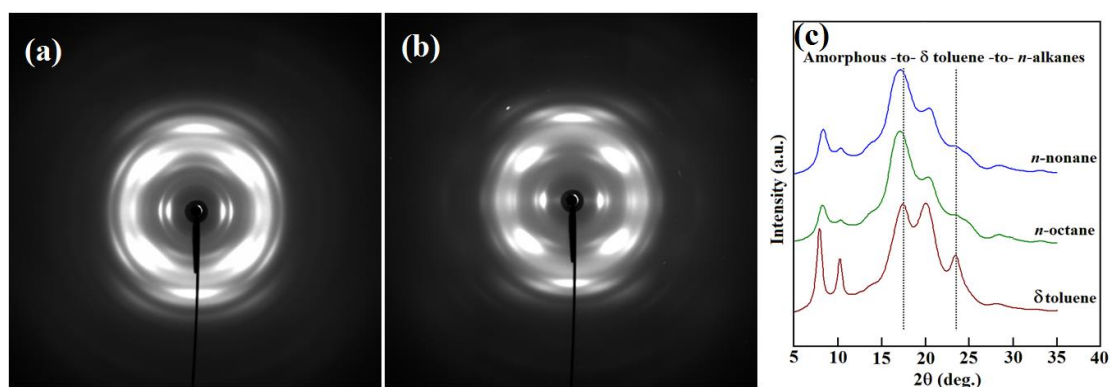


**Figure 4.2.** X-ray fiber diagrams of (a) toluene treated uniaxially drawn amorphous sample (b) *n*-nonane treated sPS/toluene complex for 32 days and (c) 1D intensity profiles of various samples (as indicated) by the circular integration of 2D diffraction patterns.

To know more about the structural changes on the guest exchange process, X-ray diffraction results are compared with the infrared spectral data. Figure 4.3 shows FTIR spectra of sPS/toluene complex (Figure 4.3a) along with the *n*-nonane treated  $\delta$  (toluene) sample (Figure 4.3b) in three different spectral regions. Complete disappearance of the toluene band at  $465\text{ cm}^{-1}$  (not shown in figure) and appearance of the *n*-nonane band at  $1466\text{ cm}^{-1}$  (scissoring of the C–H bonds in the methylene group) confirms the replacement of toluene by *n*-nonane. In the literature, it was shown that the infrared bands in the spectra regions  $590\text{--}620\text{ cm}^{-1}$

and  $875\text{--}975\text{ cm}^{-1}$  are associated with aromatic C–H out-of-plane bending and are sensitive to the chain conformation and differences in packing and are known to distinguish between  $\delta$ , empty  $\delta$  ( $\delta_e$ ),  $\gamma$  and  $\varepsilon$  crystalline forms of sPS having the same helical chain conformation.<sup>13, 14, 28, 40, 41</sup>  $\delta$  (toluene) sample prepared from undrawn amorphous sPS film (Figure 4.3a) shows IR bands at 600.8, 608.2, 907.5, 933.5, and  $943.5\text{ cm}^{-1}$ , which are the characteristic peaks of the  $\delta$  cocrystal of sPS/toluene complex. Upon the exchange of toluene with *n*-nonane (Figure 4.3b), the position and intensity of these IR bands changed, confirming the phase transition and the IR bands are located at 599.6, 609.6, 907, 933.5 and  $943.6\text{ cm}^{-1}$ . These peak positions are not only different from the  $\delta$ -toluene (monoclinic) but also from the  $\gamma$  form (598.5, 610.0, 904, 932.8 and  $945.1\text{ cm}^{-1}$ ).

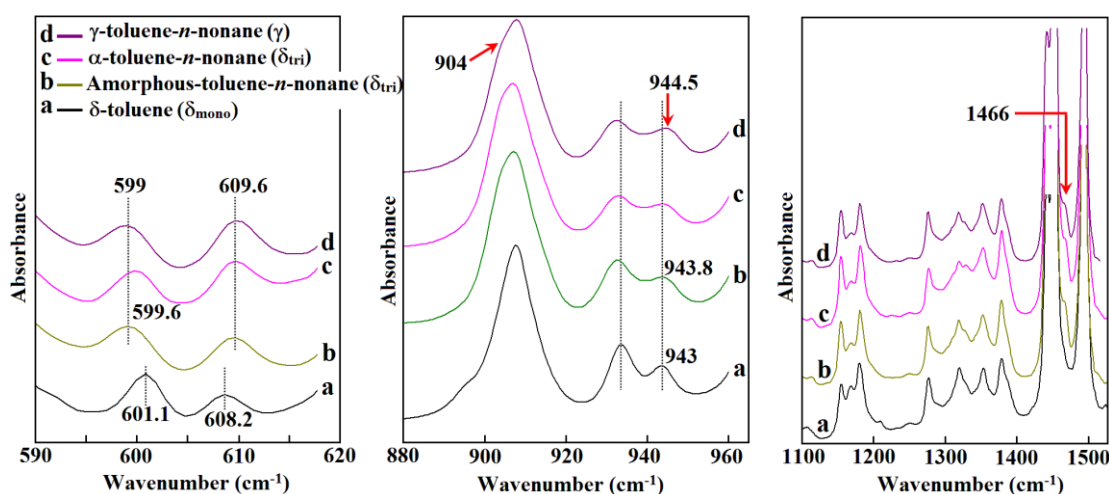


**Figure 4.3.** Infrared spectra of various samples in three frequency regions presenting conformation, packing sensitive bands and guest bands (a) toluene treated amorphous film, (b) *n*-nonane treated  $\delta$ -toluene film, (c) *n*-nonane treated  $\delta$ -toluene film prepared from the  $\alpha$  form as starting material and (d) *n*-nonane treated  $\delta$ -toluene film prepared from the  $\gamma$  form as starting material.

#### 4.4.2. Guest Exchange Process Using Toluene Treated $\alpha$ form Samples

In this section, instead of amorphous sPS films, undrawn  $\alpha$  form films were used to prepare sPS/toluene  $\delta$ -clathrate samples and the samples were used for guest exchange process with a series of *n*-alkanes ranging from *n*-octane to *n*-decane at room temperature. Figure 4.4 shows the X-ray diffraction patterns of undrawn  $\delta$  toluene sample before and after treatment with longer *n*-alkanes. X-ray

diffraction pattern of toluene treated  $\alpha$  form film shows reflections at  $2\theta = 8.0, 10.3, 17.4, 20.6,$  and  $23.4^\circ$  and these reflections are corresponding to the monoclinic  $\delta$  cocrystal of sPS/toluene complex. The  $d_{010}$  spacing estimated for the sPS/*n*-alkanes is lower than that of the starting sPS/toluene complex. The  $\delta$  cocrystal prepared in this route shows a strong reflection at  $2\theta = 20.6^\circ$ , due to the occurrence of strong crystalline phase orientation.<sup>42</sup> Upon guest exchange, the relative intensity of the reflection at  $2\theta = 8.0^\circ$  decreased and the position of the reflection at  $2\theta = 17.4^\circ$  changed to  $2\theta = 16.7^\circ$ . Similar observation was made by Tarallo et al. and they assigned such diffraction pattern to triclinic  $\delta$  cocrystal.<sup>37</sup> In all the samples initial crystalline phase orientation is maintained even after structural phase transition from monoclinic  $\delta$  cocrystal to triclinic  $\delta$  cocrystal. FTIR spectra shown in Figure 4.3c is similar to Figure 4.3b and confirms the replacement of toluene by *n*-nonane (band at  $1466\text{ cm}^{-1}$  appeared).

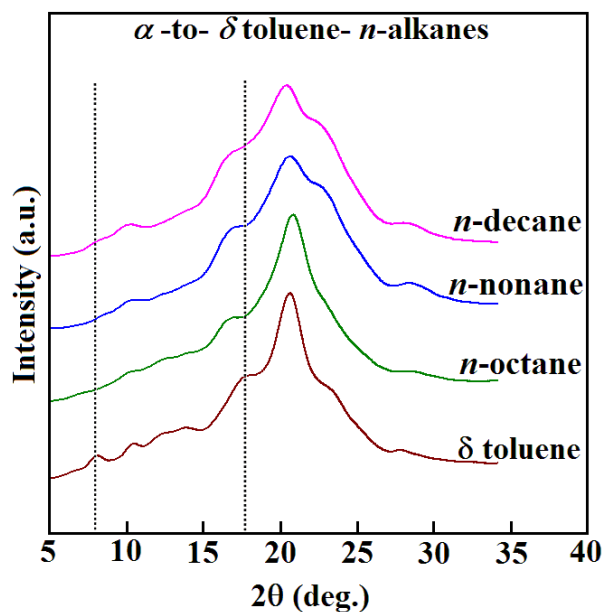


**Figure 4.4.** X-ray diffraction patterns of toluene treated  $\alpha$  form films after dipping in *n*-alkanes for 32 days. Toluene treated  $\alpha$  form is also shown for the purpose of comparison.

We further utilized uniaxially drawn samples to understand the phase transition behavior upon guest exchange process. sPS/toluene  $\delta$ -clathrate samples were prepared by treating uniaxially drawn  $\alpha$  form samples with toluene. Figure 4.5 shows 1D X-ray diffraction patterns of the sPS/toluene complex prepared from

the uniaxially drawn  $\alpha$  form together with the  $n$ -alkanes treated  $\delta$  cocrystal samples. Upon guest exchange, a clear change in the X-ray pattern is observed. In particular, relative intensity of the 010 reflection drastically reduced or completely disappeared upon the guest exchange process. As observed in the preceding section, FWHM of the observed reflections increased, indicating the presence of some disorder upon guest exchange process. The X-ray pattern observed upon the guest exchange process is similar to the X-ray pattern reported by Albuñia et al. for the disordered nanoporous crystalline form.<sup>43</sup> These results clearly suggest a structural phase transition from monoclinic  $\delta$  cocrystal to disordered crystalline form/triclinic form. Anyway, a detailed study is needed to understand the formation of disordered crystalline form with guest molecules.

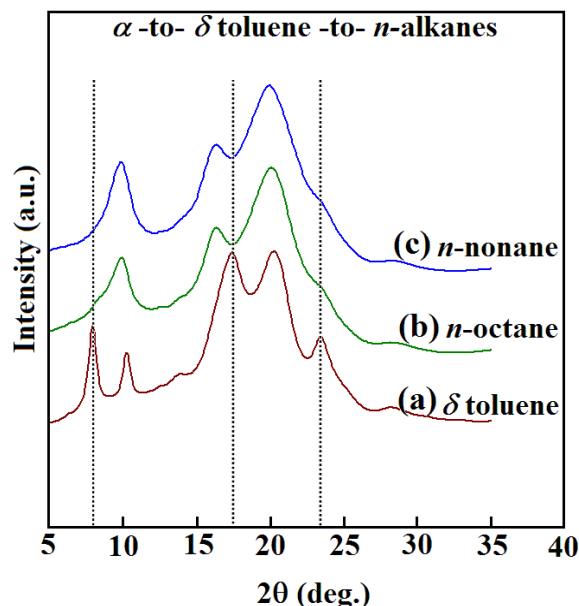


**Figure 4.5.** X-ray diffraction patterns of (a) toluene treated uniaxially drawn  $\alpha$  form sample ( $\delta$  toluene) (b)  $n$ -octane treated  $\delta$ -toluene for 32 days and (c)  $n$ -nonane treated  $\delta$ -toluene for 32 days.

By combining the experimental data of X-ray diffraction and infrared spectra, a plausible scheme is proposed to explain the phase transition behavior upon guest exchange process using the  $\delta$  cocrystal of sPS/toluene complex prepared from both amorphous phase (Figure 4.6a) and  $\alpha$  form (Figure 4.6b). Both amorphous and  $\alpha$  form samples transform to the  $\delta$  cocrystal (monoclinic) after dipping in toluene. Further treatment of the  $\delta$  cocrystal of sPS/toluene complex in

series of *n*-alkanes leads to the structural phase transition from  $\delta$  cocrystal (monoclinic) to  $\delta$  cocrystal (triclinic) irrespective of the initial morphology used for the preparation of sPS/toluene complex in undrawn samples. However, in the case of uniaxially drawn  $\alpha$  form samples, the  $\delta$  cocrystal of sPS/toluene complex transformed into a disordered crystalline form. As proposed in literature, the columnar model could be reasonably used to explain the results obtained here.<sup>14</sup> Treatment of sPS/toluene complex in *n*-alkanes leads to the expansion of the radius of column to some extent, and as a result longer *n*-alkanes enter into the columns and push out the existing toluene molecules. After removal of the samples from *n*-alkanes, shrinkage in the column radius may occur and as a result, longer *n*-alkanes ( $n = 8, 9$  and  $10$ ) accommodated themselves within the cavities. As the molecular volume of the longer *n*-alkanes is larger than that of the cavities, due to the geometric constraints *n*-alkanes take bent conformation to accommodate themselves within the cavities. A bend along the alkane chain (*gauche* conformation) can create steric repulsion between the hydrogens and increase the free energy requirements.<sup>44, 45</sup> The internal strain developed within the cavity causes some structural disorder in the crystal lattice and as a result the host structure transformed to the triclinic  $\delta$  cocrystal or disordered crystalline form.

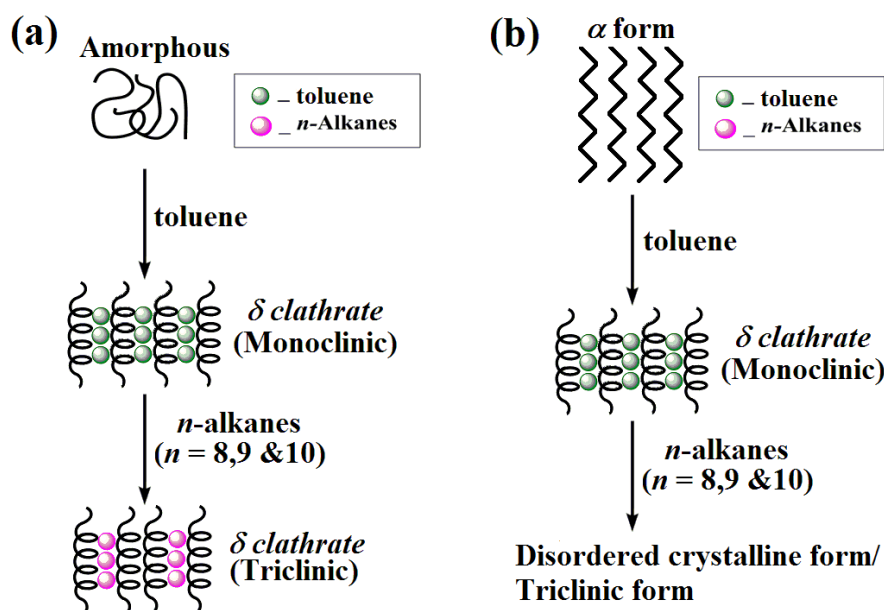


**Figure 4.6.** Schematic illustration of structural changes in the guest exchange process using (a) toluene treated amorphous samples and (b) toluene treated  $\alpha$  form samples.

#### 4.4.3. Guest Exchange Process Using Toluene Treated $\gamma$ form Samples

Undrawn  $\gamma$ -form films were used to prepare sPS/toluene  $\delta$ -clathrate samples and these samples were used for guest exchange process with a series of  $n$ -alkanes at room temperature. Figure 4.7 shows the X-ray diffraction patterns of the  $\gamma$  form, toluene treated  $\gamma$  form (i.e.  $\delta$  toluene), and  $n$ -alkanes containing samples after guest exchange process. X-ray diffraction pattern of toluene treated  $\gamma$  form film shows reflections corresponding to the typical monoclinic  $\delta$  cocrystal of sPS/toluene complex at  $2\theta = 8.4, 10.4, 17.1,$  and  $20.5^\circ$ . After dipping these samples in  $n$ -alkanes for 32 days, reflections corresponding to the  $\delta$  cocrystal of sPS/toluene complex disappear and are replaced by new reflections corresponding to the typical  $\gamma$  form ( $2\theta = 9.4, 10.3, 16.5,$  and  $20.4$ ).

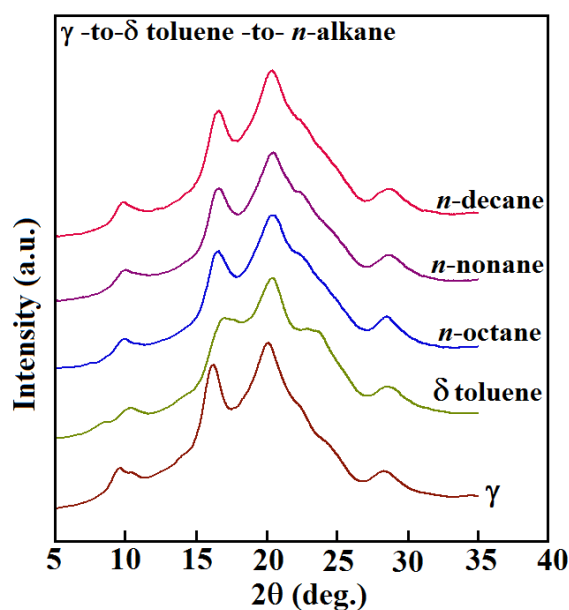


**Figure 4.7.** X-ray diffraction patterns of toluene treated  $\gamma$  form films after dipping in  $n$ -alkanes for 32 days. Toluene treated  $\gamma$  form ( $\delta$  toluene) and  $\gamma$  form are also shown in the figure for the purpose of comparison.

In another set of experiments, uniaxially drawn  $\gamma$  form was utilized to understand the structural phase transitions upon the guest exchange process. In this case, the intensities of the lower angle reflections are dominant enough to understand the phase transitions more precisely. Figure 4.8 shows the representative two-dimensional (2D) X-ray diffraction fiber patterns and one-

dimensional (1D) X-ray diffraction patterns of toluene treated  $\gamma$  form (i.e.  $\delta$  cocrystal) together with *n*-octane and *n*-nonane treated  $\delta$  cocrystal of sPS/toluene complex. The  $\delta$  cocrystal obtained in this route was completely transformed to the  $\gamma$  form in presence of *n*-alkanes after 32 days. Figure 4.3d shows representative infrared spectrum of *n*-nonane treated  $\delta$ -toluene film prepared from the  $\gamma$  form as starting sample. Upon guest exchange with *n*-nonane, the bands at 601.1 and 608.2  $\text{cm}^{-1}$  corresponding to the  $\delta$ -toluene shifted to 599 and 619.6  $\text{cm}^{-1}$ , indicating the structural phase transition to the  $\gamma$  form. Appearance of a shoulder at 904  $\text{cm}^{-1}$  to the peak centered 909  $\text{cm}^{-1}$  also confirms the formation of the  $\gamma$  form.<sup>41</sup> However, it is worth pointing here that the band corresponding to the *n*-nonane at 1466  $\text{cm}^{-1}$  (scissoring of the C–H bonds in the methylene group) is present in the  $\gamma$  form after guest exchange. It has been known that the  $\gamma$  form is guest-free and guest occupies the amorphous region of the  $\gamma$  form in solvent-rich gels.<sup>46</sup> Therefore, in the present case *n*-alkane molecules are speculated to reside in the amorphous phase of the  $\gamma$  form due to their high boiling point.

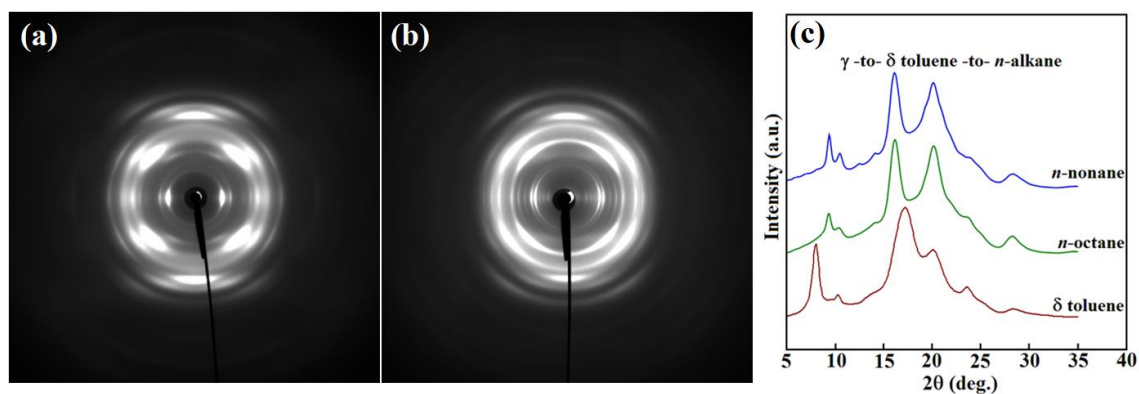


**Figure 4.8.** X-ray fiber diagrams of (a) toluene treated uniaxially drawn  $\gamma$  form (b) *n*-nonane treated sPS/toluene complex for 32 days and (c) 1D intensity profiles of various samples (as indicated) by the circular integration of 2D diffraction patterns.

Based on the X-ray diffraction and infrared spectroscopy, the following phase transition model (Figure 4.9) is proposed. Treatment of the  $\gamma$  form with toluene molecules leads to the formation of the monoclinic  $\delta$  cocrystal.<sup>42</sup> After treatment of such obtained  $\delta$  cocrystal with longer *n*-alkanes (*n*-octane to *n*-nonane), surprisingly, instead of guest exchange, the structure is transformed back

to the  $\gamma$  form. For the first time, we observed such a transition from  $\delta$  cocrystal to  $\gamma$  form in presence of bulky guests like  $n$ -alkanes. To explain such phase transition, we may speculate that when the bulky guests like  $n$ -alkanes approach the  $\delta$  cocrystal, the distance between the  $ac$  parallel layers of  $s(2/1)2$  helices may slightly increase due to the swelling effect in the crystalline and amorphous interface. At the same time, the toluene molecules which are residing in the crystal lattice of the  $\delta$  cocrystal migrate out of the lattice. As a result the  $\delta$  cocrystal may change transiently to the  $\delta_e$  form, and subsequently to the  $\gamma$  form in presence of  $n$ -alkanes.

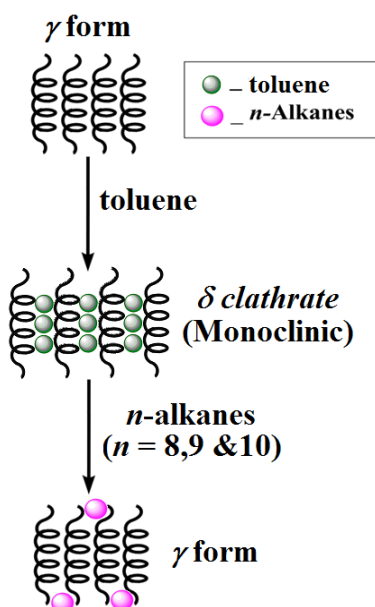


**Figure 4.9.** Schematic illustration of structural change in the guest exchange process using toluene treated  $\gamma$  form samples.

In the literature it is reported that  $\delta$  to  $\gamma$  transition occurs at  $T_g$  of sPS and the presence of guest molecules in the amorphous phase reduces the  $\delta$  to  $\gamma$  transition temperature due to the reduction in  $T_g$ .<sup>47, 48</sup> We speculate that the  $T_g$  of sPS is lowered well below room temperature in presence of  $n$ -alkanes environment and it facilitates the  $\delta_e$  to  $\gamma$  transition upon guest exchange process. Such reduction in the  $T_g$  of sPS in presence of various organic solvents was reported by Yoshioka et al. using time resolved infrared spectroscopy.<sup>49</sup> It may be noted that the toluene treated amorphous and  $\alpha$  form samples transforms into the triclinic  $\delta$

cocrystal/disordered crystalline form and not to the  $\gamma$  form. These results suggest that the  $\delta$  cocrystal prepared from the amorphous,  $\alpha$  and  $\gamma$  phases behave differently upon the guest exchange process. On the basis of these observations, it might be speculated that in presence of *n*-alkanes environment, the mobility in the crystalline and amorphous interface of the monoclinic  $\delta$  cocrystal prepared from different morphologies is different and determines the phase transitions upon guest exchange process.

For the purpose of comparison and to understand structural phase transitions more concretely, guest exchange process was performed using chloroform treated amorphous,  $\alpha$  and  $\gamma$  samples under the similar conditions.

#### **4.4.4. Guest Exchange Process Using Chloroform Treated Amorphous Samples**

Gowd et al., performed guest exchange process with *n*-alkanes using chloroform treated amorphous samples (i.e. monoclinic  $\delta$  cocrystal).<sup>36</sup> In that work, guest exchange process was performed for shorter duration and guest exchange was not fully completed. sPS/chloroform  $\delta$ -clathrate samples were prepared by dipping undrawn amorphous sPS films directly into chloroform for 12 hours at room temperature. Thus prepared samples were used for the guest exchange process with a series of *n*-alkanes ranging from *n*-octane to *n*-decane at room temperature for different intervals of time up to 32 days and the structural changes were monitored through X-ray diffraction measurements at different times (Figure 4.10).

X-ray diffraction pattern of undrawn sPS/chloroform sample shows reflections characteristic to the typical monoclinic  $\delta$  cocrystal ( $2\theta = 8.2, 10.3, 17.2, 20.6, 23.2, \text{ and } 28.4^\circ$ ). After treating with *n*-alkanes, reflections characteristic of the monoclinic  $\delta$  cocrystal ( $17.4$  and  $23.2^\circ$ ) started to decrease its intensity over a period of time and simultaneously new reflections appeared, which are characteristic of the both  $\varepsilon$  cocrystal ( $6.9$  and  $23.6^\circ$ ) and triclinic  $\delta$  cocrystal ( $16.6^\circ$ ). It is worth highlighting that the X-ray diffraction patterns observed after the guest exchange process are in very good agreement with those reported by

Gowd et al.<sup>36</sup> and are different with those reported in the literature by Tarallo et al.<sup>37</sup> As seen in Figure 4.10, the monoclinic  $\delta$  cocrystal transformed to a mixture of  $\varepsilon$  cocrystal and triclinic  $\delta$  cocrystal at different times in different *n*-alkanes. These results suggest that molecular size, solubility parameter and vapor pressure of the *n*-alkanes determines the duration of the guest exchange process.

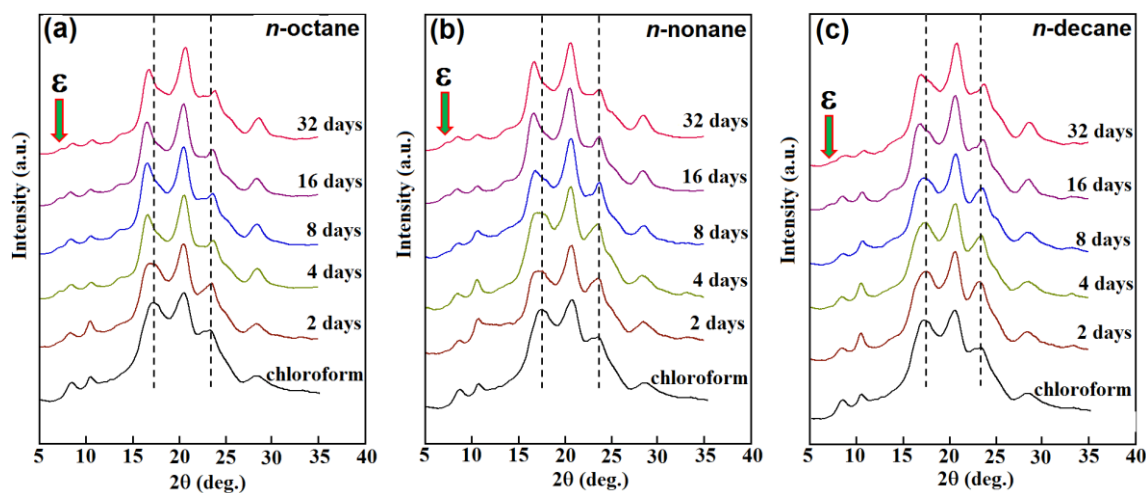
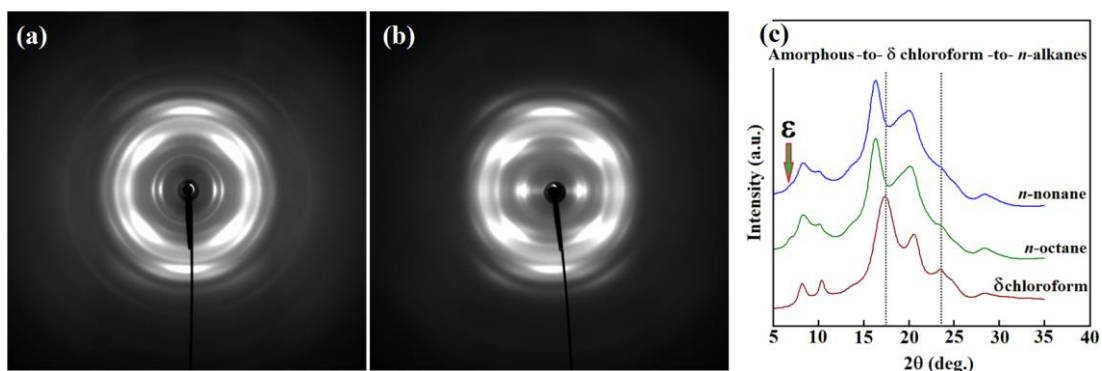


**Figure 4.10.** X-ray diffraction patterns of chloroform treated amorphous films (for 1 day) after dipping in *n*-alkanes for the indicated time intervals (a) *n*-octane (b) *n*-nonane and (c) *n*-decane. For the purpose of comparison, chloroform treated amorphous sample is shown too.

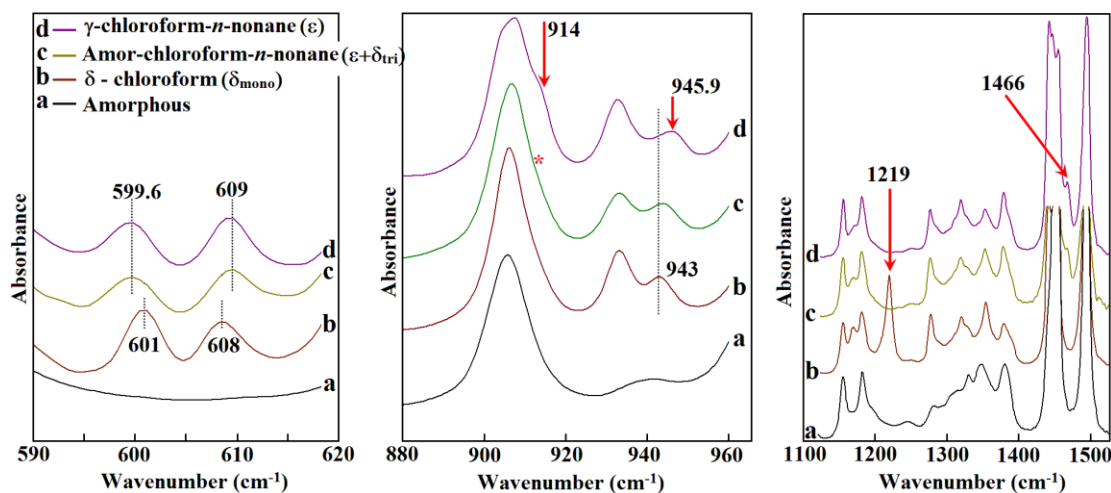
We further utilized the uniaxially drawn samples. In these experiments, as drawn samples, with a mesophase of all-trans planar-zigzag conformation were used to prepare the  $\delta$  cocrystal of sPS/chloroform complex. Figure 4.11 shows the representative two-dimensional (2D) X-ray diffraction fiber patterns and one-dimensional (1D) X-ray diffraction patterns of  $\delta$  cocrystal of sPS/chloroform complex together with *n*-octane and *n*-nonane treated  $\delta$  cocrystal of sPS/chloroform complex. After treating with *n*-alkanes, reflections characteristic of the monoclinic  $\delta$  cocrystal ( $17.4$  and  $23.3^\circ$ ) disappeared and these reflections are replaced with new reflections corresponding to the  $\varepsilon$  cocrystal ( $6.9^\circ$ ) and triclinic  $\delta$  cocrystal ( $16.4^\circ$ ).

Figure 4.12 shows FTIR spectra of amorphous sPS film (Figure 4.12a) along with the  $\delta$  cocrystal of sPS/chloroform complex (Figure 4.12b) and *n*-nonane treated  $\delta$  (chloroform) cocrystal (Figure 4.12c) in three different spectral regions.

As reported in the literature, the spectral region  $1100\text{--}1500\text{ cm}^{-1}$  gives the information about the guest exchange process.<sup>31</sup>



**Figure 4.11.** X-ray fiber diagrams of (a) chloroform treated uniaxially drawn amorphous sample (b) *n*-nonane treated sPS/chloroform complex for 32 days and (c) 1D intensity profiles of various samples (as indicated) by the circular integration of 2D diffraction patterns.



**Figure 4.12.** Infrared spectra of various samples in three frequency regions presenting conformation, packing sensitive bands and guest bands (a) amorphous film, (b) chloroform treated amorphous film ( $\delta$ -chloroform), (c) *n*-nonane treated  $\delta$ -chloroform film and (d) *n*-nonane treated  $\delta$ -chloroform film prepared from the  $\gamma$  form.

In Figure 4.12c, the complete disappearance of the chloroform band at  $1219\text{ cm}^{-1}$  (C–H deformation) and appearance of the *n*-nonane band at  $1466\text{ cm}^{-1}$  (scissoring of the C–H bonds in the methylene group) confirms the complete replacement of chloroform by *n*-nonane. sPS/chloroform  $\delta$ -clathrate sample prepared from undrawn amorphous sPS film (Figure 4.12b) shows IR bands at  $600.7, 608.5, 906.0, 933.1,$  and  $942.8\text{ cm}^{-1}$ , which are the characteristic peaks of the  $\delta$  (chloroform) sample. Upon exchange of chloroform with *n*-nonane (Figure

4.12c), the position and intensity of these IR bands changed confirming the phase transition and the IR bands are located at 600, 609, 906.6 (with a shoulder at 914), 932.4 and 944.2  $\text{cm}^{-1}$ . These peak positions are not only different from the  $\delta_{\text{chl}}$  (monoclinic) but also from the  $\gamma$  form. At this point, however, it is rather difficult to assign these peaks to any particular crystalline form as the resultant spectrum is the combination of two crystalline forms ( $\delta$  triclinic +  $\varepsilon$ ), which have similar  $s(2/1)_2$  helical conformation. A shoulder at 914  $\text{cm}^{-1}$  confirms the presence of the  $\varepsilon$  cocrystal.<sup>41</sup>

By combining the experimental data presented above, we propose a model, as shown schematically in Figure 4.13, to explain the phase transition behavior upon guest exchange process using the  $\delta$  cocrystal of sPS/chloroform complex prepared from amorphous phase. These results suggest that after guest exchange, the  $\delta$  cocrystal (monoclinic) transforms into the mixture of  $\delta$  triclinic and  $\varepsilon$  cocrystals where longer  $n$ -alkanes hosted both inside the cavities as well as the channels. These results are different from the observations made in toluene treated amorphous samples where the monoclinic  $\delta$  cocrystal transformed into the triclinic  $\delta$  cocrystal upon guest exchange process.

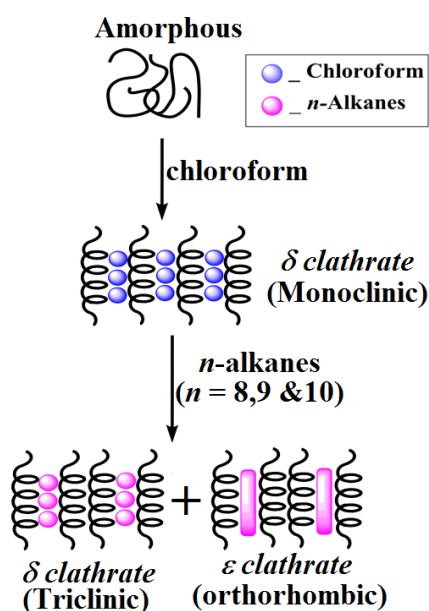


**Figure 4.13.** Schematic illustration of structural changes in the guest exchange process using chloroform treated amorphous samples.

#### 4.4.5. Guest Exchange Process Using Chloroform Treated $\alpha$ form Samples

In this section, instead of amorphous sPS films, undrawn  $\alpha$  form films were used to prepare sPS/chloroform  $\delta$ -clathrate samples. Such prepared  $\delta$ -clathrate samples were used for guest exchange process with a series of  $n$ -alkanes ranging from  $n$ -octane to  $n$ -decane at room temperature. It is worth mentioning here that Tarallo et al. used such chloroform treated undrawn  $\alpha$  form powder samples for guest exchange process.<sup>37</sup> Figure 4.14 shows the X-ray diffraction patterns of  $\delta$  chloroform sample together with the  $n$ -alkanes treated  $\delta$  cocrystal samples.

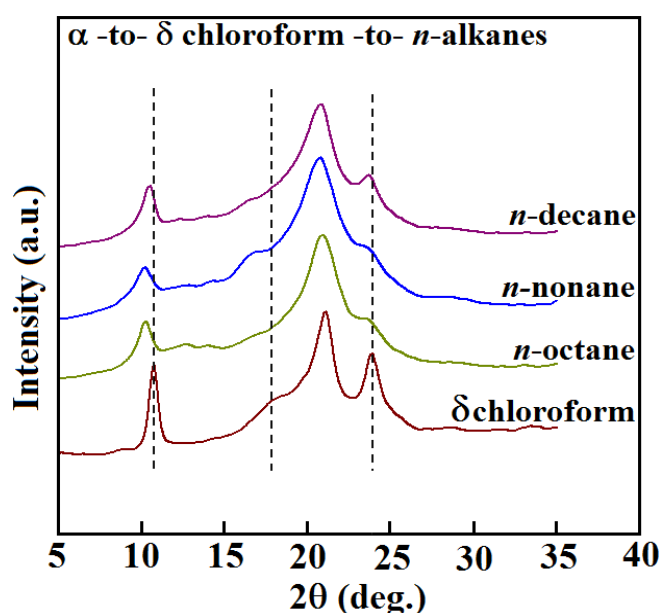


**Figure 4.14.** X-ray diffraction patterns of chloroform treated  $\alpha$  form films after dipping in  $n$ -alkanes for 32 days. For the purpose of comparison, chloroform treated  $\alpha$  form is also shown.

X-ray diffraction pattern of the chloroform treated  $\alpha$  form film shows intense reflections at  $2\theta = 10.7, 21.1,$  and  $23.8^\circ$  corresponding to  $\bar{2}10, \bar{3}21$  and  $\bar{4}21/\bar{4}11$  planes, respectively. It is, however, worth pointing that these X-ray patterns are somewhat different with those reported by Tarallo et al.<sup>37</sup> The occurrence of strong molecular orientation is clearly seen in the X-ray pattern by the variation of the  $\bar{2}10$  reflection intensity with respect to the powder sample reported by Tarallo et al.,<sup>37</sup> and this pattern is very similar to the pattern reported by Alburnia et al., indicating the presence of uniplanar  $\bar{2}10$  orientation.<sup>42, 50</sup> It is evident from the X-ray diffraction patterns that after guest exchange with  $n$ -

alkanes, monoclinic  $\delta$  cocrystal (10.7, 21.1 and 23.8°) transformed to triclinic  $\delta$  cocrystal (10.2, 20.7 and 23.8°). The relative intensity of the reflection at  $2\theta = 23.8^\circ$  was decreased drastically in the triclinic  $\delta$  cocrystal. In all the samples initial uniplanar orientation is maintained perfectly even after structural phase transition from monoclinic  $\delta$  cocrystal to triclinic  $\delta$  cocrystal. It is also worth highlighting here that no trace of the  $\varepsilon$  cocrystal is detected when chloroform treated  $\alpha$  form samples were used for the guest exchange process with  $n$ -alkanes.

In another set of experiments, sPS/chloroform  $\delta$ -clathrate samples were prepared by treating uniaxially drawn  $\alpha$  form samples with chloroform. Figure 4.15 shows representative 2D X-ray diffraction fiber patterns and 1D X-ray diffraction patterns of the sPS/chloroform complex prepared from the uniaxially drawn  $\alpha$  form together with the  $n$ -alkanes treated  $\delta$  cocrystal samples. Upon guest exchange, small differences occur in the peak positions and intensities of X-ray reflections. In particular, the X-ray reflection corresponding to the 010 plane is dominant in uniaxially drawn samples and it allowed us to estimate the  $d_{010}$  more accurately. The  $d_{010}$  spacing calculated for the sPS/ $n$ -alkane complexes upon the guest exchange from chloroform ( $\leq 1.05$  nm) is less than that of the  $\delta_e$  form despite the bulkiness of the  $n$ -alkanes. These results clearly suggested the structural phase transition from monoclinic  $\delta$  cocrystal to triclinic  $\delta$  cocrystal.

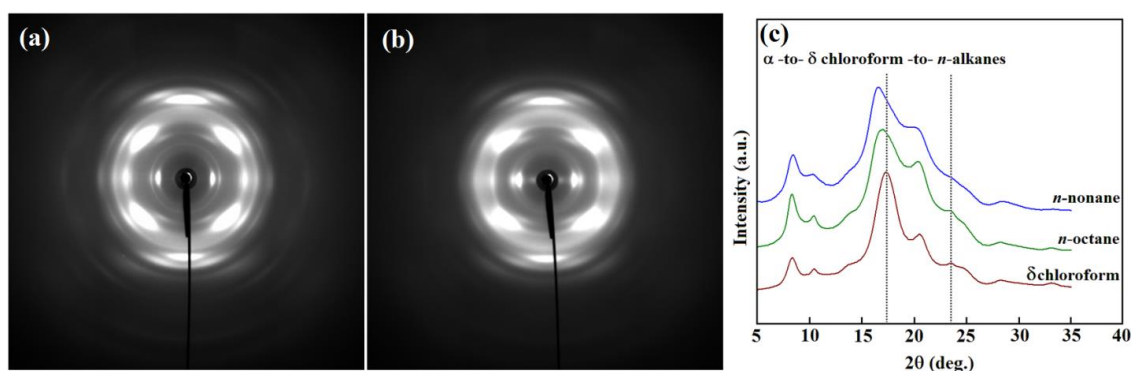


**Figure 4.15.** X-ray fiber diagrams of (a) chloroform treated uniaxially drawn  $\alpha$  form (b)  $n$ -nonane treated sPS/chloroform complex for 32 days and (c) 1D intensity profiles of various samples (as indicated) by the circular integration of 2D diffraction patterns.

Based on the present data and the information already available in the literature, a schematic model is proposed to explain the phase transition behavior upon guest exchange process using chloroform treated  $\alpha$  form and the schematic diagram is shown in Figure 4.16. In this case, upon guest exchange, the  $\delta$  cocrystal (monoclinic) transformed to the  $\delta$  cocrystal (triclinic) where longer  $n$ -alkanes ( $n = 8, 9$  and  $10$ ) accommodated themselves within the cavities with bent conformation. These results suggested that, the  $\delta$  cocrystal prepared from the amorphous phase and the  $\alpha$  phase behave differently upon the guest exchange process. We may speculate that the crystalline and amorphous interface of the  $\delta$  cocrystal prepared from the  $\alpha$  form is structurally more rigid and upon guest exchange, monoclinic  $\delta$  cocrystal transformed to the triclinic  $\delta$  cocrystal. These results are similar to that found in the case of toluene treated amorphous samples as discussed in the preceding section.

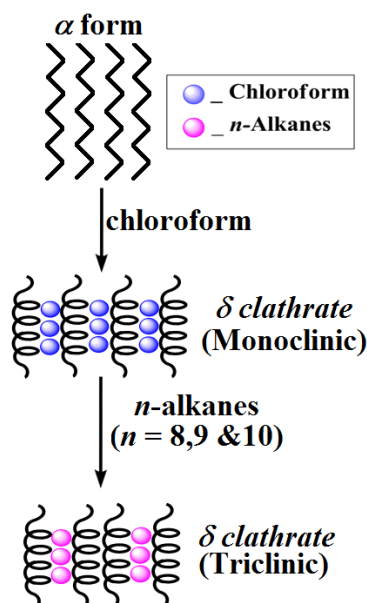


**Figure 4.16.** Schematic illustration of structural change in the guest exchange process of chloroform treated  $\alpha$  form samples.

#### 4.4.6. Guest Exchange Process Using Chloroform Treated $\gamma$ form Samples

Undrawn  $\gamma$  form films were treated with chloroform to obtain the sPS/chloroform complex, which after guest removal transformed into the  $\varepsilon$  cocrystal. sPS/chloroform complex obtained by this route is used for guest

exchange process with a series of *n*-alkanes. X-ray diffraction patterns of the  $\epsilon$  cocrystal together with the sPS/*n*-alkane complexes obtained upon guest exchange process are shown in Figure 4.17.

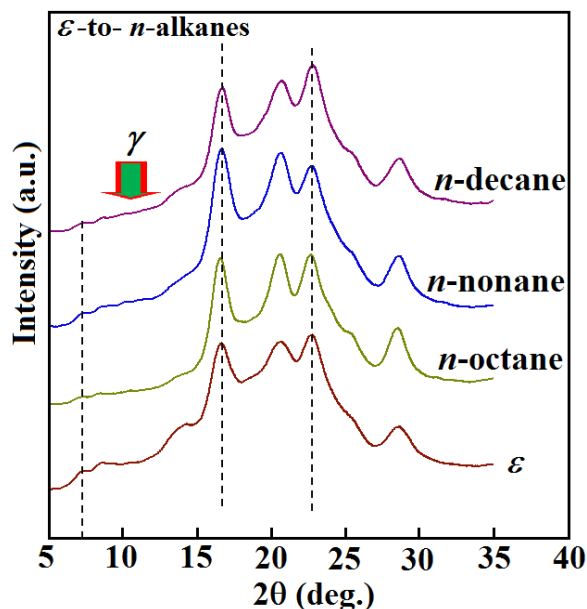


**Figure 4.17.** X-ray diffraction patterns of chloroform treated  $\gamma$  form films after dipping in *n*-alkanes for 32 days. The pattern of  $\epsilon$  cocrystal is also given for the purpose of comparison.

X-ray diffraction pattern of the chloroform extracted sample shows strong reflections at  $2\theta = 6.9, 8.2, 16.3, 20.4,$  and  $22.5^\circ$ , which are characteristic reflections of the  $\epsilon$  cocrystal and in addition to that a minor content of the  $\gamma$  form is also observed. Intense reflection at  $2\theta = 22.5^\circ$  corresponds to the 002 reflection, and it is due to the preferential perpendicular orientation of the crystalline chain axes with respect to the film plane.<sup>50</sup> It is worth mentioning here that, Tarallo et al. studied the guest exchange process with *n*-alkanes using the  $\epsilon$  cocrystal as the starting material.<sup>38</sup> Their samples did not show the preferential 002 orientation due to the powder samples used to obtain the  $\epsilon$  cocrystal. Upon the guest exchange with *n*-alkanes, the X-ray diffraction patterns of sPS/*n*-alkane complexes remain unchanged irrespective of the size or volume of the guest molecules. It is worth highlighting here the preferential (002) perpendicular orientation of the crystalline chain axes with respect to the film plane is retained perfectly upon the guest exchange process. FTIR spectra shown in Figure 4.12d, confirms the replacement

of chloroform by *n*-nonane and the appearance of IR band at  $914\text{ cm}^{-1}$  confirms the presence of the  $\varepsilon$  cocrystal.

Uniaxially drawn samples are also used to understand the phase transition behavior upon the guest exchange process. In this section, sPS/clathrate ( $\delta$  cocrystal) samples were prepared by chloroform treatment on uniaxially drawn  $\gamma$  form samples. Figure 4.18 shows representative 2D fiber patterns and 1D X-ray diffraction patterns of the  $\delta$  cocrystal together with the sPS/*n*-alkane complexes obtained upon guest exchange process. The  $\delta$  cocrystal obtained in this route presents a minor amount of the  $\gamma$  form, as evidenced from the shoulder at  $2\theta = 11^\circ$ . Upon the guest exchange with longer *n*-alkanes, the monoclinic  $\delta$  cocrystal transformed to the  $\varepsilon$  cocrystal and the minor content of the  $\gamma$  form remained as such.

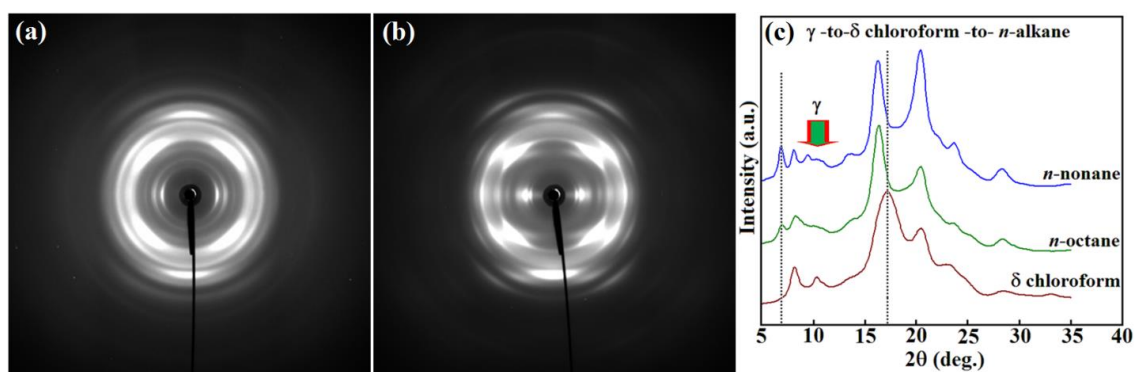


**Figure 4.18.** X-ray fiber diagrams of (a) chloroform treated uniaxially drawn  $\gamma$  form (b) *n*-nonane treated sPS/chloroform complex for 32 days and (c) 1D intensity profiles of various samples (as indicated) by the circular integration of 2D diffraction patterns.

Figure 4.19 shows the schematic illustration of the phase transition behavior upon guest exchange process using chloroform treated  $\gamma$  form. Major content of the  $\gamma$  form transformed to the  $\delta$  cocrystal, which after transformed to the  $\varepsilon$  cocrystal upon guest exchange with longer *n*-alkanes. In the preceding section, when the toluene was used as a guest molecule, the  $\delta$  cocrystal prepared from the  $\gamma$  form transformed back to the  $\gamma$  form in presence of longer *n*-alkanes. We speculated that the  $\delta$  cocrystal transformed the  $\gamma$  form via  $\delta_e$  form. In the present case, when *n*-alkanes approach the  $\delta$  cocrystal, chloroform which is residing in the crystal lattice

excludes from the lattice. But in this case, as already pointed out in the literature, instead of  $\delta_e$  form, the nanoporous  $\varepsilon$  is obtained where channels shaped cavities are crossing the unit cell along the c-direction.<sup>29, 41</sup> It is also worth adding that, up to now, chloroform is the only guest that induces the  $\varepsilon$  cocrystal upon the guest removal, which may be due to the not planar shape of the chloroform.<sup>51</sup> Longer *n*-alkanes can smoothly enter the channel shaped cavities of nanoporous  $\varepsilon$  form with their main molecular axis roughly parallel to the polymer chain axis with all-trans conformation and stabilizes the  $\varepsilon$  structure.

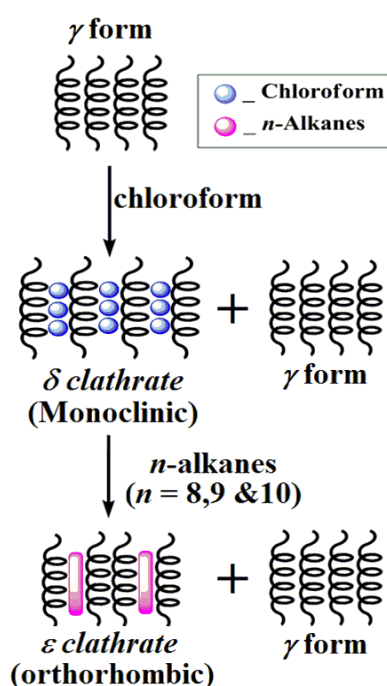


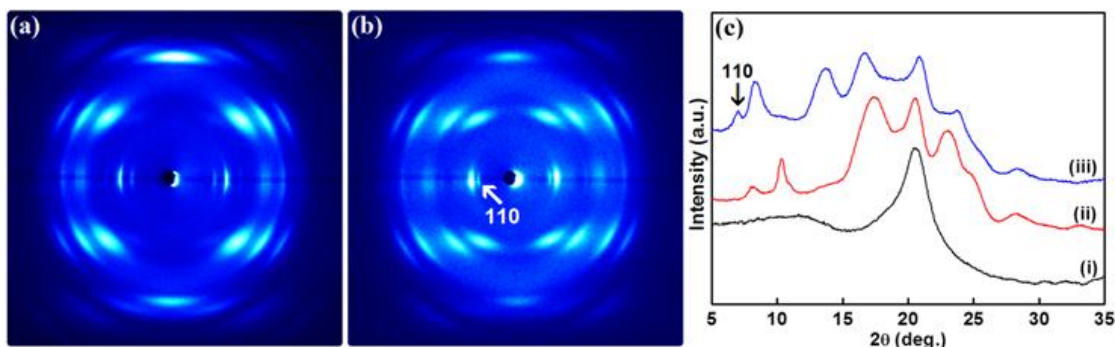
**Figure 4.19.** Schematic illustration of structural changes in the guest exchange process using chloroform treated  $\gamma$  form samples.

In order to investigate the structural phase transitions of sPS upon the guest extraction process, samples having two different initial morphologies such as amorphous and  $\gamma$  form were used as the starting materials and the cocrystals were prepared using chloroform as the guest molecule. Selective extraction of guest molecules resulted in complex phase transitions of the host structure.

#### 4.4.7. Guest Extraction from Chloroform Treated Amorphous Samples

Figure 4.20 shows the 2D X-ray diffraction patterns of chloroform treated uniaxially drawn amorphous samples and corresponding 1D profiles obtained upon

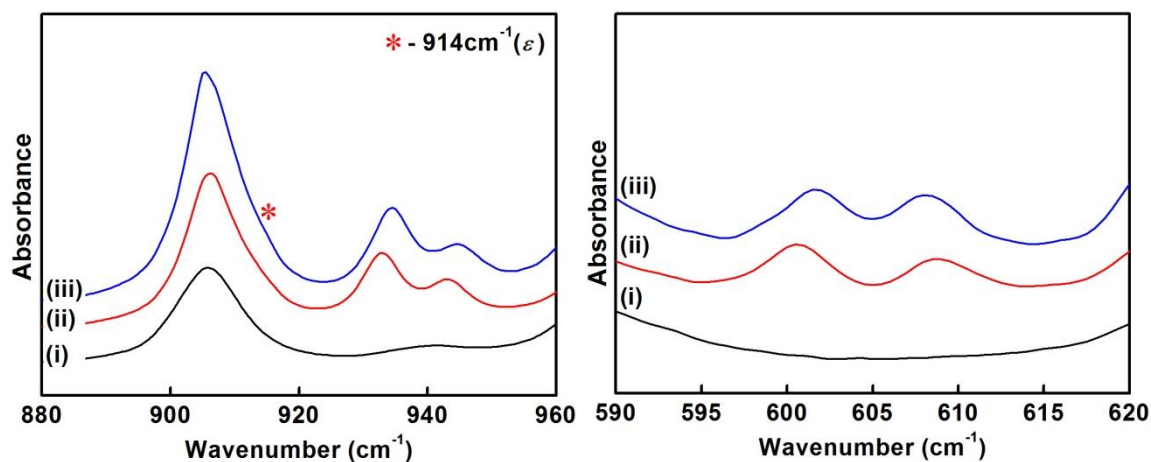
the guest extraction process. As expected the treatment of uniaxially drawn sPS with chloroform resulted in the formation of  $\delta$  cocrystal (Figure 4.20a & 4.20c) with peak positions at  $2\theta = 8.1, 10.3, 17.4, 20.5$  and  $23.1^\circ$ . After the guest extraction, new reflections were observed at  $2\theta = 6.9, 8.3, 13.6, 16.6, 20.8$  and  $23.8^\circ$ .<sup>51</sup> The appearance of the reflection at  $2\theta = 6.9^\circ$  (110) confirms the presence of  $\varepsilon$  ( $\varepsilon_e$ ) form along with the  $\delta$  ( $\delta_e$ ) form in the chloroform extracted samples.



**Figure 4.20.** 2D X-ray fiber diagrams of (a) chloroform treated uniaxially drawn amorphous sample (b) the resultant pattern obtained after the guest extraction and (c) the corresponding one-dimensional patterns (ii) and (iii) obtained by the circular integration of a and b, respectively. One-dimensional pattern of uniaxially drawn amorphous sample (i) is shown in (c) for the purpose of comparison.

To confirm the WAXS results, FTIR spectra of the thin films of chloroform treated amorphous samples were collected before and after solvent extraction. The appearance of peaks in the region  $920\text{ cm}^{-1}$  to  $960\text{ cm}^{-1}$  and  $590$  to  $620\text{ cm}^{-1}$  indicates the formation of the helical structure (Figure 4.21). The peaks at  $600.7\text{ cm}^{-1}$  and  $608.8\text{ cm}^{-1}$ , which are sensitive to the chain packing mode, moves closer to  $601.8\text{ cm}^{-1}$  and  $608\text{ cm}^{-1}$  indicating the removal of chloroform molecules after the guest extraction. The presence of a shoulder peak at  $914\text{ cm}^{-1}$  in chloroform extracted sample confirms the appearance of  $\varepsilon_e$  form along with  $\delta_e$  form. These results are clearly showed that when the chloroform was used as the guest molecule to prepare the cocrystal form of sPS, upon the chloroform extraction, the structure is transformed to a mixture of  $\delta$  ( $\delta_e$ ) and  $\varepsilon$  ( $\varepsilon_e$ ) forms. It is also worth mentioning here that the chloroform treated amorphous sample ( $\delta_{\text{chl}}$ ) transformed

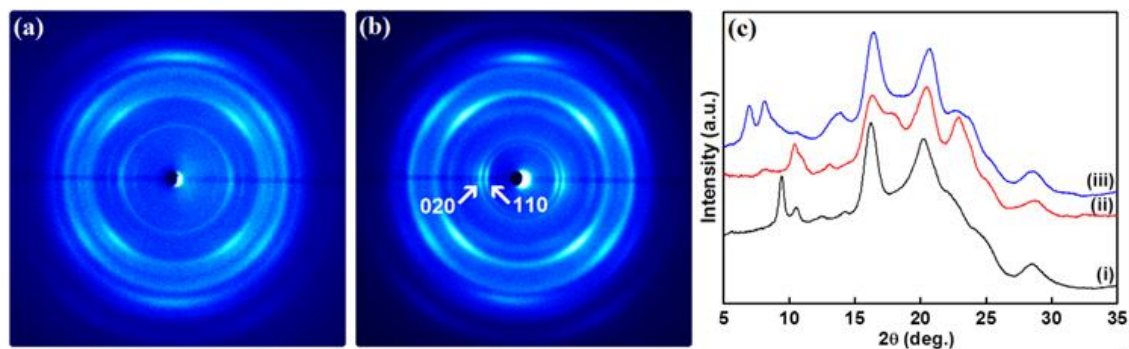
into the mixture of the  $\delta$  cocrystal and the  $\varepsilon$  cocrystal upon the guest exchange process.<sup>7, 28, 36, 52</sup>



**Figure 4.21.** Infrared spectra of (i) amorphous sPS (undrawn) (ii) chloroform treated amorphous sPS and (iii) the resultant pattern obtained after the guest extraction with acetonitrile in two different regions.

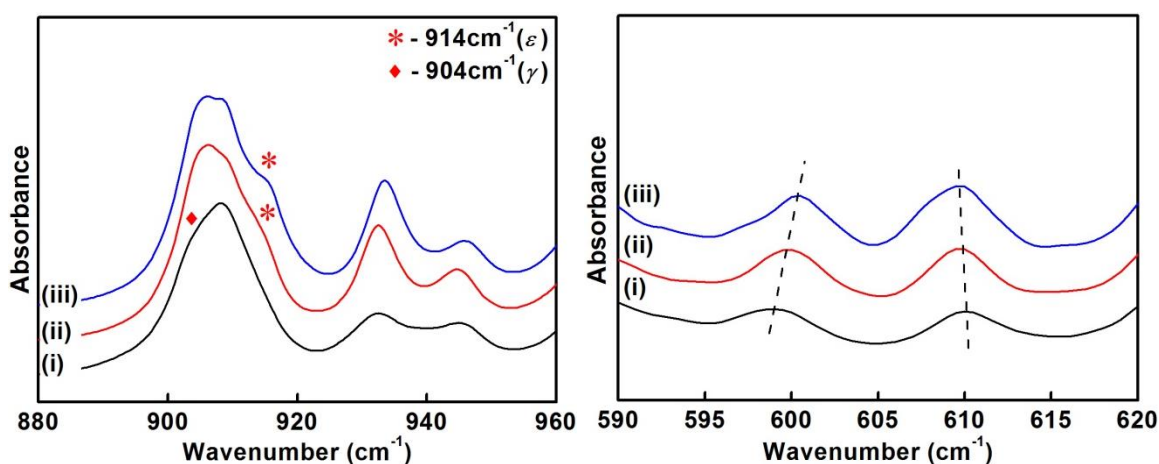
#### 4.4.8. Guest Extraction from Chloroform Treated $\gamma$ form Samples

Figure 4.22 shows the changes in the 2D X-ray diffraction patterns and the corresponding 1D profiles of chloroform treated  $\gamma$  form samples upon the solvent extraction process. As already reported in the literature,<sup>29, 52</sup> the uniaxially drawn  $\gamma$  form gets converted into  $\delta$  cocrystal after the treatment with chloroform, which is contrary to the behavior of undrawn samples where the  $\gamma$  form transforms directly into the  $\varepsilon$  cocrystal after the treatment with chloroform. Chain orientation in uniaxially drawn samples has a significant effect on the solvent evaporation rate from the crystalline and amorphous phases of sPS/solvent complex. Solvent evaporation rate might be responsible for such a difference in the structure of host sPS in chloroform treated  $\gamma$  form samples. If the uniaxially drawn samples were kept undisturbed at room temperature for a long time, slowly the  $\delta$  cocrystal structure gets converted into the  $\varepsilon$  cocrystal. However, upon the guest extraction using acetonitrile, both undrawn and uniaxially drawn samples readily transformed to the nanoporous  $\varepsilon$  ( $\varepsilon_c$ ) form. It is evident from the appearance of intense 110 and 020 reflections as shown in Figure 4.22b.<sup>29</sup>



**Figure 4.22.** 2D X-ray fiber diagrams of (a) chloroform treated uniaxially drawn  $\gamma$  form (b) the resultant pattern obtained after the guest extraction and (c) the one-dimensional patterns of (i) uniaxially drawn  $\gamma$  form (ii) chloroform treated uniaxially drawn  $\gamma$  form ( $\delta_{\text{chl}}$ ) and (iii)  $\delta_{\text{chl}}$  after the guest extraction.

Detailed information about the structural changes upon the guest extraction was also obtained from the FTIR measurements as shown in figure 4.23. Since thin films were used for the FTIR measurements, the treatment of  $\gamma$  form with chloroform resulted in the formation of  $\varepsilon$  cocrystal, and that is evident from the appearance shoulder peak at  $914\text{ cm}^{-1}$ .<sup>53</sup> This peak becomes more dominant after the guest extraction process suggests the structural transition from  $\varepsilon$  to nanoporous  $\varepsilon$  ( $\varepsilon_e$ ). The changes observed in a pair of bands in the frequency region  $590\text{--}620\text{ cm}^{-1}$  also indicates the structural phase transitions in host sPS upon the guest extraction process.



**Figure 4.23.** Infrared spectra of (i)  $\gamma$  form (undrawn) (ii) chloroform treated  $\gamma$  form and (iii) the resultant pattern obtained after the guest extraction with acetonitrile in two different regions.

## 4.5. Conclusions

In this chapter we have investigated the structure controlling factors in sPS upon the guest exchange and guest extraction processes by means of X-ray diffraction, and Fourier transform infrared spectroscopy. The data obtained in this paper, combined with the information already available in the literature, allowed us to conclude the following points.

1. The toluene treated amorphous samples ( $\delta_{\text{tol}}$ ) transforms into the triclinic  $\delta$  cocrystal upon the guest exchange process. No trace of the  $\varepsilon$  cocrystal was observed in these samples. On the other hand, the toluene treated  $\alpha$  form samples ( $\delta_{\text{tol}}$ ) transforms into the triclinic  $\delta$  cocrystal/disordered crystalline form upon the guest exchange process.
2. For the first time, we observed that the toluene treated  $\gamma$  form samples, i.e. monoclinic  $\delta$  cocrystal reverts to the  $\gamma$  form in presence of longer  $n$ -alkanes. No evidence of guest exchange was observed in these samples.
3. The chloroform treated amorphous sample ( $\delta_{\text{chl}}$ ) transforms into a mixture of  $\delta$  cocrystal (triclinic) and  $\varepsilon$  cocrystal upon the guest exchange process.
4. The chloroform treated  $\alpha$  form samples ( $\delta_{\text{chl}}$ ) transforms into the triclinic  $\delta$  cocrystal upon the guest exchange with  $n$ -alkanes.
5. The chloroform treated  $\gamma$  form samples ( $\delta_{\text{chl}}$ ) transforms into the  $\varepsilon$  form after the guest exchange with  $n$ -alkanes.
6. Guest extraction from chloroform treated amorphous samples gave a mixture of nanoporous  $\delta$  ( $\delta_e$ ) and  $\varepsilon$  ( $\varepsilon_e$ ) forms.
7. Guest extraction from chloroform treated  $\gamma$  form samples gave nanoporous  $\varepsilon$  ( $\varepsilon_e$ ) with channel-shaped cavities.

Based on the present results, it can be postulated that the starting morphology as well as the solvents used has a strong influence in tuning the final morphology and the porosity of sPS after the guest exchange and guest extraction processes, respectively.

#### 4.6. References

- (1) Guerra, G.; Vitagliano, V. M.; De Rosa, C.; Petraccone, V.; Corradini, P. *Macromolecules* **1990**, *23*, 1539-1544.
- (2) Woo, E. M.; Sun, Y. S.; Yang, C. P. *Prog. Polym. Sci.* **2001**, *26*, 945-983.
- (3) Gowd, E. B.; Tashiro, K.; Ramesh, C. *Prog. Polym. Sci.* **2009**, *34*, 280-315.
- (4) Milano, G.; Guerra, G. *Prog. Mater. Sci.* **2009**, *54*, 68-88.
- (5) Schellenberg, J., *Syndiotactic Polystyrene: synthesis, characterization, processing and applications*. Wiley: New York, 2010.
- (6) Gowd, E. B.; Nair, S. S.; Ramesh, C. *Macromolecules* **2002**, *35*, 8509-8514.
- (7) Gowd, E. B.; Shibayama, N.; Tashiro, K. *Macromolecules* **2008**, *41*, 2541-2547.
- (8) Gowd, E. B.; Shibayama, N.; Tashiro, K. *Macromolecules* **2007**, *40*, 6291-6295.
- (9) Gowd, E. B.; Tashiro, K. *Macromolecules* **2007**, *40*, 5366-5371.
- (10) Chatani, Y.; Shimane, Y.; Inagaki, T.; Ijitsu, T.; Yukinari, T.; Shikuma, H. *Polymer* **1993**, *34*, 1620-1624.
- (11) Chatani, Y.; Inagaki, T.; Shimane, Y.; Shikuma, H. *Polymer* **1993**, *34*, 4841-4845.
- (12) De Rosa, C. *Macromolecules* **1996**, *29*, 8460-8465.
- (13) Gowd, E. B.; Nair, S. S.; Ramesh, C.; Tashiro, K. *Macromolecules* **2003**, *36*, 7388-7397.
- (14) Yoshioka, A.; Tashiro, K. *Macromolecules* **2003**, *36*, 3593-3600.
- (15) Moyses, S.; Spells, S. J. *Macromolecules* **1999**, *32*, 2684-2689.
- (16) Musto, P.; Mensitieri, G.; Cotugno, S.; Guerra, G.; Venditto, V. *Macromolecules* **2002**, *35*, 2296-2304.
- (17) Capitani, D.; De Rosa, C.; Ferrando, A.; Grassi, A.; Segre, A. L. *Macromolecules* **1992**, *25*, 3874-3880.
- (18) Woo, E. M.; Sun, Y. S.; Lee, M. L. *Polymer* **1999**, *40*, 4425-4429.
- (19) Vittoria, V.; Filho, A. R.; De Candia, F. J. *Macromol. Sci., Part B: Phys.* **1990**, *29*, 411-428.
- (20) Cimmino, S.; Pace, E. D.; Martuscelli, E.; Silvestre, C. *Polymer* **1991**, *32*, 1080-1083.
- (21) De Rosa, C.; Rapacciuolo, M.; Guerra, G.; Petraccone, V.; Corradini, P. *Polymer* **1992**, *33*, 1423-1428.
- (22) Cartier, L.; Okihara, T.; Lotz, B. *Macromolecules* **1998**, *31*, 3303-3310.
- (23) Kobayashi, M.; Nakaoki, T.; Ishihara, N. *Macromolecules* **1989**, *22*, 4377-4382.

- 
- (24) Immirzi, A.; de Candia, F.; Iannelli, P.; Zambelli, A.; Vittoria, V. *Makrom. Chem. Rapid. Commun.* **1988**, *9*, 761-764.
- (25) Tashiro, K.; Yoshioka, A. *Macromolecules* **2001**, *35*, 410-414.
- (26) Chatani, Y.; Shimane, Y.; Inoue, Y.; Inagaki, T.; Ishioka, T.; Ijitsu, T.; Yukinari, T. *Polymer* **1992**, *33*, 488-492.
- (27) De Rosa, C.; Guerra, G.; Petraccone, V.; Pirozzi, B. *Macromolecules* **1997**, *30*, 4147-4152.
- (28) Gowd, E. B.; Shibayama, N.; Tashiro, K. *Macromolecules* **2006**, *39*, 8412-8418.
- (29) Rizzo, P.; Daniel, C.; De Girolamo Del Mauro, A.; Guerra, G. *Chem. Mater.* **2007**, *19*, 3864-3866.
- (30) Tarallo, O.; Schiavone, M. M.; Petraccone, V.; Daniel, C.; Rizzo, P.; Guerra, G. *Macromolecules* **2010**, *43*, 1455-1466.
- (31) Uda, Y.; Kaneko, F.; Kawaguchi, T. *Macromolecules* **2005**, *38*, 3320-3326.
- (32) Kaneko, F.; Kashihara, N.; Tsuchida, T.; Okuyama, K. *Macromol. Rapid Commun.* **2010**, *31*, 554-557.
- (33) Kaneko, F.; Sasaki, K. *Macromol. Rapid Commun.* **2011**, *32*, 988-993.
- (34) Uda, Y.; Kaneko, F.; Kawaguchi, T. *Polymer* **2004**, *45*, 2221-2229.
- (35) Kaneko, F.; Uda, Y.; Kawaguchi, T.; Ute, K.; Yamamuro, O. *Macromol. Symp.* **2006**, *242*, 113-119.
- (36) Gowd, E. B.; Tashiro, K. *Polymer* **2011**, *52*, 822-829.
- (37) Tarallo, O.; Schiavone, M. M.; Petraccone, V. *Polymer* **2011**, *52*, 1426-1435.
- (38) Tarallo, O.; Schiavone, M. M. *Soft Materials* **2011**, *9*, 124-140.
- (39) Tarallo, O.; Petraccone, V.; R. Alburnia, A.; Daniel, C.; Guerra, G. *Macromolecules* **2010**, *43*, 8549-8558.
- (40) Yoshioka, A.; Tashiro, K. *Macromolecules* **2003**, *36*, 3001-3003.
- (41) Rizzo, P.; D'Aniello, C.; De Girolamo Del Mauro, A.; Guerra, G. *Macromolecules* **2007**, *40*, 9470-9474.
- (42) Alburnia, A. R.; Annunziata, L.; Guerra, G. *Macromolecules* **2008**, *41*, 2683-2688.
- (43) ALBUNIA, A. R.; Bianchi, R.; Di, M. L.; Galimberti, M.; Guerra, G.; PANTANI, R.; Senatore, S., Disordered nanoporous crystalline form of syndiotactic polystyrene, process for its preparation and articles comprising the same. Google Patents: 2012.
- (44) Purse, B. W.; Rebek, J. *Proc. Natl. Acad. Sci. U. S. A.* **2006**, *103*, 2530-2534.

- (45) Scarso, A.; Trembleau, L.; Rebek, J. *Angewandte Chemie International Edition* **2003**, *42*, 5499-5502.
- (46) van Hooy-Corstjens, C. S. J.; Magusin, P. C. M. M.; Rastogi, S.; Lemstra, P. J. *Macromolecules* **2002**, *35*, 6630-6637.
- (47) Naidu, S.; Ramesh, N. C. *Macromol. Symp.* **2008**, *273*, 109-114.
- (48) Gowd, E. B.; Tashiro, K.; Ramesh, C. *Macromolecules* **2008**, *41*, 9814-9818.
- (49) Yoshioka, A.; Tashiro, K. *Macromolecules* **2004**, *37*, 467-472.
- (50) Rizzo, P.; Spatola, A.; De Girolamo Del Mauro, A.; Guerra, G. *Macromolecules* **2005**, *38*, 10089-10094.
- (51) Tarallo, O.; Schiavone, M. M.; Petraccone, V. *Eur. Polym. J.* **2010**, *46*, 456-464.
- (52) Jose, R. C.; Shaiju, P.; Nagendra, B.; Gowd, E. B. *Polymer* **2013**, *54*, 6617-6627.
- (53) Torres, F. J.; Civalleri, B.; Pisani, C.; Musto, P.; Alburnia, A. R.; Guerra, G. *J. Phys. Chem. B* **2007**, *111*, 6327-6335.



### Overall Summary

---

#### 5.1. Summary

The overall concept of the thesis is to understand the importance of polymer-solvent interactions on the crystallization behavior and other properties of certain semicrystalline polymers. The presence of an interacting solvent can induce the crystallization of glassy polymers by facilitating the segmental mobility of the polymer chains at ambient temperature. This type of crystallization triggered by solvent molecules is termed as solvent-induced crystallization. Most of the advanced polymer processing techniques such as spin-casting and electrospinning, involve the use of solvent molecules. Here the polymer-solvent interactions play a major role in tuning the structural organization or crystallization of the polymer. It is therefore highly essential to understand the interaction between the polymer and the solvent in detail.

The 1<sup>st</sup> chapter comprises of a general introduction about polymer crystallization and polymorphism. Solvent induced crystallization and cocrystal formation of certain semicrystalline polymers were also described here in detail. The chapter concludes with a short description of the applications of the nanoporous crystalline structures created by the selective removal of the solvent from the crystal lattice of certain polymer cocrystals.

In the 2<sup>nd</sup> chapter, for the first time, we found that the optical clarity of solvent-crystallized PLLA films depends on the polymer-solvent interactions. Water was found to disrupt the formation of spherulites, and thus affect the morphology of solvent-crystallized PLLA films. This was investigated at multiple length scales using various microscopy techniques (polarized optical, electron, and atomic force), thermal analysis and small-, and wide-angle X-ray scattering. PLLA films crystallized in aqueous miscible organic solvents such as tetrahydrofuran (THF) and acetone, and their water mixtures were examined. Polymer-solvent

interactions, solvent evaporation rate and film shrinkage were influenced by the addition of water to the solvent medium and hence resulted in different morphologies. Lamellar thickening was also observed for the solvent treated PLLA films at higher temperatures, above 140 °C. When the temperature is high, the activated amorphous chains diffuse to the crystal growth front and finally adsorbed and crystallized into the thicker crystals.

In the 3<sup>rd</sup> chapter we tried to understand the structural changes in PLLA-solvent complex during solvent desorption. PLLA forms cocrystals ( $\varepsilon$ ) with certain organic solvents such as cyclopentanone (CPO), at subambient temperatures. It was found that the  $\varepsilon$  form transforms to the  $\alpha$  form upon heating just above the glass transition temperature of PLLA. This transformation preserves the chain orientation as seen in the WAXS fiber diagrams. During  $\varepsilon$  to  $\alpha$  transition, the solvent molecules residing within the crystal lattice of the  $\varepsilon$  form migrate into the amorphous phase. DSC thermogram showed a sharp endotherm at this transition temperature. However, infrared spectra did not show the obvious changes in the crystalline sensitive bands indicating that the helical conformation remains unchanged during the  $\varepsilon$  to  $\alpha$  transition. The change in the lamellar parameters, long period, lamellar thickness, amorphous thickness and invariant, during the  $\varepsilon$  to  $\alpha$  transition indicates that the structural reorganization of the stacked lamellar structure is mainly due to the solvent desorption from the crystal lattice to the amorphous phase. On further heating, the solvent molecules residing in the amorphous phase of the  $\alpha$  form facilitates the motion of molecular chains. As a result, some of the amorphous phase crystallizes into the  $\alpha$  form. The higher crystallinity calculated from the WAXS patterns and the change in the lamellar parameters in the temperature range of 100–130 °C confirmed the crystallization of amorphous PLLA. In this way, this study has clarified the intimate connection between the crystal structure and the lamellar structure during the  $\varepsilon$  to  $\alpha$  transition in PLLA/CPO cocrystals.

In the 4<sup>th</sup> chapter, a detailed investigation of the structure controlling factors in syndiotactic polystyrene upon the guest exchange and extraction processes were

carried out. Uniaxially drawn and undrawn films of sPS with three different morphologies, amorphous  $\alpha$ , and  $\gamma$  were used for the preparation of cocrystals. Such obtained cocrystals were used for the guest exchange process. The solvent exchange in these cocrystals was carried out by dipping in n-alkanes, ranging from n-octane to n-decane, for 32 days. It was observed that the guest exchange process of toluene treated amorphous and  $\alpha$  form samples with n-alkanes resulted in the formation of triclinic  $\delta$  form irrespective of the starting morphology. But the toluene treated  $\gamma$  form sample reverted to its original structure after the solvent exchange. On the other hand, when the cocrystals prepared using chloroform was used for the guest exchange process, the results were entirely different. A mixture of  $\delta$  form and  $\varepsilon$  form was obtained after the guest exchange process of chloroform treated amorphous samples. Conversely, the chloroform treated  $\alpha$  and  $\gamma$  forms transformed into triclinic  $\delta$  form and  $\varepsilon$  form, respectively. Guest extraction process was carried out using chloroform treated amorphous and  $\gamma$  form samples. Solvent extraction from chloroform treated amorphous samples, gave a mixture of nanoporous  $\delta$  ( $\delta_e$ ) and  $\varepsilon$  ( $\varepsilon_e$ ) forms. In contrast, pure nanoporous  $\varepsilon$  ( $\varepsilon_e$ ) was obtained after the guest extraction from chloroform treated  $\gamma$  form.

## 5.2. Future Perspectives

- Preliminary studies showed that the PLLA films crystallized in acetone/H<sub>2</sub>O and THF/H<sub>2</sub>O mixture are flexible and mechanically robust, in addition to their transparent nature. Therefore, it will be interesting to study the barrier properties and mechanical properties in detail, especially when we consider the applications of PLLA in packaging.
- Stereocomplex, which is prepared by mixing equal quantities of PLLA and Poly(*D*-lactide) [PDLA], has drawn much attention due to its high melting point (~50 °C higher) compared to the PLLA or PDLA homocrystallites. Efforts can be made to understand how the solvent mixtures affect the stereocomplex formation and its structure and morphology.

- Detailed investigation could be carried out of the possibility of cocrystal formation by PLLA/PDLA stereocomplex and associated structural changes upon changing the reaction parameters.
- The present work identified the conditions to tune the porosity of sPS. This comprehension can be further utilized to conduct polymerization and chemical reactions within a confined space by introducing the reactants into the cavities.

---

---

## Papers Presented at Conferences

### *Oral Presentations*

1. Molecular, Crystalline, and Lamellar Length-Scale Changes in the Poly(*L*-lactide) (PLLA) during Cyclopentanone (CPO) Desorption in PLLA/CPO Cocrystals. **P. Shaiju** and E. Bhoje Gowd, MRSI Annual Technical Meeting – 2016, held at IIST, Thiruvananthapuram, Kerala (*Best Oral Presentation Award*).
2. Temperature Induced Structural Changes in the Cocrystal formed by Poly(*L*-lactic acid) and Cyclopentanone, **P. Shaiju**, N.S. Murthy and E. Bhoje Gowd, National Seminar on Green Analytical Techniques (NASGAT-2015), held at Department of Chemistry, D.B. College, Sasthamcotta, Kollam, (Kerala) (*Best Oral Presentation Award*).
3. Lamellar Thickening in Transparent and Crystalline Poly(*L*-lactide) Prepared by Solvent Induced Crystallization. **P. Shaiju** and E. Bhoje Gowd, Short Course on Polymer Science & Indo-Japan Joint Symposium on Polymeric Materials, 31<sup>st</sup> January-1<sup>st</sup> February, 2017, held at Thiruvananthapuram, Kerala.
4. Molecular, Crystalline and Lamellar Length-scale Changes in the Poly(*L*-lactide) (PLLA) during Cyclopentanone (CPO) Desorption in PLLA/CPO Cocrystals. **P. Shaiju** and E. Bhoje Gowd, International Conference on Advanced Materials & Technology (ICMAT)-2016, held at SJCE, Mysuru, Karnataka.
5. Influence of La<sub>0.5</sub>Sr<sub>0.5</sub>CoO<sub>3-δ</sub> (LSCO) Particles on the Crystallization Behavior of Poly (Vinylidene Fluoride). **P. Shaiju**, K. S. Deepa, M. T. Sebastian, J. James and E. Bhoje Gowd, National Seminar on Frontiers of Polymers and Advanced Materials (FPAM-2014), held at university of Kerala, Thiruvananthapuram, Kerala.

### *Poster Presentations*

1. Solvent-Induced Crystallization and Phase Transitions of Poly(*L*-lactide) (PLLA). **P. Shaiju** and E. Bhoje Gowd, International Conference on Polymer Science and Technology (MACRO-2017), held at Thiruvananthapuram, Kerala.
2. Molecular, Crystalline and Lamellar Length-scale Changes in the Poly(*L*-lactide) (PLLA) during Cyclopentanone (CPO) Desorption in PLLA/CPO Cocrystals. **P. Shaiju** and E. Bhoje Gowd, Polymer Conference for Young Researchers (PCYR-2015), held at CSIR-NIIST, Thiruvananthapuram, Kerala.

3. Thermally Induced Structural Changes in the Cocrystal formed by Poly(*L*-lactic acid) and Cyclopentanone. **P. Shaiju**, N. Sanjeeva Murthy and E. Bhoje Gowd, International Symposium on Polymer Science and Technology (MACRO-2015), held at Kolkata, West Bengal.
4. Structural Phase Transitions of Syndiotactic Polystyrene upon the Guest Exchange Process. **P. Shaiju** and E. Bhoje Gowd, Polymer Conference for Young Researchers (PCYR-2014), held at CSIR-NIIST, Thiruvananthapuram, Kerala.
5. Crystallization, Polymorphism and Thermal Behavior of Plasticized Poly (*L*-lactic acid). **P. Shaiju**, S. Nagarajan and E. Bhoje Gowd, International Conference on Advanced Functional Materials (ICAFM-2014), held at Thiruvananthapuram, Kerala.
6. Effect of Two-Dimensional Nanoparticles on Crystallization, Polymorphism & Thermal Properties of Syndiotactic Polystyrene. **P. Shaiju**, B. Nagendra and E. Bhoje Gowd, National conference on Nano Science and Technology (NANO INDIA-2013), held at Thiruvananthapuram, Kerala.
7. Crystallization, Polymorphism & Thermal Properties of Syndiotactic Polystyrene-Graphene/Carbon Nanotube Nanocomposites: A Comparative Study. **P. Shaiju** and E. Bhoje Gowd, Third Federation of Asian Polymer Societies (FAPS) Polymer Congress and MACRO-2013, hosted by the Indian Institute of Science (IISc), Bangalore, Karnataka.
8. Influence of Host Preparation Method on the Structural Phase Transitions of Syndiotactic Polystyrene upon the Guest Exchange with n-Alkanes. **P. Shaiju**, Robbinson C. Jose, Baku Nagendra and E. Bhoje Gowd, Third Federation of Asian Polymer Societies (FAPS) Polymer Congress and MACRO-2013, hosted by the Indian Institute of Science (IISc), Bangalore, Karnataka.

---

---

## List of Publications

### Related to Thesis

1. Molecular, Crystalline, and Lamellar Length-Scale Changes in the Poly(*L*-lactide) (PLLA) during Cyclopentanone (CPO) Desorption in PLLA/CPO Cocrystals; **P. Shaiju**, N. S. Murthy, E. Bhoje Gowd\*.  
*Macromolecules* **2016**, 49, 224-233.
2. Polystyrene: Syndiotactic; **P. Shaiju**, E. Bhoje Gowd\*, H. H. Görtz. P. Shaiju, E. Bhoje Gowd\* and H-H Görtz.  
*Reference Module in Materials Science and Materials Engineering; Elsevier*, 02612, **2016**.
3. Structural Phase Transitions of Syndiotactic Polystyrene upon the Guest Extraction Process; **P. Shaiju** and E. Bhoje Gowd\*.  
*Macromolecular Symposia* **2016**, 359, 104-110.
4. Factors Controlling the Structure of Syndiotactic Polystyrene upon the Guest Exchange and Guest Extraction Processes; **P. Shaiju** and E. Bhoje Gowd\*.  
*Polymer* **2015**, 56, 581-589.
5. Influence of Host Preparation Method on the Structural Phase Transitions of Syndiotactic Polystyrene upon the Guest Exchange with n-Alkanes; R.C. Jose, **P. Shaiju**, B. Nagendra and E. Bhoje Gowd\*.  
*Polymer* **2013**, 54, 6617-6617.
6. Water Disrupts Solvent-Induced Crystallization in Poly(*L*-lactide) to Yield Transparent Films; **P. Shaiju**, N. S. Murthy, E. Bhoje Gowd\*.  
(Submitted to *ACS Sustainable Chem. Eng.*)
7. Structural Changes and Lamellar tilting in Uniaxially Drawn Poly(*L*-lactide) Treated with Different Solvents and Solvent Mixtures; **P. Shaiju** and E. Bhoje Gowd\*.  
(Manuscript under preparation)

### Not Related to thesis

8. Poly(vinylidene fluoride)/La<sub>0.5</sub>Sr<sub>0.5</sub>CoO<sub>3-δ</sub> composites: Influence of LSCO particle size on the structure and dielectric properties; K. S. Deepa, **P. Shaiju**, M. T. Sebastian, E. Bhoje Gowd\* and J. James\*.  
*Phys. Chem. Chem. Phys.* **2014**, 16, 17008-17017.
9. Effect of Poly(ethylene Glycol) Dimethyl Ethers (PEGDME) on the crystallization behaviour of Poly(*L*-lactide); **P. Shaiju**, N. M. Praveena and E. Bhoje Gowd\*.  
(Manuscript under preparation)